SURFACE MODIFICATION OF NANOSTRUCTURED MATERIALS FOR LITHIUM-ION BATTERIES

BY

WEI ZHANG

A THESIS

SUBMITTED TO THE FACULTY OF

ALFRED UNIVERSITY

IN PARTIAL FULFILLMENT OF THE REQUIREMENTS
FOR THE DEGREE OF

DOCTOR OF PHILOSOPHY

IN

MATERIALS SCIENCE AND ENGINEERING

ALFRED, NEW YORK

AUGUST, 2016

SURFACE MODIFICATION OF NANOSTRUCTURED MATERIALS

FOR LITHIUM-ION BATTERIES

BY

WEI ZHANG
B.S. HUAZHONG UNIVERSITY OF SCIENCE &TECHNOLOGY (2008)
M.S. HUAZHONG UNIVERSITY OF SCIENCE &TECHNOLOGY (2012)

SIGNATUER OF AUTHOR_____

APPROVED BY_____

DOREEN D. EDWARDS, ADVISOR

_____

DAWEI LIU, ADVISORY COMMITTEE

_____

SCOTT T. MISTURE, ADVISORY COMMITTEE

_____

DAVID W. LIPKE, ADVISORY COMMITTEE

ACCEPTED BY_____

ALASTAIR N. CORMACK, DEAN
KAZUO INAMORI SCHOOL OF ENGINEERING

ACCEPTED BY_____

NANCY J. EVANGELISTA, ASSOCIATE PROVOST
FOR GRADUATE AND PROFESSIONAL PROGRAMS
ALFRED UNIVERSITY

ACKNOWLEGEMENTS

At the moment my Ph.D. study comes into final step, I am looking back on my four years life at Alfred and feel so lucky to have many great teachers and friends around. I would like to take the opportunity to say thank you to all of them. Without their help and support, it is impossible for me to finish my thesis.

First I wish to bring my heartiest gratitude to my advisor, Dr. Doreen Edwards, for providing me with this greatest opportunity to work in her group and giving me strongest support on my Ph.D. project during the past year. Doreen is a gracious and enthusiastic mentor. She has been always supporting my research work with her insightfulness, patience, and encouraging me to pursue my dreams. I also wish to bring my deepest gratitude to my previous advisor Dr. Dawei Liu during the beginning of more than years of my Ph.D. study. He generously admitted me into Alfred and guided me into research with enormous patience and enthusiastic help. Even after he left Alfred, I still got lots of valuable suggestions and feedback from him, which helped me to finish my research in this thesis.

Second, I would like to thank my thesis committee members, Doctors David Lipke, and Scott Misture, whose suggestions and support are deeply appreciated. I first met Dr. Misture in a graduate class, he probably did not know at the time that I believe he is one of the most influential educators I have been honored to learn from. I met Dr. Lipke when I was a first-year Ph.D. student. Dr. Lipke urged me to understand the underlying mechanisms behind the electrochemical behavior of materials. And the insights he provide in my committee meetings inspired creative thinking and have been invaluable for moving the research forward. In addition, many thanks to Dr. Yiyuan Wu, Gerry Wynick, Yiyu Li, Yin Liu, Brittany Higgins, and Bo Zhang for their help in my research.

Finally, I am really grateful to my family for the essential role they have played in accomplishing this Ph.D. study; they are persistently supportive to me and proud of me. My dear wife who always encourage and support me no matter what situation I have faced. The past four years have not been an easy ride, and I truly thank my wife for her accompany, even when I was moody and depressed, thank you for always loving and believing in me. My thesis would never have been accomplished without you.

TABLE OF CONTENTS

LIST OF TABLES

Page

LIST OF FIGURES

Page

CHAPTER 1

CHAPTER 2

CHAPTER 3

CHAPTER 4

Chapter 5

ABSTRACT

Lithium-ion batteries (LIBs) continue to attract a tremendous amount of interest because they are the most promising candidate to power hybrid electric vehicles (HEV), electric vehicles (EV) and stationary energy storage systems. However, to meet the needs of the soaring markets, new generations of LIBs are required with increased energy and power density, longer cycle life, improved safety, and lower cost. To achieve this goal, electrode materials discovery and development is necessary. In particular, anode materials remain a key factor in improving the performance of LIBs due to their notably higher capacities than cathode materials. However, for a large fraction of anode materials, major critical challenges are the poor cyclic stability and safety issue during the repeated charging and discharging operations. Therefore, it is still greatly important to develop new materials for overcoming these problems.

In this thesis, a two-step strategy comprising synthesis and surface modification was adopted to develop various novel anodes materials for LIBs. First, we synthesized morphology-controlled TiO_2, $Li_4Ti_5O_{12}$, and MoS_2 nanomaterials, and then used surface modification methods including doping, calcination, composites and coating to improve the electrochemical performance of prepared materials.

It was found that the undoped TiO_2 showed an initial capacity of 201 mAh g^{-1} but only had 44.1% of the initial capacity retained after 50 cycles at mixed current densities of 30, 150, and 500 mA g^{-1} at 55 °C, while the Mn-doped one exhibited an initial capacity of 190 mAh g^{-1} and 91.4% capacity retention with superior reversible capacity under the same test conditions. A similar result was also observed in the nitrogen-treated porous TiO_2, which exhibited a higher capacity of 293 mAh g^{-1} than that of air-treated sample

(187 mAh g^{-1}) after 50 cycles. In addition, the nitrogen-treated $Li_4Ti_5O_{12}$-TiO_2 sample showed significantly improved capacity, good rate capability, and cycling stability compared with pure $Li_4Ti_5O_{12}$. It delivered capacities of 220 mAh g^{-1}, 213 mAh g^{-1} at a current density of 30 mA g^{-1} when tested at room temperature and 55 °C, respectively; it still had a capacity of 184 mAh g^{-1}, 197 mAh g^{-1} after 50 cycles, which was noticeably higher than the known theoretical capacity of pure $Li_4Ti_5O_{12}$ (175 mAh g^{-1}). Furthermore, compared with the previous results, the hierarchical nanocomposites of MoS_2@$Li_4Ti_5O_{12}$ showed much improved capacity (433 mAh g^{-1} after 70 cycles at various current densities), good rate capability (320 mAh g^{-1} and 210 mAh g^{-1} at 500 mA g^{-1} and 2000 mA g^{-1}, respectively), outstanding cycling stability (174 mAh g^{-1} after 1000 cycles at 5000 mA g^{-1}) and wide operating temperature range extending from -15 to 55 ºC when used as anode materials for lithium ion batteries. Finally, the mechanism of surface modification on the improvement of nanomaterials' performance has been studied, and simple methods to fabricate promising candidates for the next generation anode materials are given.

INTRODUCTION

A. Background on Lithium-Ion Batteries

The continuous increase in demand for oil and the associated environmental issues are continuing to exert pressure on the already strained world energy infrastructure. Therefore, there has been an ever increasing and urgent demand for a prolonged cycle life, earth-abundant elements, and environmentally friendly high-power energy systems.[1-3] Significant progress has been made in the development of renewable energy technologies such as solar cells, fuel cells, and bio-fuels.[4-6] Among them, rechargeable lithium-ion batteries (LIBs) have been widely studied due to its relatively high specific energy and specific power, and it has revolutionized portable electronic devices.[7] At present, LIBs are efficient, light-weight, and rechargeable power sources for consumer electronics such as laptops, digital cameras, and cell phones.[8] Moreover, they have been intensively studied for use as power supplies of electric vehicles and hybrid electric vehicles, which require high energy and power densities. The worldwide market for rechargeable lithium-ion batteries is now valued at 10 billion dollars per annum and growing.[9]

Generally, the rechargeable lithium battery is a simple lithium-ion electrochemical device that consists of an anode and a cathode separated by a non-aqueous liquid electrolyte. Anodes and cathodes are made of different materials; anode wants to oxidize by giving up electrons and cathode wants to reduce through accepting electrons. When the anode and cathode separated by an electrolyte are

connected with a wire, chemical reactions occur on the surfaces and in inside both electrodes, meanwhile, the chemical potential converts to electrical energy. The principal concept of lithium-ion batteries is illustrated in Figure 1-1. As shown in this figure, anode and cathode are separated by the electrolyte, which is an electronic insulator but an ion conductor. Upon charging, lithium ions are released by the cathode and intercalated at the anode. When the cell is discharged, lithium ions are

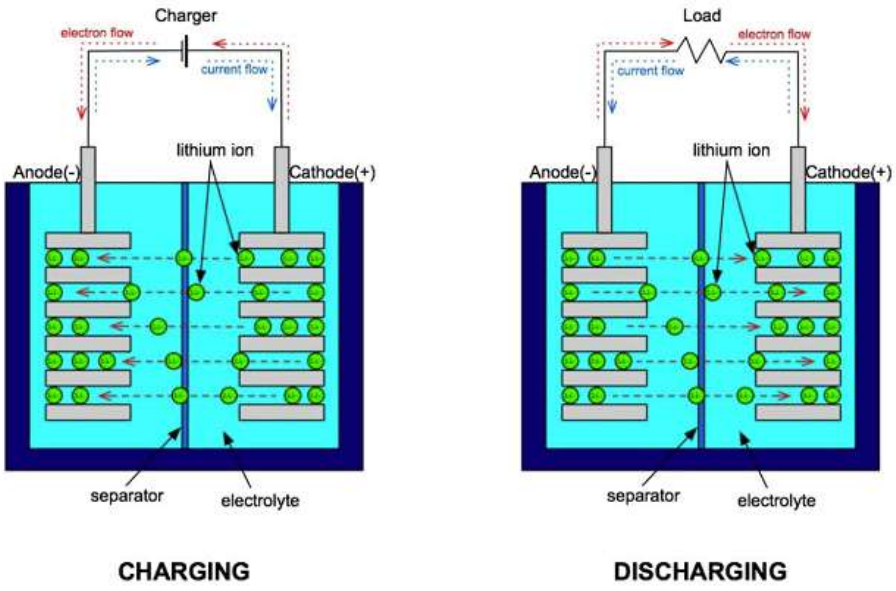

Figure 1-1. Schematic representation of a lithium-ion battery (from ref. 10)

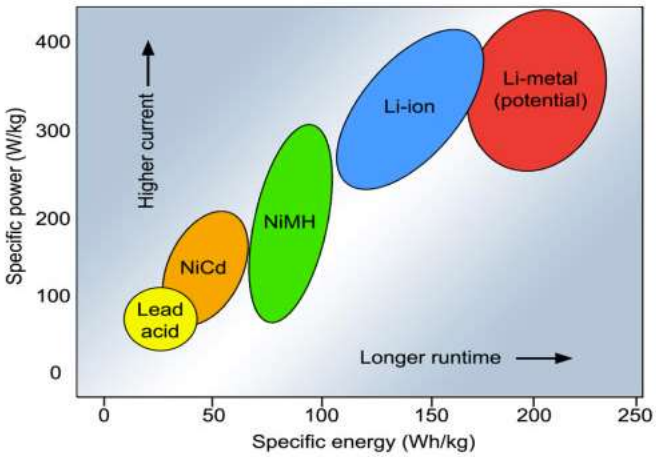

Figure 1-2. Specific energy and power densities of different rechargeable batteries. Reproduced with the permission from ref. 7 (Copyright 2001 Nature Publishing Group).

extracted by the anode and inserted into the cathode. During these processes, the electrons pass through the external circuit. A more detailed description of LIBs can be found in the literature.[8-11] Compared with the traditional nickel-cadmium and nickel-metal-hydride rechargeable batteries, LIBs have both higher energy and power densities (Figure 1-2). The limiting factor in LIBs is the performance of the electrodes, which is, in turn, determined by the chemistry, crystal structure, microstructure, and physical properties of the materials used as the electrodes. Electrode materials must fulfill three fundamental requirements to reach the goal of a high specific energy and power density: (1) a high specific charge and charge density, that is, a high number of available charge carriers per mass and volume unit of the material; (2) a high cell voltage, resulting from a high (cathode) and low (anode) standard redox potential of the respective electrode redox reaction; and (3) a high reversibility of electrochemical reactions at both cathodes and anodes to maintain the specific charge for hundreds of charge/discharge cycles.[4]

First-generation of LIBs used metallic lithium as the anode, which combined a very negative redox potential with a low weight. It was later replaced by carbon-based material because of safety concerns, and the graphite becomes a major choice for commercial anodes in LIBs. The first commercial LIBs appeared in 1991, which utilized graphite as the anode material, and lithium cobalt oxide ($LiCoO_2$) as the cathode material. The electrochemical reactions involved in this typical LIB can be expressed as follow:

(Anode) $6C + xLi^+ + xe^- \leftrightarrow Li_xC_6$ (1-1)

(Cathode) $LiCoO_2 \leftrightarrow Li_{1-x}CoO_2 + xLi^+ + xe^-$ (1-2)

More recently, replacement of graphite by lithium intercalation compounds has attracted attention due to their observed improvement on the cells' cycle life, capacity and safety. Compared with anode materials, there are two types of cathode materials. One comprises layered compounds with an anion close-packed lattice; transition metal cations occupy alternate layers between the anion sheets, and lithium ions are intercalated into remaining empty layers. $LiTiS_2$, $LiCoO_2$, and $LiNi_{1-x}Co_xO_2$ all belong to this group. Among them, $LiCoO_2$ has been the dominant cathode material for lithium-ion batteries owing to its ease of preparation and stable electrochemical cycling performance, provided the lithium utilization is no more than 50%.[12] Concerns about the high cost of cobalt and the safety issues of the batteries have led to the development of alternative cathode materials that offer lower cost, longer life, and improved abuse tolerance. The developments have focused on lithium transition-metal phosphates ($LiMPO_4$, M=Mn, Ni, Co).[13-16] Another group of cathode materials has more open structures, such as vanadium oxides[17] and the tunnel compounds of manganese oxides.[18] These materials generally provide the advantages of better safety and lower cost compared to the first group. The disadvantage is that they have the lower energy density (energy per unit of volume) owing to their more open lattices.

Figure 1-3 listed various anode and cathode materials presently used or are promising for the next generation of LIBs together with their working voltages and

specific capacities.[19] Compared with cathode materials, anode materials have higher specific capacities: for example, Si anode has a theoretical capacity over 4000 mAh g^{-1}, which is more than 20 times larger than that of cathode materials. Meanwhile, anode materials also suffer from the side reactions to form solid electrolyte interface (SEI) especially operate under a low voltage (< 1 V).[20] Therefore, it is urgent to develop new anode materials with high capacity, good safety, and rate capability in order to meet the future demands of commercial vehicles. In this project, we will focus on the study of anode materials, and the detailed discussions are shown in section B.

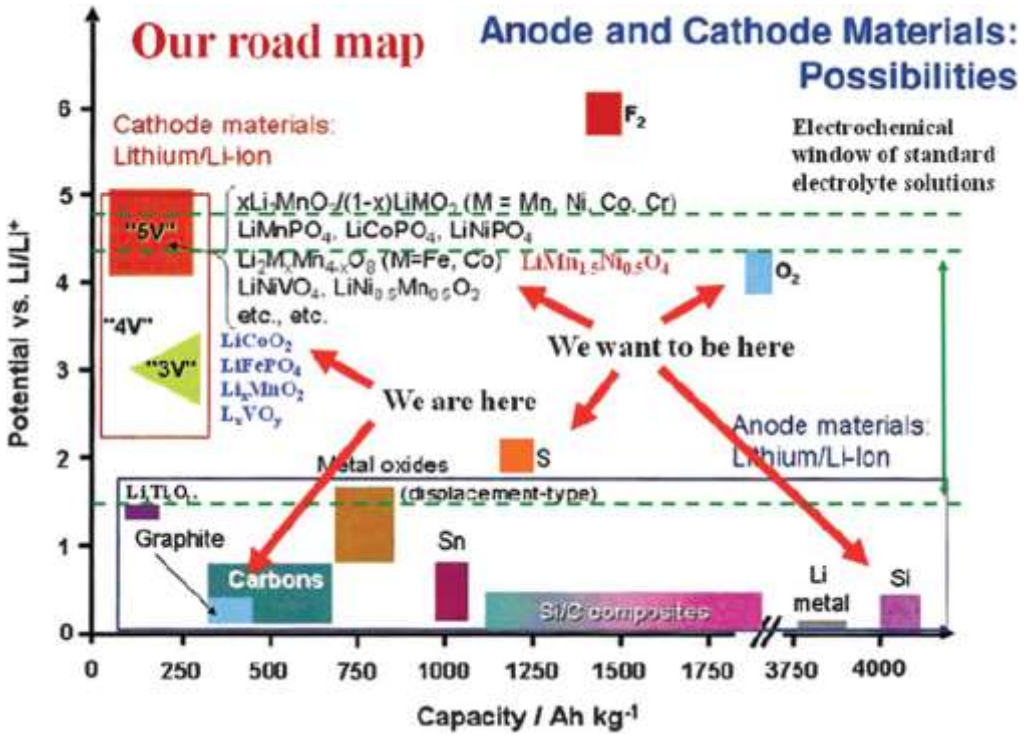

Figure 1-3. The road map for R&D of new electrode materials, compared to today's state-of-the-art. The y and x-axes are voltage and specific capacity, respectively. Reproduced with the permission from ref. 19 (Copyright 2011 Royal Society of Chemistry).

B. Advanced Anode Materials and Challenges in Current Studies

Generally, there are four most promising groups of materials that can be used in the anode electrodes as follows:

1. Carbonaceous materials

Carbonaceous materials, especially graphite, are the most used anode materials and will remain important and relevant for the foreseeable future. They can avoid the problem of Li dendrite formation by reversible intercalation of Li ion into graphite host lattice during cycling, which provides good cyclic stability for LIB anodes. In addition, graphite also has high intrinsic electrical conductivity (1×10^6 S cm^{-1}), low lithiation potential (0.25-0.05 V *vs*. Li^+/Li) and relatively high specific capacity (~372 mAh g^{-1}).[21] When lithium ions' are inserted into graphite at a potential of lower than 1 V *vs.* Li^+/Li, the electrolyte will be reduced, accompanied by the formation of a passivating solid electrolyte interface (SEI) film on the graphite surface. This film has a porous structure that allows lithium ions to move from the electrolyte solution into the graphite and prohibits solvent molecules from intercalating into the graphite host since the size of solvent molecules is much greater than that of lithium ions. As a result, it will avoid the rest of graphite further reacts with electrolyte and maintain the stability of anodes during cycling.[21-23] However, the formation of SEI film is accompanied by some initial irreversible capacity loss and the existence of gas products, which is highly undesirable from the process and safety points of view. Meanwhile, this passivation reaction depends on the surface area of materials,

indicating that higher surface area will consume excessive electrolyte solution and charges to form more SEI film leading to a greater irreversible capacity loss. More important is the fact that most of the lithium intercalated into graphite at potentials less than 100 mV versus Li^+/Li aggravates the batteries' initial capacity loss. Eventually, this formed SEI film will become thinner when exposed to an elevated temperature due to the excessive electrode and electrolyte reactions, thus leading to serious safety concerns.[9] For example, Chen and co-workers showed that the exothermal reaction observed in lithiated carbon in the temperature range between 110 °C and 180 °C in the presence of electrolyte was caused by the continuous formation of a SEI film until all reactants are depleted.[24] To overcome this problem, many work has been done to improve the thermal stability of lithiated graphite through different approaches.[20,25,26]

2. Sn and Si-based alloys and composites

Lithium can be electrochemically alloyed/dealloyed with some semi-metallic elements in groups IV-VI, such as Sn, Si, Ge, P and S, and also many metallic elements, such as Al, Mg, Zn, Fe and Ag.[27-29] These alloyed anodes are well-known for their promise of high specific capacities (900 mAh g^{-1} and above) (Figure 1-4), compared with the conventional graphite anode. As an example, the alloying reaction between Li and Si can lead to a final product of stoichiometry $Li_{4.4}Si$, delivering a capacity of 4200 mAh g^{-1} (*vs.* 372 mAh g^{-1} for graphite). However, the consequence of accommodating such a large amount of lithium is large volume expansion–contraction (>300%) upon cycling, for instance, a Si anode electrode with the

thickness of 40 μm can expand to over 150 μm in the charge process.[20] These changes lead to rapid deterioration of the electrode (cracks, and eventually, pulverization), thus limiting its lifetime to only a few charge/discharge cycles. The main approaches to overcome this problem are through the use of both nanoparticles and composite structures, which can better accommodate these huge volume changes.[30]

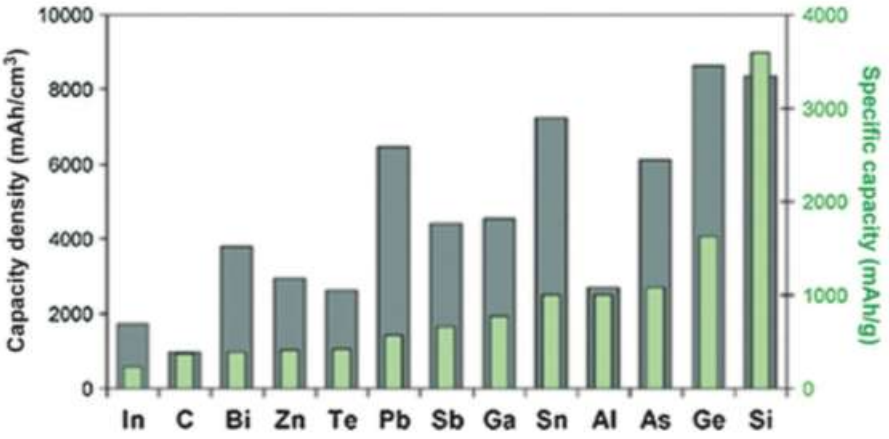

Figure 1-4. Specific capacities and capacity densities for selected alloy anodes. Reproduced with the permission from ref. 20 (Copyright 2012 John Wiley and Sons).

For example, Zhang's group[30] reported the preparation of Si nanocomposites by embedding Si nanoparticles in polypolyacrylonitrile (PAN) fibers using the electrospinning method. Then, the prepared Si/PAN fibers were calcined at high temperature to get the final Si-filled carbon (Si/C) nanocomposites (Figure 1-5a and b). This as-prepared Si/C nanocomposite combined the advantages of both carbon (long cycle life) and Si (high Li-storage capacity) and exhibited high reversible capacity (around 800 mAh g^{-1} at 100 mA g^{-1}) and relatively good capacity retention (84.5% after 20 cycles) when tested as anodes in LIBs (Figure 1-5c and d). The good electrochemical performance of these nanocomposites can be ascribed to the existence of carbon fibers cores that acted as efficient electron transport pathways and

stable mechanical support for keeping the structural integrity of the electrodes during cycling. However, achieving longer cycle life of these alloyed anodes remains a challenge.

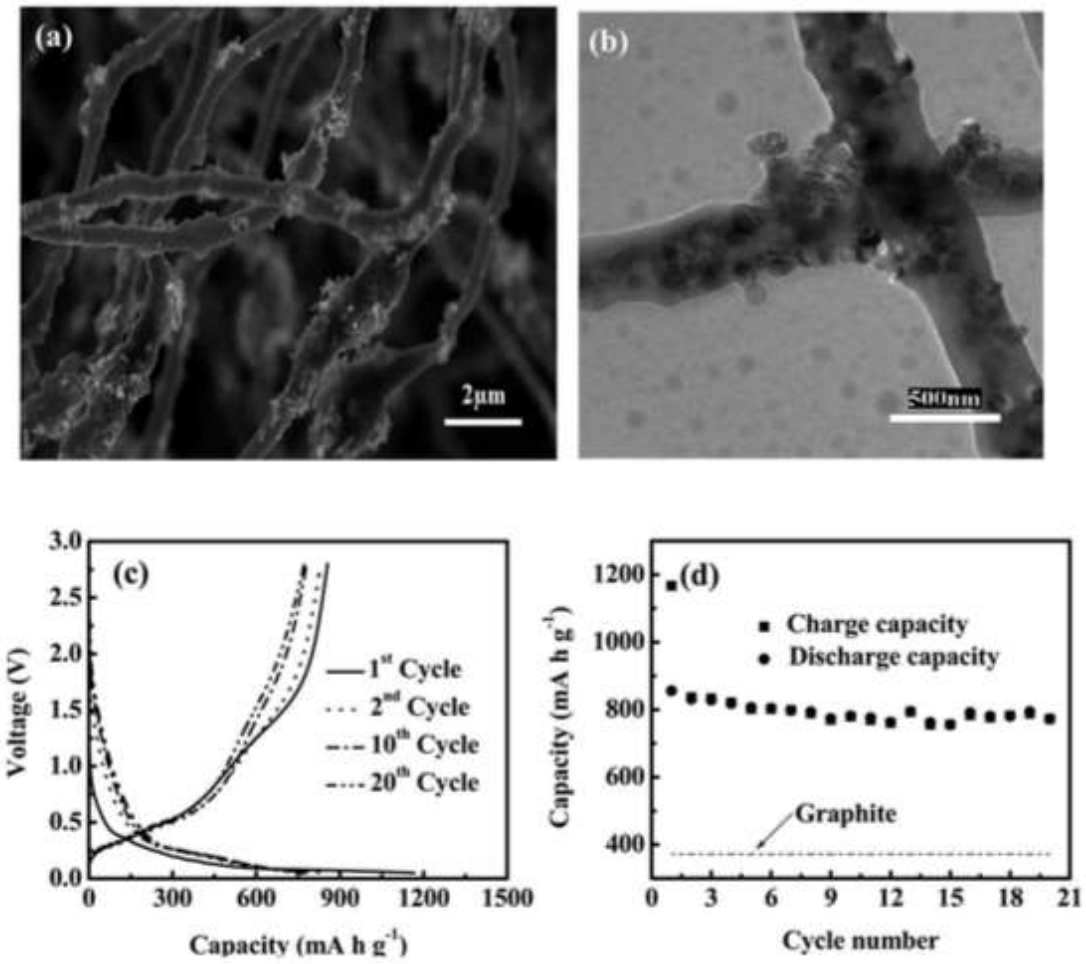

Figure 1-5. a) SEM and b) TEM images of Si/carbon nanocomposites, and c) Galvanostatic charge-discharge curves and d) cycling performance of Si/carbon nanofibers. Current density: 100 mA g^{-1}. Reproduced with the permission from ref. 30 (Copyright 2009 Royal Society of Chemistry).

3. Metal oxides

Metal oxides are considered to be promising candidates for anode materials due to relative ease of large-scale fabrication, specific crystal structures, and their rich redox reactions involving different ions which contributes to high specific

capacities/capacitances.[31] All metal oxide-based anodes can be divided into three groups depending on their reaction mechanism: 1) Li-alloy reaction mechanism, 2) insertion/extraction reaction mechanism that involves the insertion and extraction of Li^+ into and from the lattice of the metal oxide, and 3) conversion reaction mechanism that involves the formation and decomposition of Li_2O, accompanying the reduction and oxidation of metal nanoparticles.[25,32-34] These three reaction mechanism can be expressed as follows:[25]

Li-alloy reaction mechanism:

$$M_xO_y + 2yLi^+ + 2ye^- \rightarrow xM + yLi_2O \quad (1\text{-}3)$$

$$M + zLi^+ + ze^- \leftrightarrow Li_zM \quad (1\text{-}4)$$

Insertion reaction mechanism:

$$MO_x + yLi^+ + ye^- \leftrightarrow Li_yMO_x \quad (1\text{-}5)$$

Conversion reaction mechanism:

$$M_xO_y + 2yLi^+ + 2ye^- \leftrightarrow xM + yLi_2O \quad (1\text{-}6)$$

Among them, transitional metal oxides (e.g. TiO_2), which store Li^+ *via* the insertion reaction mechanism, attract many people's attention due to their low cost and non-toxicity. Furthermore, TiO_2 also has a relatively higher lithium insertion/extraction voltage (<1.7 V vs. Li^+/Li), which can avoid metallic lithium dendrite formation and improve the safety of batteries by reducing the excessive formation of SEI film and lithium plating on anodes.[35] Among the several polymorphs of TiO_2, anatase TiO_2 is considered to be the most promising anode materials for lithium-ion batteries because of its high reversible capacity.[36] Typically the Li^+

insertion/extraction reaction for TiO_2 occurs in the potential range of 1.4-1.8 V vs. Li^+/Li, according to the following reaction:

$$xLi^+ + TiO_2 + xe^- = Li_xTiO_2 \quad (1\text{-}7)$$

The maximum theoretical capacity is 335 mAh g^{-1} which corresponds to x=1 and to the complete reduction of Ti^{4+} to Ti^{3+}. However, the number of electrons involved in this insertion reaction is generally less than one because Li can only be accommodated into the sites in TiO_2. Therefore, TiO_2 has relatively low specific capacity in practice (below 200 mAh g^{-1}).[37] To overcome this problem, various nanostructured TiO_2 has been reported with much improved electrochemical performance. For instance, Jiang et al. studied three different commercially available anatase nanopowders with crystallite sizes of 6, 15 and 30 nm, respectively (Figure 1-6).[38] They reported a first discharge capacity of more than 350 mAh g^{-1} and 209 mAh g^{-1} for the first charge with the 6 nm material. Moreover, they obtained very good capacities at ultra fast regime (~137 mAh g^{-1} at 40 A g^{-1}). The good performance is attributed to the small crystallite size and the porous structures, which favor the complete wetting of the TiO_2 by the liquid electrolyte so that rapid Li^+ insertion/extraction can be achieved. However, like other nanomaterials, more significant side reactions with electrolyte will reduce their cycle life and stability in the practical applications.

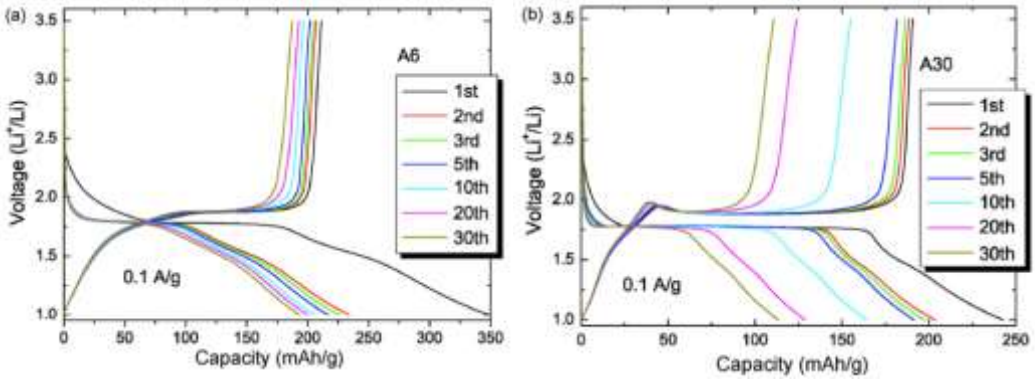

Figure 1-6. Discharge/charge profiles of the nanocrystalline anatase electrodes with different particle sizes tested at 100 mA g^{-1} for 30 cycles. Reproduced with the permission from ref. 38 (Copyright 2007 Elsevier).

4. $Li_4Ti_5O_{12}$ Electrodes

In the search for safe materials with better cyclic stability at various operation environments to replace conventional carbon-based anodes, lots of efforts have been made to investigate spinel lithium titanate ($Li_4Ti_5O_{12}$) because of its several inherent advantages. First, lithium titanate-based materials exhibit long flat operation potential plateau and high lithiation redox voltage (~1.55 V vs. Li^+/Li), which could avoid the safety issues of forming too many SEI films, because undesirable electrolyte decomposition mostly occurs at the reduction potential lower than 1 V (vs. Li^+/Li).[39,40] Second, the spinel $Li_4Ti_5O_{12}$ is a zero-strain insertion material and can accommodate three Li^+ per molecule with no volume change, resulting in excellent cyclic stability (Figure 1-7). The insertion reaction can be expressed as follows:

$$Li_4Ti_5O_{12} + xLi^+ + xe^- \leftrightarrow Li_{4+x}Ti_5O_{12} \quad (0<x<3) \qquad (1\text{-}8)$$

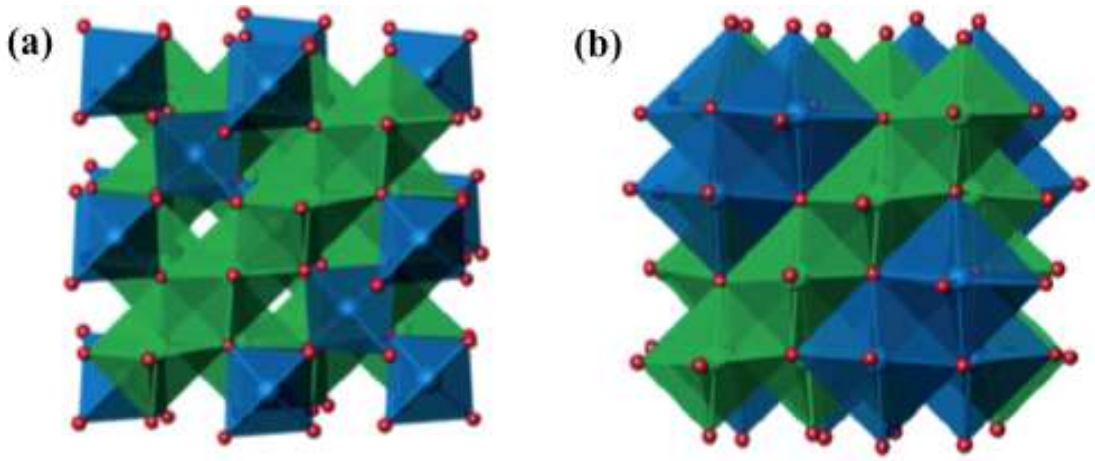

Figure 1-7. a) $Li_4Ti_5O_{12}$ spinel structure type and b) $Li_7Ti_5O_{12}$ rock salt structure type: blue tetrahedra represent lithium, and green octahedra represent disordered lithium and titanium. Reprinted with permission for ref. 41 (Copyright 2006 American Chemical Society).

Third, $Li_4Ti_5O_{12}$ is a cost-effective anodic material due to the abundance of element Ti. However, $Li_4Ti_5O_{12}$ has limited intrinsic capacity (175 mAh g^{-1}) and low electronic conductivity ($<10^{-13}$ S cm^{-1}) which makes this material almost irrelevant for the high energy density and fast charge/discharge batteries required for practical applications.[42] Using the strategy of nanomaterials could remarkably improve their electrochemical performance.[43,44] For example, Chen et al. synthesized vertically aligned $Li_4Ti_5O_{12}$ nanosheet arrays grown directly on Ti foil by a hydrothermal process in LiOH solution and subsequent topotactical transformation *via* thermal decomposition. This self-supported LTO nanosheet arrays standing on Ti foil exhibited an excellent rate capability (a reversible capacity of 163 mA h g^{-1} and 78 mA h g^{-1} at 20 C and 200 C, respectively) and an outstanding cycling performance (a capacity retention of 124 mA h g^{-1} after 3000 cycles at 50C) (Figure 1-8).[44] However,

due to the low intrinsic capacity of $Li_4Ti_5O_{12}$, new approaches still need that could further enhance its capacities.

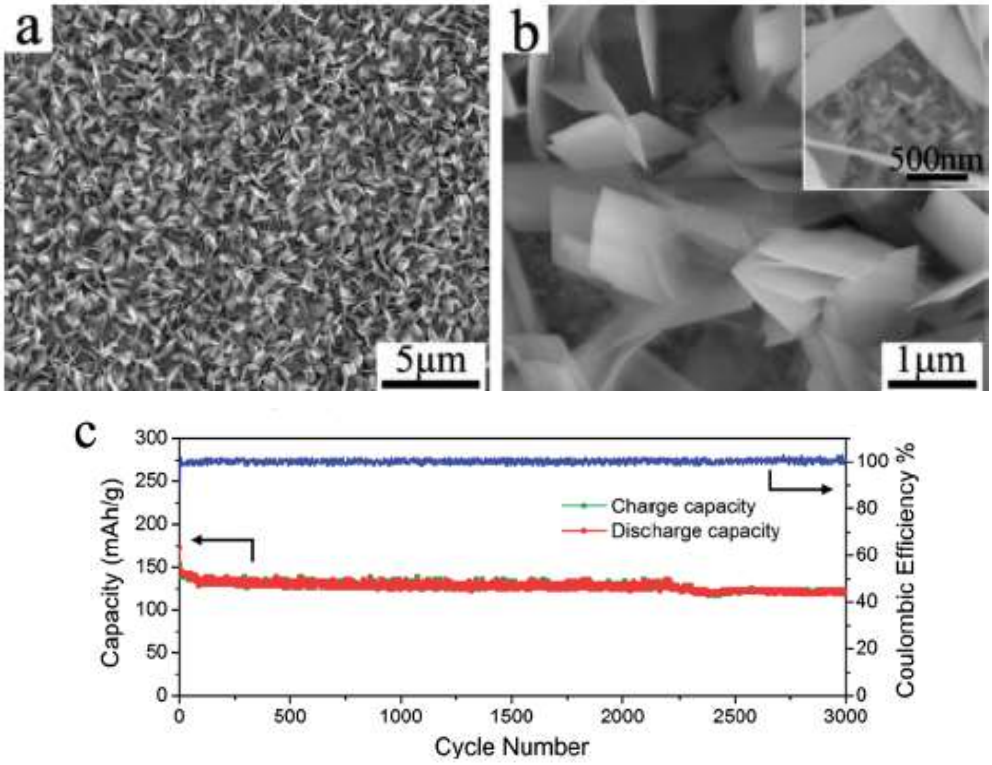

Figure 1-8. a) and b) SEM images of LTO nanosheet arrays standing on Ti foil obtained at [LiOH]=0.05 M, c) Specific capacity and Coulombic efficiency for 3000 cycles at 50 C for LTO. Reproduced with the permission from ref. 44 (Copyright 2013 Royal Society of Chemistry).

C. The Solutions with Surface-Modified Nanomaterials

Nanostructuring is a common way to improve the electrochemical performance of materials used in LIBs. The advantages of using nanomaterials include: easier to occur electrode reactions compared to bulk materials, short distances for lithium-ion transport within the electrodes, high lithium-ion flux across the interface, and better accommodation of strain associated with intercalation.[9] Therefore, numerous studies have been focused on the study of nanomaterials used in electrodes, and remarkable

improvement on the performance of lithium-ion batteries have been reported. Comprehensive reviews to cover a large variety of nanostructured electrode materials can be found in the literatures.[4,9,13,19,20] However, nanomaterials are certainly not a panacea. Nanomaterial-related challenges include: difficult to control synthesis conditions, more significant side reactions with electrolyte, more difficulty maintaining interparticle contact, and low volumetric energy density.[9]

Surface modification is an approach that has been successfully utilized to circumvent some of these challenges surface modification methods include:[45,46] carbon coating,[47] doping,[48] conductive networks,[49] and hierarchical structures.[50] For instance, Ali et al. reported Zn-doped mesoporous TiO_2 microspheres synthesized *via* a combined sol-gel and solvothermal method. As shown in Figure 1-9, the specific capacity of Zn-doped mesoporous TiO_2 microspheres was significantly higher than that of the bare TiO_2 nanopowder at high charge/discharge rates (75 mAh g^{-1} at 10 C vs. 25 mAh g^{-1} for undoped TiO_2). More importantly, doped TiO_2 delivered a good cyclic stability when tested at 1C for 100 cycles; the capacity retention ratio after 100 cycles was 80%.[48]

In addition, Cui's group demonstrated the design of the hierarchical sulphur-TiO_2 yolk-shell nanostructures with internal void space to accommodate the volume expansion of sulphur (Figure 1-10a). This specific yolk-shell exhibited an initial specific capacity of 1030 mAh g^{-1} at 0.5 C and long cycling stability over 1000 charge/discharge cycles, with a capacity decay as small as 0.033% per cycle (Figure 1-10b). While further cycling at 0.5, 1 and 2 C, this hierarchical nanostructured

sample still showed high reversible capacities of 810, 725 and 630 mAh g^{-1}, respectively (Figure 1-10c).[50]

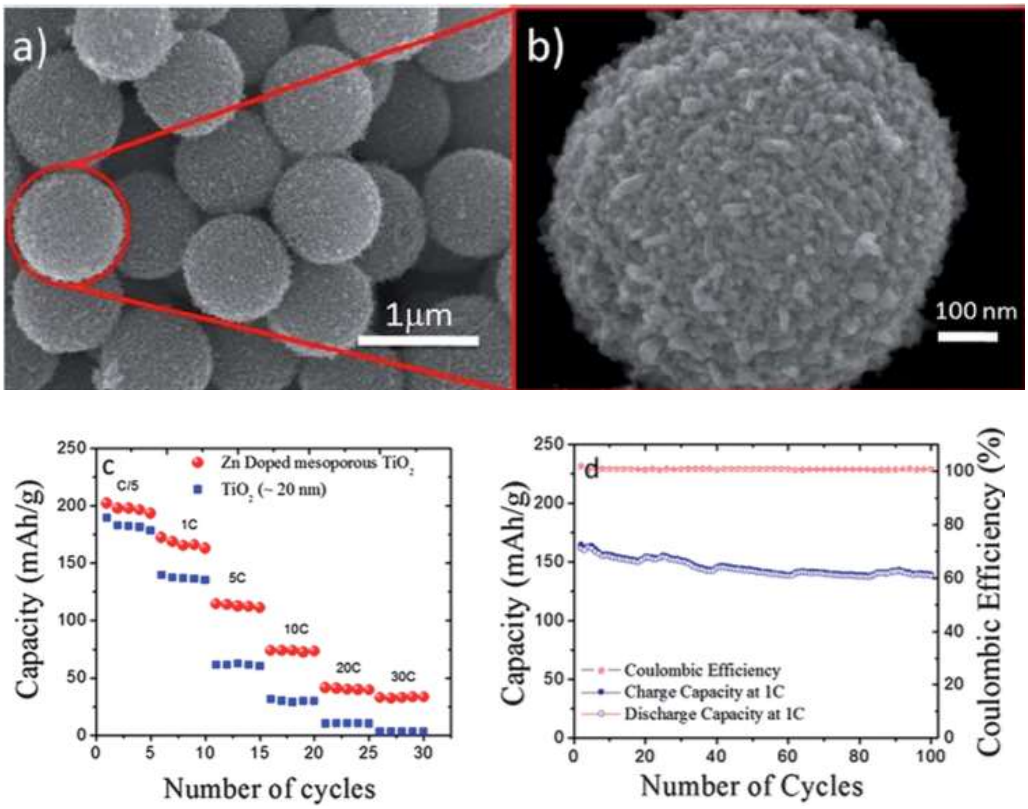

Figure 1-9. SEM images of Zn-doped mesoporous TiO_2 microspheres a, b), c) Discharge capacity of Zn-doped mesoporous TiO_2 microspheres and anatase TiO_2 nanopowder tested at different current rates, d) Cycling performance and Coulombic efficiency of Zn-doped mesoporous TiO_2 up to 100 cycles at 1 C. Reproduced with the permission from ref. 48 (Copyright 2012 Royal Society of Chemistry).

The above examples demonstrate that various surface modification methods are useful to improve disadvantages of applying nanomaterials in LIBs. Even though important progress has been made so far, it deserves to be explored further for high performance electrodes in LIBs. Meanwhile, more efforts should also be devoted to understanding the underlying mechanism for performance improvement by surface modification.

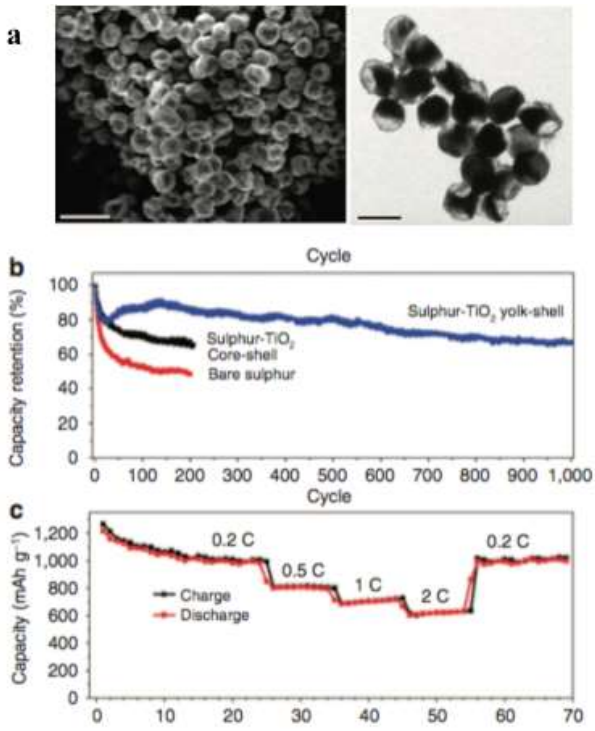

Figure 1-10. a) SEM and TEM image of prepared sulfur-TiO_2 yolk-shell hierarchical nanostructures, b) Capacity retention of sulfur-TiO_2 cycled at 0.5C, in comparison with bare sulfur and sulphur-TiO_2 core-shell nanoparticles, c) Charge/discharge capacity of sulfur-TiO_2 yolk-shell nanostructures cycled at various current rates from 0.2 to 2 C. Reproduced with the permission from ref. 50 (Copyright 2013 Nature Publishing Group).

D. Overview and Outline of This Thesis

The broad goal of this research is to improve performance of LIBs by development of novel anodes with high specific capacity, low cost, and environmentally friendly surface-modified nanomaterials. To achieve this goal, two aspects of work need to be done, which include an understanding of materials synthesis and processing and ultimately improve device performance and an understanding of how prepared materials affect device performance. Thus, the nature of this work requires iteratively synthesizing and characterizing materials, testing electrochemical properties,

understanding structure-property relationships and returning to the synthesis process for better materials. The connecting theme among all the materials research in this work is the ultimate enhancement of LIBs by applying surface modification methods, and the detail objectives in this thesis are shown as follows:

1. Synthesis of Surface-Modified Nanomaterials

1) To develop scalable methods to produce morphology controlled TiO_2, $Li_4Ti_5O_{12}$, and MoS_2 as potential anode materials, such as, nanosheet-based spheres TiO_2, porous $Li_4Ti_5O_{12}$ and so on. A relation between different experimental parameters and the morphology of prepared samples was established.

2) To explore feasible and energy-efficient ion-exchange methods to modify the surface of TiO_2 and $Li_4Ti_5O_{12}$ nanostructures for potential anode application. The influence of these treatments on the crystal structure and morphology of these materials were investigated.

3) To investigate the enhanced effect of TiO_2 phase on the electrochemical performance of $Li_4Ti_5O_{12}/TiO_2$ nanocomposite. In addition, the underlying mechanism of TiO_2 second phase was revealed and discussed.

4) To develop kinds of hierarchical nanomaterials ($Li_4Ti_5O_{12}/MoS_2$, TiO_2/MoS_2) with high electrochemical performance in LIBs. Different substrates, including $Li_4Ti_5O_{12}$ nanosheet arrays and MoS_2 nanospheres were used in the various systems.

2. Morphology and Structural Characterization

The morphology of obtained samples was characterized with scanning electron microscopy and Transmission electron microscopy, respectively. The phase structure

was determined by X-ray diffraction. The surface element composition was measured by energy dispersive spectroscopy and X-ray photoelectron spectroscopy. And the specific surface area of the obtained samples was calculated using the nitrogen adsorption-desorption measurements.

3. Electrochemical Performance Evaluation

Lithium ion battery performance tests were carried out with a half-cell configuration using CR-2032 coin cells. Li foil was used as both the counter and reference electrode. The electrodes were assembled in an Argon-filled glove box. Galvanostatic discharge/charge tests were performed using an Arbin-BT 2000 measurement system at different current densities at various temperatures (25, 55 °C and so on). Electrochemical impedance spectroscopy and cyclic voltammetry studies were carried out on a CHI650E electrochemical workstation.

References

[1] M.E. Mann, R.S. Bradley, and M.K. Hughes, "Global-Scale Temperature Patterns and Climate Forcing Over the Pase Six Centuries," *Nature,* **392** 779 (1998).

[2] M.E. Mann, Z. Zhang, M.K. Hughes, R.S. Bradley, S.K. Miller, S. Rutherford, and F. Ni, "Proxy-based Reconstructions of Hemispheric and Global Surface Temperature Variations Over the Past Two Millennia," *Proc. Natl. Acad. Sci.*, USA **105** 13252 (2008).

[3] N. Armaroli, and V. Balzani, "The Future of Energy Supply: Challenges and Opportunities,"*Angew. Chem. Int. Ed.,* **46** 52-66 (2007).

[4] Y. Wang, and G. Cao, "Developments in Nanostructured Cathode Materials for High-Performance Lithium-Ion Batteries," *Adv. Mater.,* **20** 2251-2269 (2008).

[5] L. Carrette, K.A. Friedrich, and U. Stimming, "Fuel Cells-Fundamentals and Applications," *Fuel Cells,* **1** 5-33 (2001).

[6] H.B. Goyal, Diptendu Seal, and R.C. Saxena, “Bio-fuels from Thermochemical Conversion of Renewable Resources: A Review,” *Renew Sust. Energy Rev.,* **12** 504-517 (2008).

[7] J.M. Tarascon, and M. Armand, “Issues and Challenges Facing Rechargeable Lithium Batteries,” *Nature,* **414** 359 (2001).

[8] Advances in Lithium-Ion Batteries (Eds: W. van Schalkwijk, B.Scrosati), Springer, Berlin 2002.

[9] P.G. Bruce, B. Scrosati, and J.-M. Tarascon, “Nanomaterials for Rechargeable Lithium Batteries,” *Angew. Chem. Int. Ed.,* **47** 2930-2946 (2008).

[10] IPS, “The Rocking Chair Battery (Lithium Ion Battery)” (2013) Availabe at

<https://physicsandsocietybc.wordpress.com/2013/04/03/the-rocking

-chair-battery- lithium-ion-battery/>.

[11] Lithium Batteries Science and Technology (Eds.: G.-A. Nazri, G. Pistoia), Kluwer Academic/Plenum, Boston, 2004.

[12] Y. Cho, S. Lee, Y. Lee, T. Hong, and J. Cho, “Spinel-Layered Core-Shell Cathode Materials for Li-Ion Batteries,” *Adv. Energy Mater.,* **1** 821-828 (2011).

[13] M. S. Whittingham, “Lithium Batteries and Cathode Materials,” *Chem. Rev.,* **104** 4271-4301 (2004).

[14] Y.K. Sun, S.T. Myung, B.C. Park, J. Prakash, I. Belharouak, and K. Amine, “High-energy Cathode Material for Long-life and Safe Lithium Batteries,” *Nat. Mater.,* **8** 320-324 (2009).

[15] K. Ariyoshi, Y. Maeda, T. Kawai, and T. Ohzuku, “Effect of Primary Particle Size upon Polarization and Cycling Stabliltiy of 5-V Lithium Insertion Material of $Li[Ni_{1/2}Mn_{3/2}]O_4$,” *J. Electrochem. Soc.,* **158** A281-A284 (2011).

[16] W.B. Luo, X.H. Li, and J.R. Dahn, “Synthesis, Characterization, and Thermal Stability of $Li[Ni_{1/3}Mn_{1/3}Co_{1/3-z}(MnMg)_{z/2}]O_2$,” *Chem. Mater.,* **22** 5065-5073 (2010).

[17] M.S. Whittingham, “Mechansim of Reduction of the Fluorographite Cathode,” *J. Electrochem. Soc.,* **122** 526-527 (1975).

[18] W.C. West, N.V. Myung, J.F. Whitacre, and B.V. Ratnakumar, “Electrodeposited Amorphous Manganese Oxide Nanowire Arrays for High Energy and Power Density Electrodes,” *J. Power Sources,* **126** 203-206 (2004).

[19] R. Marom, S.F. Amalraj, N. Leifer, D. Jacob, and D. Aurbach, “A Review of Advanced and Practical Litium Battery Materials,” *J. Mater. Chem.,* **21** 9938-9954 (2011).

[20] N.-S Choi, Z. Chen, S.A. Freunberger, X. Ji, Y.-K. Sun, K. Amine, G. Yushin, L. F. Nazar, J. Cho, and P.G. Bruce, “Challenges Facing Lithium Batteries and Electrical Double-Layer Capacitors,” *Angew. Chem. Int. Ed.,* **51** 9994-10024 (2012).

[21] M. Armand, and J.M. Tarascon, “Buidling Better Batteries,” *Nature,* **451** 652-657 (2008).

[22] E. Peled, “The Electrochemical Behavior of Alkali and Alkaline Earth Metals in Nonaqueous Battery Systems-The Solid Electrolyte Interpahse Model,” *J. Electrochem. Soc.,* **126** 2047-2051 (1979).

[23] R. Fong, U. Von Schen, and J.R. Dahn, “Studies of Lithium Intercalation into Carbons Using Nonaqueous Electrochemical Cells,” *J. Electrochem. Soc.,* **137** 2009-2013 (1990).

[24] Z. Chen, Y. Qini, Y. Ren, W. Lu, C. Orendorfff, E.P. Roth, and K. Amine, “Multi-Scale Study of Thermal Stability of Lithiated Graphite”, *Energy Environ. Sci.,* **4** 4023-4030 (2011).

[25] L. Ji, Z. Lin, M. Alcoutlabi, and X. Zhang, “Recent Developments in Nanostructured Anode Materials for Rechargeable Lithium-Ion Batteries”, *Energy Environ. Sci.,* **4** 2682-2699 (2011).

[26] M. Herstedt, M. Stjerndahl, T. Gustafsson, and K. Edstrom, “Anion Receptor for Enhanced Thermal Stability of the Graphite Anode Interface in a Li-Ion Battery”, *Electrochem. Commun.,* **5** 467-472 (2003).

[27] M. Holzapfel, H. Buqa, W. Scheifele, P. Novak and F.M. Petrat, “A New Type of Nano-Sized Silicon/Carbon Composite Electrode for Reversible Lithium Insertion”, *Chem. Commun.,* **12** 1566-1568 (2005).

[28] C.M. Park, J.H. Kim, H. Kim and H.J. Sohn, “Li-Alloy Based Anode Materials for Li Secondary Batteries”, *Chem. Soc. Rev.,* **39** 3115-3141 (2010).

[29] W.J. Zhang, “Lithium Insertion/Extraction Mechanism in Alloy Anodes for Lithium-Ion Batteries”, *J. Power Sources,* **196** 877-885 (2011).

[30] L.W. Ji, K.H. Jung, A.J. Medford and X.W. Zhang, “Electrospun Polyacrylonitrile Fibers with Dispersed Si Nanoparticles and Their Electrochemical Behaviors after Carbonization”, *J. Mater. Chem.,* **19** 4992-4997 (2009).

[31] J. Jiang, Y. Li , J. Liu, X. Huang, C. Yuan, and D. Lou, "Recent Advances in Metal Oxide-based Electrode Architecture Design for Electrochemical Energy Storage," *Adv. Mater.,* **24** 5166-5180 (2012).

[32] C. M. Park, J. H. Kim, H. Kim and H. J. Sohn, "Li-Alloy Based Anode Materials for Li Secondary Batteries", *Chem. Soc. Rev.,* **39** 3115-3141 (2010).

[33] J. Cabana, L. Monconduit, D. Larcher and M.R. Palacin, "Beyond Intercalation-Based Li-Ion Batteries: The State of the Art and Challenges of Electrode Materials Reacting Through Conversion Reactions", *Adv. Mater.*, **22** E170-E192 (2010).

[34] L. J. Zhi, Y. S. Hu, B. El Hamaoui, X. Wang, I. Lieberwirth, U. Kolb, J. Maier and K. Mullen, "Precursor-Controlled Formation of Novel Carbon/Metal and Carbon/Metal Oxide Nanocomposites", *Adv. Mater.*, **20** 1727-1731 (2008).

[35] J. Jiang, Y. Li , J. Liu, X. Huang, C. Yuan, and D. Lou, "Recent Advances in Metal Oxide-based Electrode Architecture Design for Electrochemical Energy Storage," *Adv. Mater.,* **24** 5166-5180 (2012).

[36] S.T. Myung, N. Takahashi, S. Komaba, C.S. Yoon, Y.K. Sun, K. Amine, and H. Yashiro, "Nanostructured TiO_2 and Its Application in Lithium-Ion Storage," *Adv. Funct. Mater.*, **21** 3231-3241 (2011).

[37] D. Dambournet, I. Belharouak and K. Amine, "Tailored Preparation Methods of TiO_2 Anatase, Rutile, Brookite: Mechansim of Formation and Electrochemical Properties," *Chem. Mater.,* **22** 1173-1179 **(**2010).

[38] C. Jiang, M. Wei, Z. Qi, T. Kudo, I. Honma and H. Zhou, "Particle Size Dependence of the Lithium Storage Capability and High Rate Performance of Nanocrystalline Anatase TiO_2 Electrode," *J. Power Sources,* **166** 239-243 (2007).

[39] G.G. Amatucci, F. Badway, A.D. Pasquier, and T. Zheng, "An Asymmetric Hybrid Nonaqueous Energy Storage Cell", *J. Electrochem. Soc.,* **148** A930-A939 (2001).

[40] Y. Shi, L. Wen, F. Li, H. M. Cheng, "Nanosized $Li_4Ti_5O_{12}$/Graphene Hybrid Materials with Low Polarization for High Rate Lithium Ion Batteries", *J. Power Sources*, **196** 8610-8617 (2011).

[41] E.M. Sorensen, S.J. Barry, H.-K. Jung, J.R. Rondinelli, J.T. Vaughey, and K.R. Poeppelmeier, "Three-Dimensionally Ordered Macroporous $Li_4Ti_5O_{12}$: Effect of Wall Structure on Electrochemical Properties", *Chem. Mater.*, **18** 482-489 (2006).

[42] Y.Q. Wang, L. Gu, Y.G. Guo, H. Li, X.Q. He, S. Tsukimoto, Y. Ikuhara and L.-J. Wan, "Rutile-TiO_2 Nanocoating for a High-Rate $Li_4Ti_5O_{12}$ Anode of a Lithium-Ion Battery," *J. Am. Chem. Soc.*, **134** 7874-7879 (2012).

[43] M. R. Jo, Y. S. Jung and Y.-M. Kang, "Tailored $Li_4Ti_5O_{12}$ Nanofibers with Outstanding Kinetics for Lithium Rechargeable Batteries," *Nanoscale*, **4** 6870-6875 (2012).

[44] S. Chen, Y. Xin, Y. Zhou, Y. Ma, H. Zhou, and L. Qi, "Self-Supported $Li_4Ti_5O_{12}$ Nanosheet Arrays for Lithium Ion Batteries with Excellent Rate Capability and Ultralong Cycle Life," *Energy Environ. Sci.*, **7** 1924-1930 (2014).

[45] R.S. Devan, R.A. Patil, J.-H. Lin, and Y.-R. Ma, "One-Dimensional Metal Oxide Nanostructures: Recent Developments in Synthesis, Characterization, and Applications," *Adv. Funct. Mater.*, **22** 3326-3370 (2012).

[46] A.S. Aricò, P.G. Bruce, B. Scrosati, J.-M. Tarascon, and W. Van Schalkwijc, "Nanostructured Materials for Advanced Energy Conversion and Storage Devices," *Nat. Mater.*, **4** 366-377 (2005).

[47] M. Pfanzelt, P. Kubiak, U. Hoermann, U. Kaiser, M. Wohlfahrt-Mehrens, "Preparation, Characterization, and Electrochemical Performances of Carbon-Coated TiO_2 Anatase," *Ionics*, **15** 657-663 (2009).

[48] Z. Ali, S.N. Cha, J.I. Sohn, I. Shakir, C. Yan, J.M. Kim, and D.J. Kang, "Design and Evaluation of Novel Zn Doped Mesoporous TiO_2 Based Anode Material for Advanced Lithium Ion Batteries," *J. Mater. Chem.*, **22** 17625-17629 (2012).

[49] Y.Q. Wang, L. Gu, Y.G. Guo, H. Li, X.Q. He, S. Tsukimoto, Y. Ikuhara and L.-J. Wan, "Rutile-TiO_2 Nanocoating for a High-Rate $Li_4Ti_5O_{12}$ Anode of a Lithium-Ion Battery," *J. Am. Chem. Soc.*, **134** 7874-7879 (2012).

[50] Z.W. Seh, W. Li, J.J. Cha, G. Zheng, Y. Yang, M.T. McDowell, P.-C. Hsu, and Y. Cui, "Sulphur–TiO_2 yolk–shell nanoarchitecture with internal void space for long-cycle lithium–sulphur batteries", *Nat. commun.*, **4** 133 (2013).

DESIGNING ION-DOPED TiO_2 NANOSTRUCTURES AS ANODE MATERIALS FOR LITHIUM-ION BATTERIES

A. Introduction

Today, the demand for clean and sustainable energy is becoming more and more critical owing to climate change and the decreasing availability of fossil fuels. As powerful energy storage devices, rechargeable lithium-ion batteries (LIBs) have demonstrated their significant roles in mobile applications.[1-5] However, to meet the needs of the soaring market, new generations of LIBs are required with increased power density, wider work-temperature range, improved safety, and lower cost. After decades of research, many studies have been published around the world,[6-8] and anode materials will be a key factor in improving the performance of lithium-ion batteries due to their impressively higher capacities than cathode materials. However, a large fraction of anode materials suffers poor cyclic stabilities during repeated lithium ion insertion/extraction processes due to the complicated properties of their electrode/electrolyte interface, well known as solid electrolyte interface (SEI). As a result, most anode materials studied in the lab exhibit poor performance in commercial applications. So far, graphite has been used as the anode for most LIBs in practice because of its low electric potential (0.1 V vs. Li^+/Li) and high capacity (~300 mAg^{-1}).[9] However, problems include low power density and decomposition of the solid electrolyte interphase (SEI) on lithiated graphite at elevated temperatures, severely limiting its application in future development.[10-11] Therefore, new materials

for overcoming these problems need to be developed. Compared to graphite, titanium dioxide (TiO_2) has a relatively higher lithium insertion/extraction voltage (~1.7 V vs Li^+/Li), which can improve the safety of batteries by reducing the excessive formation of SEI and lithium plating on anodes.[12-13] Furthermore, TiO_2 has promising electrochemical properties, high chemical stability, and non-toxicity.[14-15] These characteristics make it a favorable candidate to replace graphite as an anode material for a new generation of LIBs used in some specific applications requiring fast response and high stability in numerous cycles, i.e. start-stop batteries.

Among different TiO_2 polymorphs, anatase TiO_2 is considered as one of most promising candidates for energy storage due to its easy fabrication, fast Li^+ insertion–extraction reactions, and high theoretical insertion capacity.[16-19] However, in most applications the real capacity of anatase TiO_2 is lower than the predicted maximum of 335 $mAhg^{-1}$ [15,20] due to the phase transition from tetragonal crystal structure to orthorhombic crystal structure and the resulting 1-D diffusion limitation in the Li-ordered $Li_{0.5}TiO_2$.[21] Moreover, it also has a low intrinsic electrical conductivity (10^{-12} scm^{-1}) for application in practice.[22,23] To solve this problem, various TiO_2 nanostructures have been fabricated in order to improve its Li-ion intercalation performance by shortening Li-ion and electron diffusion paths, enlarging the electrode/electrolyte interfacial area, and facilitating strain relaxation during the insertion/extraction processes.[24-27] However, more severely capacity fading can be observed when applied nanomaterial in some specific situations (elevated temperature, etc.) To solve this problem, one common approach is to modify the

surface of electrodes with transition metal ions, transition metals, transition metal oxides and so on. Many methods have been used to accomplish this, such as solution-based coating,[28] physical vapor deposition (PVD),[29] and atomic layer deposition (ALD).[30] However, these methods require complicated procedures and induce high cost; in addition, it is still not easy to obtain homogeneously modified nanostructures. Therefore, there is an immediate need for a simple, low cost and reliable synthesis method to fabricate homogenously modified TiO_2 that can be used as anodes at elevated temperatures.

In this chapter, we adopt a two-step strategy through the synthesis of two kinds of nanostructured anatase TiO_2 (nanosheet-based spheres, nanoparticles) and doping manganese/nickel ions into the structure *via* an ion-exchange process. These novel nanostructured materials exhibited high capacity and cyclic stability when used as a lithium-ion battery electrode. Therefore, it is promising as the anode material for a new generation of LIBs.

B. Mn-Doped TiO_2 Nanosheet-Based Spheres

1. Experimental procedure

Mn-doped TiO_2 nanosheet-based spheres have been synthesized in three steps. First, TiO_2 nanospheres were prepared *via* a sol-gel process as reported in the literature.[31] In a typical synthesis process, 0.1987 g of hexadecylamine (HDA, 98%, Sigma-Aldrich) was dissolved in 20 ml of anhydrous ethanol (>99.5%, Anhydrous, Sigma-Aldrich), followed by the addition of 0.08 mL of KCl (≥99.0%, Sigma)

solution (0.1 M). Then, 0.4525 ml of titanium (IV) isopropoxide (TIP, 97+%, Alfa Aesar) was added under vigorous stirring for 2 mins. The milky white suspension was kept static for 18 h and then centrifuged; the precipitation was washed with ethanol (200 Proof, Ultra-Pure) three times and dried in air at 40 °C. Then, 0.1 g of as-prepared TiO_2 precursor was dissolved in 20 ml of anhydrous ethanol together with 17 ml of ammonium hydroxide (ACS, 30%, Alfa Aesar) and 3 ml of deionized (DI) water. The mixture was then transferred to a Teflon-lined stainless steel autoclave (Parr Instrument Co.), heated to 130 °C and kept static for 72 h. After this treatment, the autoclave was cooled down to room temperature at a rate of 1 °C min^{-1}. The obtained products were washed with DI water three times and the pH was adjusted to 6 by rinsing with diluted HNO_3 (0.1N, Alfa Aesar) solution. Then, the obtained powders were dispersed in 200 ml of manganese nitrate tetrahydrate (98%, Alfa Aesar) solution (0.09 M) under constant stirring for 2 h. After that, it was washed three times by DI water to remove excess Mn ions and dried in air at 40 °C. Finally, the prepared powders were calcined at 400 °C for 3 h. For comparison, TiO_2 powders without Mn-doping were also calcined under the same conditions. Within this study, the samples are designated as TiO_2-PS (precursor sphere), TiO_2-HT (after hydrothermal treatment), HT-400 (after hydrothermal and calcination without Mn ion doping), HT-Mn-400 (after hydrothermal treatment, Mn ion-exchange process and calcination).

The morphologies of obtained samples were characterized by scanning electron microscopy (SEM, FEI Quanta 200) and Transmission electron microscopy (TEM,

JEM-2100F) with the accelerating voltage of 20 kV and 200kV, respectively. The phase structures were determined by X-ray diffraction (XRD, Bruker D2) on a Scintag diffractometer with CuKα_1 radiation (λ= 1.54060 Å) at a scanning rate of 0.017 °s^{-1} in the 2θ range from 5° to 75°. The surface element composition was measured by energy dispersive spectroscopy (EDS) using the FEI Quanta 200 and X-ray photoelectron spectroscopy (XPS, VG Multilab 2000, Thermo Electron Corporation) with A1Kα X-ray as the excitation source. The nitrogen adsorption and desorption isotherms were collected at 77 K in the range of relative pressures of 0.0002-0.99P/P_0 using a TriStar II 3020 surface area and porosity measurement system (Micromeritics Instrument Corp.) and used for measurements of the pore size distribution in the 1.7-300 nm range. After drying the powder under a vacuum at 80 °C for at least 12 h, 50-100 mg of each powder sample was degassed under a N_2 gas flow at 150 °C for at least 1 hr before weighting and gas sorption measurements. The pore size distribution was calculated using the Barrett-Joyner-Halenda (BJH) methods, using Micromeritics DataMaster software.

Electrochemical impedance spectroscopy (EIS) study was carried out using a CHI650E electrochemical workstation. The applied AC perturbation was 5mV and the frequency range was from 100 kHz to 0.1 Hz. The frequency range was from 100 kHz to 0.1 Hz. Lithium ion battery performance tests were carried out with a half-cell configuration using CR-2032 coin cells. Li foil was used as both the counter and reference electrode. The working electrode was prepared by mixing active materials (85%), carbon black (Alfa Aesar, 10%), and polyvinylidene fluoride (PVDF, Alfa

Aesar, 5%) in N-methyl-2-pyrrolidone (NMP, Alfa Aesar). After uniform stirring, the above slurries were coated on copper foil and dried at 120 °C in vacuum for 6 h. Then, the electrode was pressed and cut into disks before assembly in an Argon-filled glove box for coin-cell assembling. 1 M $LiPF_6$ in a mixed solution of ethylene carbonate and diethyl carbonate (1:2 volume ratio, Novolyte, USA) were used as the electrolyte. Galvanostatic discharge/charge tests were performed using an Arbin-BT 2000 measurement system in the potential window of 1-2.5 V versus Li^+/Li at different current densities of 30 mAg^{-1}, 150 mAg^{-1} and 500 mAg^{-1} at both room temperature and 55 °C.

2. Results and discussion

2.1 Characterization of Mn-doped TiO_2 nanosheet-based spheres

As shown in Figure 2-1a, the uniformity of monodisperse spheres were investigated by SEM. The size of a single particle is around 600-700 nm. Figures 2-1b and c show the low and high magnification SEM images of hydrothermally prepared nanosheet-based spheres (TiO_2-HT). Compared to the sphere precursor, their morphology changes dramatically. It can be observed that the spheres turn into flower-like structures formed by nanoflakes. Figures 2-1d and e show the SEM images of samples after calcination at 400 °C for 3 h without and with Mn ion doping (HT-400 and HT-Mn-400). As shown in these two images, little morphology difference can be found between them and they are also similar to TiO_2-HT (Figure 2-1b). Figure 2-1f shows the TEM image of HT-Mn-400. It can be found that HT-Mn-400 possesses a solid sphere core. Although SEM and TEM images do not

show noticeable morphology change among these three samples, nitrogen adsorption isotherms and XRD patterns reveal obvious differences between them in surface area and crystallinity (To be discussed later).

To investigate the doping effect of the ion-exchange process, surface element compositions of HT-400 and HT-Mn-400 were studied by EDS and XPS. As shown in Figure 2-2, HT-400 has no manganese element peak existing in the spectrum (Figure 2-2a) while HT-Mn-400 has visible manganese element peaks (Figure 2-2b). Furthermore, the molar percentage of Mn ions in HT-Mn-400 is 3.1%, which is much higher than the EDS test result of 1.9% of TiO_2 nanotubes reported by Szirmai *et al* using a similar ion-exchange process.[32]

Figure 2-3 shows the XPS spectra of HT-400 and HT-Mn-400. Mn 2p peaks are clearly identified in the spectrum of HT-Mn-400, while there is no corresponding peaks existing in the spectrum of HT-400 (Figure 2-3a). It agrees well with the EDS result, which indicates that ion-exchange processing is an effective method to dope Mn ions in the TiO_2 nanostructure. High resolution XPS spectrum in Figure 2-3b shows that Mn 2p peaks are with binding energies of 641.4 eV for $2p_{2/3}$ and 653.9 eV for $2p_{1/2}$, suggesting that the oxidation state of Mn ions is 2^+. And it can be further confirmed through the unique satellite feature around 647 eV, which is not shared by the other oxidation states of Mn ions.[33-35] This result indicates that the Mn ions oxidation state will not change after calcination at 400 °C for 3 h.

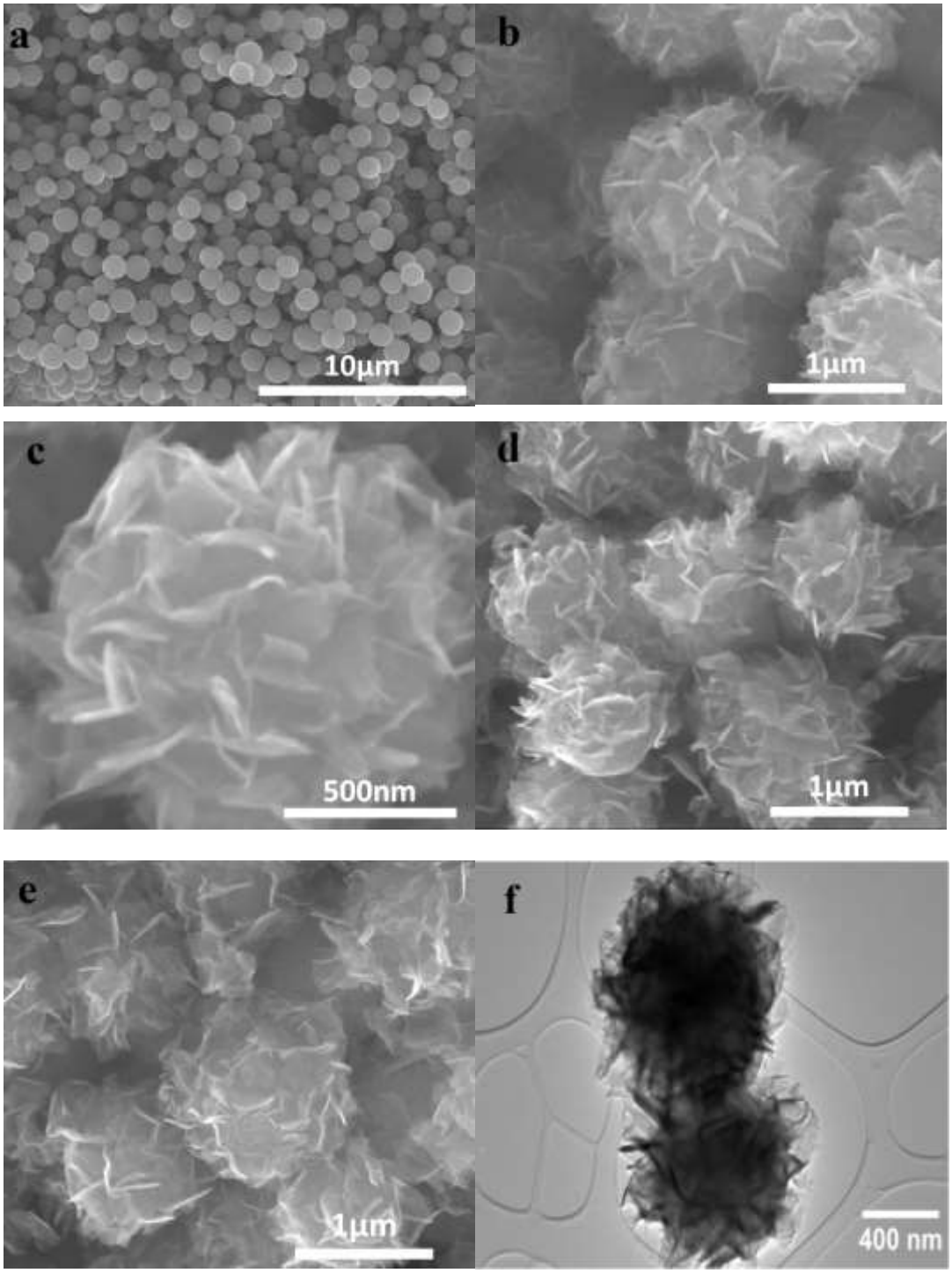

Figure 2-1. SEM and TEM images of TiO_2 nanostructures obtained after different processes: (a) TiO_2 nanospheres (TiO_2-PS), (b, c) low and high mignification SEM images of TiO_2 nanosheet-based spheres synthesized via hydrothermal process (TiO_2-HT), (d) TiO_2 nanosheet-based spheres calcined at 400 °C for 3 h (HT-400), (e, f) SEM and TEM images of TiO_2 nanosheet–based spheres doped by manganese ions, and then calcined at 400 °C for 3 h (HT-Mn-400).

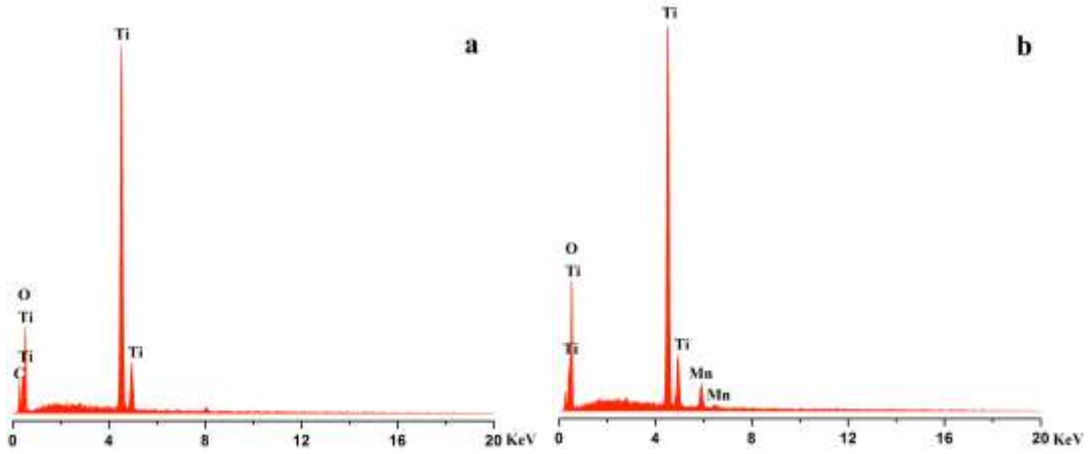

Figure 2-2. EDS spectra of TiO_2 samples treated before (a) and after (b) Mn ion-exchange process.

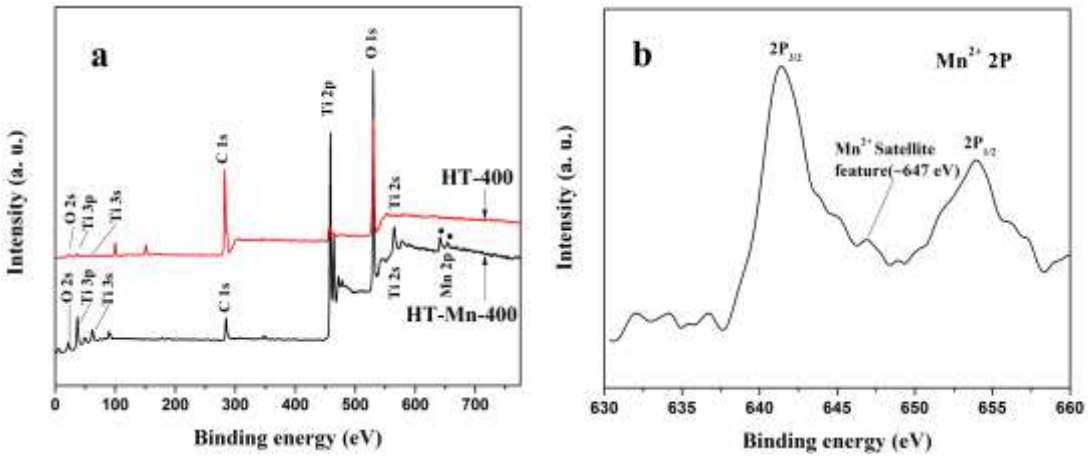

Figure 2-3. XPS spectra of TiO_2 samples: (a) Wide-scan spectra of HT-400 and HT-Mn-400 (b) High resolution XPS Mn 2p peaks of HT-Mn-400.

To get more insights into the influence of the doping and calcination processes on TiO_2 samples, nitrogen adsorption-desorption measurments were conducted to characterize the specific surface areas of TiO_2-PS, TiO_2-HT, HT-400 and HT-Mn-400. Figure 2-4 shows their adsorption and desorption isotherm curves. The isotherm curves of TiO_2-HT, HT-400 and HT-Mn-400 exhibit the typical adsorption hysteresis that belongs to type IV isotherm curves, indicating that these three samples have mesoporous structures.[36] Their specific surface areas are calculated using the BJH method to be 110.7 $m^2 g^{-1}$, 230.7 $m^2 g^{-1}$ and 222.0 $m^2 g^{-1}$, respectively. All of

these samples have higher specific surface areas than TiO_2-PS (4.5 $m^2 g^{-1}$), which has type II isotherm curve with little porosity. Furthermore, it also can be found that TiO_2-HT and HT-Mn-400 possess nearly the same specific surface area, whereas HT-400 possesses only about half as much. It is well-known that a decrease in surface area is a common phenomenon after calcination because of particle agglomeration.[37] However, the surface area of Mn-doped TiO_2 does not show any decrease after calcination compared to TiO_2-HT, which did not receive any heat treatment. When the calcination temperature was raised to 500 °C, the morphology of Mn ions doped sample exhibits noticeable change. Nanosheets of the spheres become thicker and start to agglomerate with each other (Figure 2-5). Above results indicate that Mn ions doping will enhance the structure stability of the TiO_2 nanosheet-based spheres when the calcination temperature is lower than 500 °C.

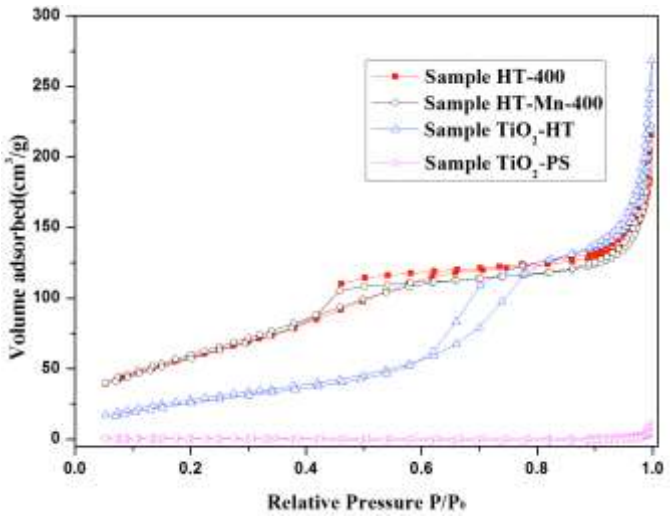

Figure 2-4. Nitrogen sorption isotherms of TiO_2-PS, TiO_2-HT, HT-400 and HT-Mn-400.

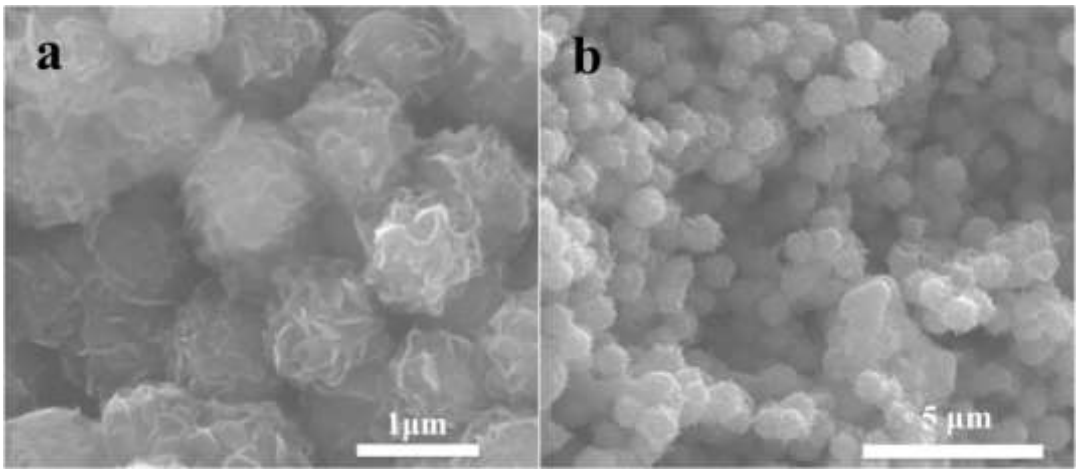

Figure 2-5. SEM images of Mn ions doped HT-TiO_2 calcined at 500 ºC for 3h (HT-Mn-500).

Figure 2-6 shows the XRD patterns of TiO_2-HT, HT-400 and HT-Mn-400. As can be found, TiO_2-HT shows a diffraction peak of $2\theta \approx 9.7^{\circ}$, which is assigned to the protonated dititanate (PDF, 047-0124). When calcined at 400 °C for 3 h, without Mn ion doping, TiO_2 nanosheet-based spheres (HT-400) show a typical anatase crystal structure. However, when Mn ions are doped *via* ion-exchange before heat treatment (HT-Mn-400), there is almost negligible intensity of anatase peaks in the XRD pattern. Even when the calcination temperature is increased to 500 °C, the anatase peak of Mn ions doped TiO_2 is still not well-defined (Figure 2-7). In addition, there is no manganese compounds peaks existing in the XRD pattern of HT-Mn-400, which suggests that Mn ions have been inserted into the lattic of TiO_2. As demonstrated by relevant studies, impurity ions could act as a strong barrier to the phase transition during calcination. Similar inhibition effects on the TiO_2 phase transition have been reported by other groups doping with various ions and methods.[28,38] On the basis of the BET and XRD tests, we can conclude that Mn ions doping process improved

the structure stability and inhibited the crystallization of the TiO_2 nanosheet-based structure.

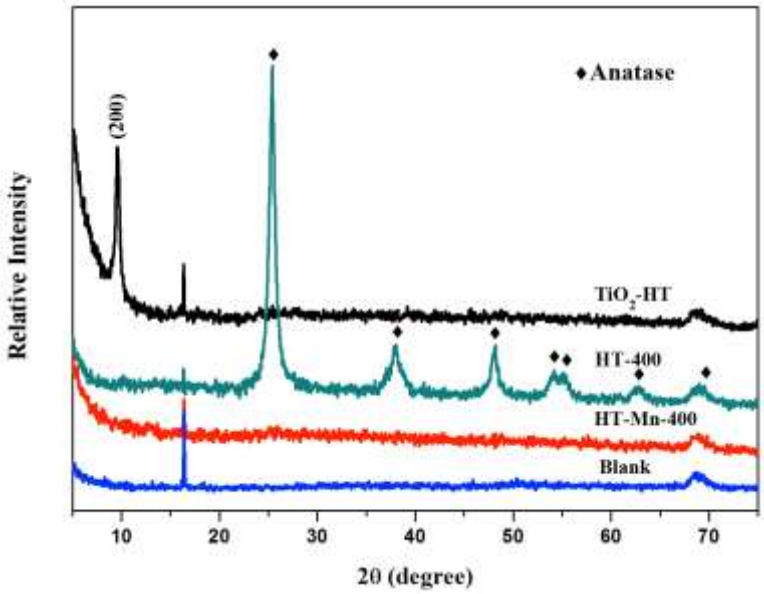

Figure 2-6. XRD patterns of TiO_2-HT, HT-400, HT-Mn-400 and the blank sample holder, the diffraction peaks of $2\theta \approx 16^\circ$ and 74° existing in all four samples are the background peaks of substrate.

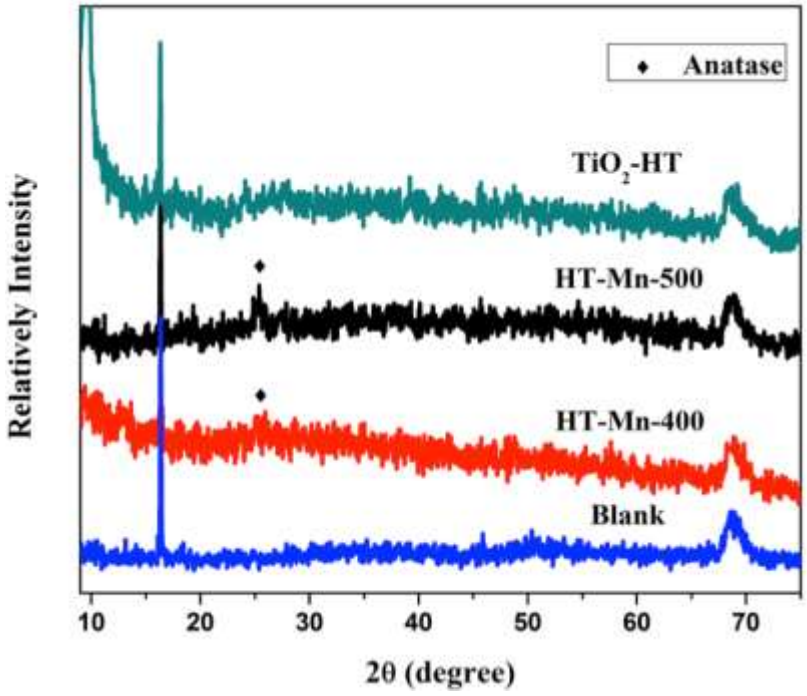

Figure 2-7. XRD patterns of HT-Mn-400, HT-Mn-500, TiO_2-HT and the blank sample holder. The diffraction peaks of $2\theta \approx 16^\circ$ and 74° existing in the samples are the background peaks of substrate.

2.2 Growth mechanism of Mn-doped TiO_2 nanosheet-based spheres

Based on above results, we believe that the formation of these nanosheet-based spheres *via* hydrothermal processing is a modified dissolution-recrystallization process as reported in the literature.[39-42] The growth process is depicted schematically in Figure 2-8. First, in a hot and alkaline condition, the precursors of TiO_2 nanospheres were partially dissolved in the mother solution to form a small quantity of $Ti(OH)_4$ and a large quantity of free titanate ions after complex chemical reactions. As the process continues and the mother solution becomes supersaturated, the dissolved ions will initiate heterogeneous nucleation and regrowth on the surface of the reacted TiO_2 spheres to form flowerlike sphere structures, which is driven by thermodynamic force to reduce the structure's total surface energy.[43] As the mass diffusion and ripening process proceeded, nanosheets continued to grow until small nanoparticles were totally consumed; thereby the uniform nanosheet-based spheres were fabricated *via* a dissolution-recrystallization process.

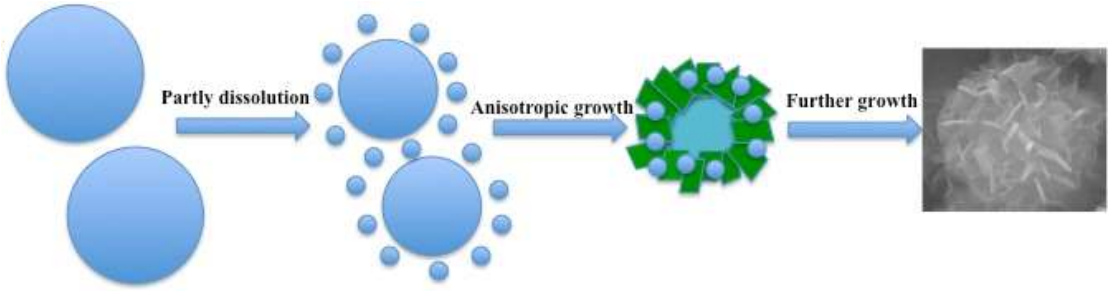

Figure 2-8. Growth schematic of TiO_2 nanosheet-based spheres prepared by a hydrothermal process.

Furthermore, it can also be deduced that the obtained TiO_2 nanosheets have been converted to ammonium titanate $[(NH_4)_2Ti_2O_5 \cdot H_2O]$ at least on the surface of the structure during this hydrothermal process according to findings of similar

experiments in the literature.[40, 43-46] NH_4^+ was later replaced by H^+ in acid solutions during the washing process and [$(NH_4)_2Ti_2O_5 \cdot H_2O$] was converted to protonated dititanate ($H_2Ti_2O_5 \cdot H_2O$). The existence of $H_2Ti_2O_5 \cdot H_2O$ was confirmed by the XRD diffraction pattern of TiO_2-HT. As shown in Figure 2-6, after hydrothermal and acid washing treatment, the nanosheet structure of TiO_2-HT exhibits a strong peak at $2\theta \approx 9.7^\circ$ corresponding to the (200) lattice plane that fits the PDF card of $H_2Ti_2O_5 \cdot H_2O$ (047-0124)'s first strongest diffraction peak. It indicates that protonated dititanate exists in HT-400. Then, protons in as-prepared [$H_2Ti_2O_5 \cdot H_2O$] were exchanged by manganese ions (Mn^{2+}) to obtain Mn^{2+} doped $Mn_xH_{4-x}Ti_2O_6$.

Compared to NaOH solution which is usually used in the hydrothermal process to obtain $Na_2Ti_3O_7$,[32, 43-46] NH_4^+ can be easily exchanged by H^+ in acidic solutions because of the larger hydrated ionic radius than Na^+,[47] which can increase the amount of obtained [$H_2Ti_2O_5 \cdot H_2O$] for the following Mn^{2+} ion-exchange treatment. Although protonated dititanate has been frequently synthesized *via* hydrothermal growth together with acid solution ion exchange,[40,41,43-46] there are few reports about further ion-exchange of prepared $H_2Ti_2O_5 \cdot H_2O$.[48] Here, we report on further ion-exchange synthesis of Mn-doped TiO_2 nanosheet-based spheres using $H_2Ti_2O_5 \cdot H_2O$ as the precursor.

2.3 Lithium-ion intercalation properties investigation

To study the effects of Mn doping on improving the performance of TiO_2 nanosheet-based spheres as lithium-ion storage electrodes at elevated temperatures, we investigated lithium-ion insertion/extraction properties of HT-Mn-400 by

galvanostatic discharge/charge measurements at both room temperature and 55 °C for 50 cycles. To make comparisons, HT-400 and TiO_2-HT were also tested under identical conditions. As shown in Figure 2-9, measurements at rooms temperatures indicated that all the tested samples possessed similar initial capacities but HT-Mn-400 exhibited better cyclic stability. It is well known that when the testing temperature of lithium ion batteries is increased to more than 50 °C, the capacity of batteries increases at the cost of cyclic stability. So in our study, we are focusing on studying the battery performance at 55 °C. Figure 2-10 shows the discharge and

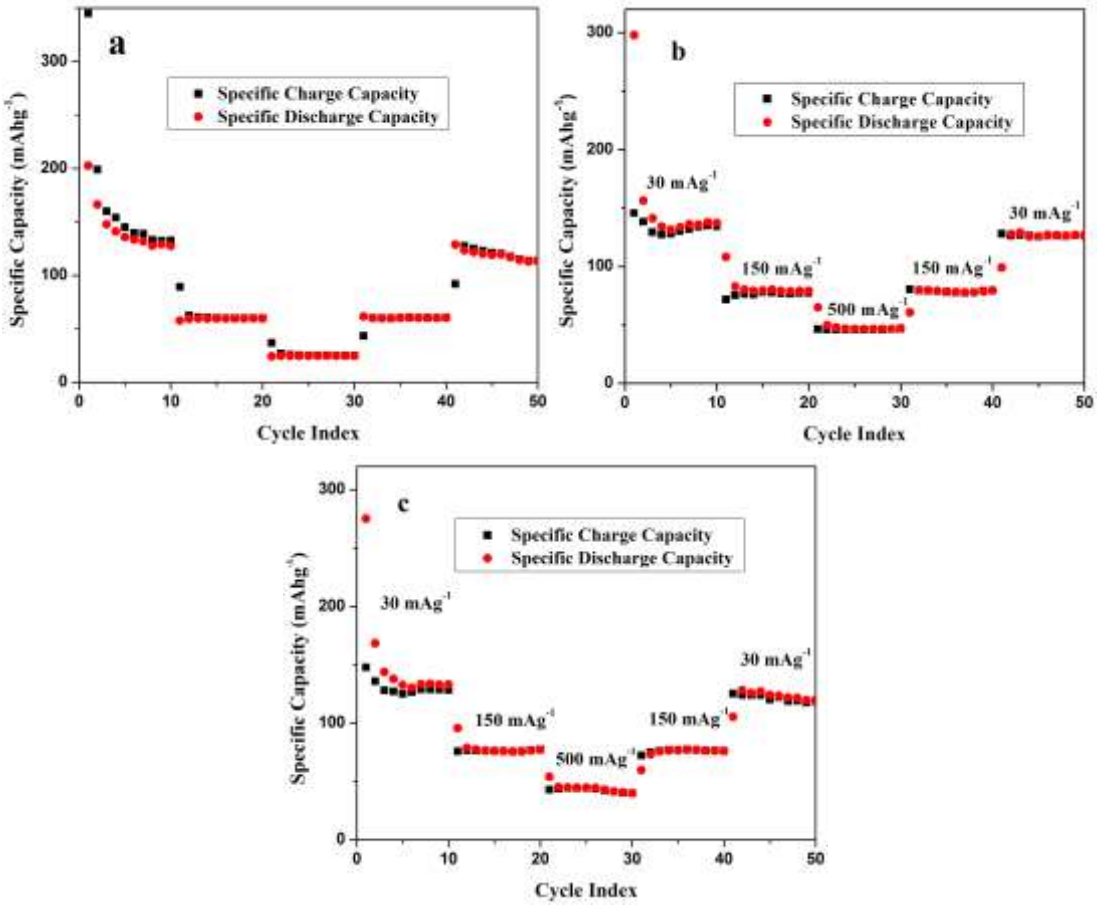

Figure 2-9. Charge/discharge capacity vs. cycle number of (a) HT-400, (b) sample HT-Mn- 400 and (c) TiO_2-HT cycled at different current densities of 30mAg^{-1}, 150 mAg^{-1} and 500mAg^{-1} under room temperature.

charge curves of these three samples in the first and last 3 cycles at a discharge/charge current density of 30 mA g^{-1} at the testing temperature of 55 °C. It is observed that the initial discharge capacities of HT-400, HT-Mn-400 and TiO_2-HT are 201 mAh g^{-1}, 190 mAh g^{-1} and 240 mAh g^{-1}, respectively. As shown in Figure 2-10a, HT-400 shows noticeable plateaus at approximately 1.8 V (discharge process) and 1.9 V (charge process) during the first 3 cycles, which is similar to reported nanostructured anatase.[23,49] During the first discharge process, TiO_2 voltage drops rapidly from the open circuit voltage (OCV) to 1.8 V and reaches a plateau, which suggests that phase transition from a Li-poor phase to a Li-rich phase occurs. After that it gradually decreases to the cut-off voltage of 1.0 V. In the last 3 cycles, the discharge plateaus decline to a lower voltage at approximately 1.5 V and become much less well-defined, while the charge plateaus disappear. Correspondingly, the discharge capacity is only 89 mAh g^{-1} at the 50^{th} cycle. However, this decline is not seen in HT-Mn-400. In contrast to HT-400, the initial discharge curve of HT-Mn-400 exhibits a sloping manner from a much lower OCV as shown in Figure 2-10b, suggesting less pure TiO_2 phase due to Mn-ion doping. In the 2^{nd} cycle, the discharge curve exhibits a much smaller plateau with similar position to that of HT-400. This phenomenon resembles what was reported of V_2O_5 xerogel films with oxygen vacancies on the surface[50] and reveals a more complicated interface formation on HT-Mn-400, which can be ascribed to doped ions on the surface of the nanostructures. In addition, the position and size of these plateaus exhibit little change after cycling. Compared to HT-400 and HT-Mn-400, TiO_2-HT shows a sloping profile of voltage-capacity

relationship during the discharge and charge processes (Figure 2-10c). These curves are typical for electrode materials with amorphous structure due to the absence of heat treatment. In addition, its capacity exhibits noticeable degradation in the initial cycles. XRD patterns of the HT-400 electrode and the HT-Mn-400 electrode after cycling were also studied and compared with those before cycling in Figure 2-11. The HT-400 electrode shows a significant decay on crystallinity. The fine anatase crystal peaks almost disappear after the cycling (Figure 2-11a), while the XRD patterns of the HT-Mn-400 electrode show little peak intensity change before and after cycling (Figure 2-11b).

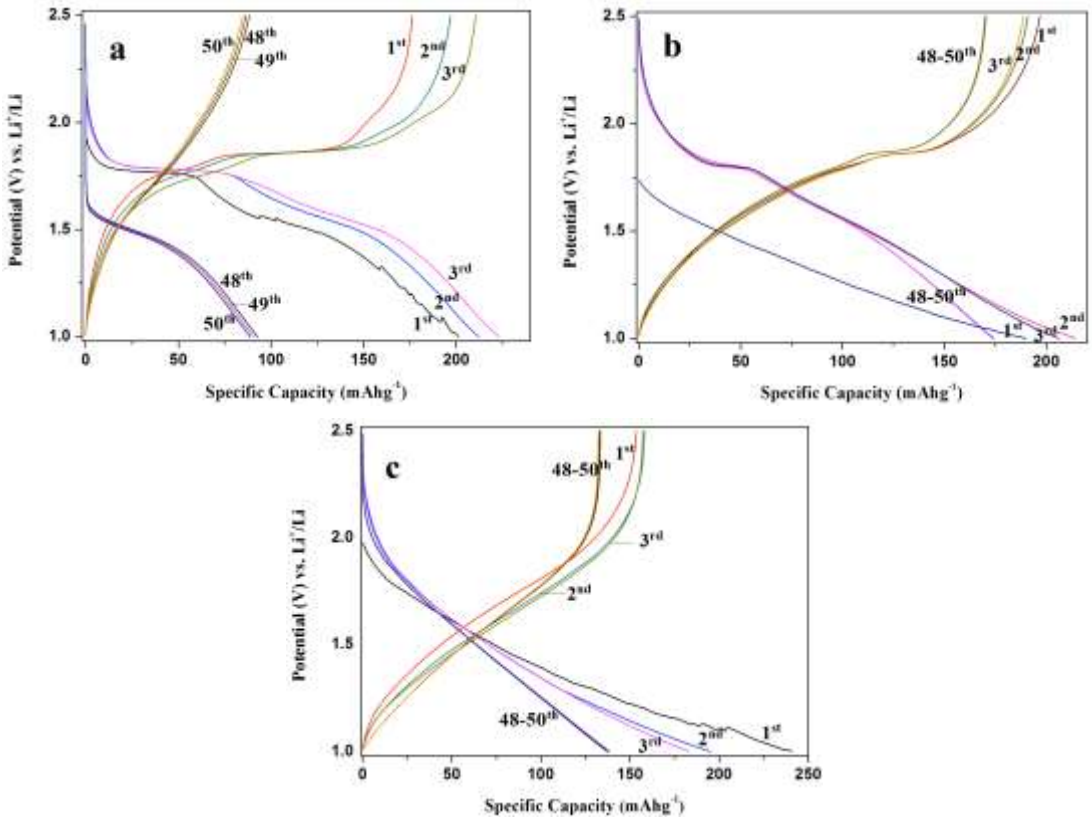

Figure 2-10. Galvanostatic discharge (lithium insertion)/charge (lithium extraction) curves vs. Li^+/Li of (a) HT-400, (b) HT-Mn-400 and (c) TiO_2-HT cycled at a current density of 30 mAg^{-1} in the first 3 and last 3 cycles of the 50-cycle tests.

Above results indicate that anatase structure deteriorates severely during cycling at the elevated temperature for HT-400, while HT-Mn-400 exhibits little structure change in the same process.

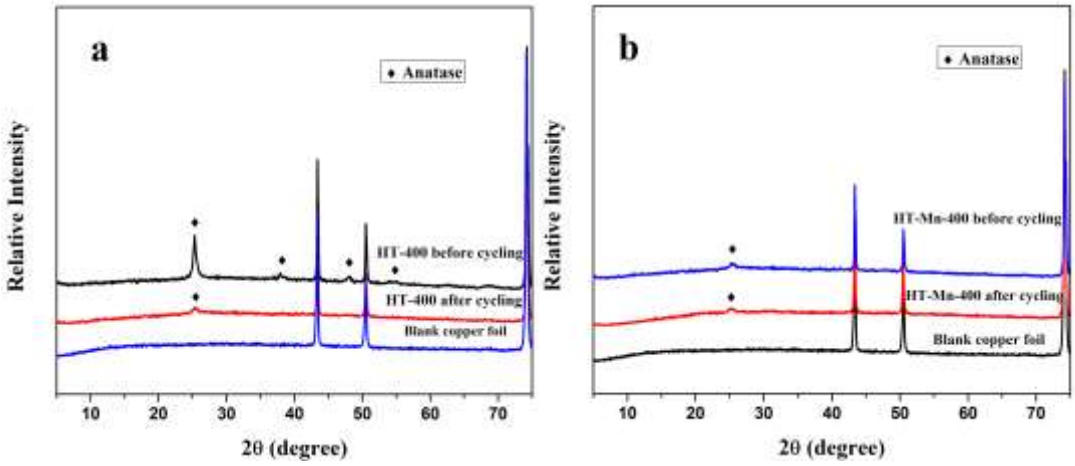

Figure 2-11. XRD patterns of HT-400 a) and HT-Mn-400 b) prepared electrodes before and after cycling.

Figure 2-12 displays the cyclic performance of HT-400, HT-Mn-400 and TiO_2-HT at different current densities of 30 mA g^{-1}, 150 mA g^{-1} and 500 mA g^{-1} in the potential window of 1-2.5 V at the testing temperature of 55 °C. As shown in Figure 2-12a, the discharge capacity of HT-400 increases from 201 mAh g^{-1} to 224 mAh g^{-1} after the first 5 cycles at the discharge current density of 30 mA g^{-1}. However, it drops very quickly in the subsequent 5 cycles to 167 mAh g^{-1} at the same discharge current density. When the discharge current density is increased to 150 mA g^{-1} at the 11^{th} cycle, the capacity drops to 125 mAh g^{-1} when the discharge current density is further increased to 500 mA g^{-1} at the 21^{st} cycle, the discharge capacity drops to 44 mAh g^{-1}. After the discharge current density is changed back to 30 mA g^{-1} at the 41^{st} cycle, the discharge capacity recovers to 69 mAh g^{-1} and increases to 89 mAh g^{-1} at the 50^{th} cycle, with a capacity retention ratio of 44.1 % after 50 cycles at different current

densities. In contrast, HT-Mn-400 starts with a little lower initial discharge capacity of 190 mAh g^{-1} but experiences much less capacity degradation in the first 10 cycles. The rate capability of HT-Mn-400 is also obviously better than HT-400: its discharge capacity is 169 mAh g^{-1} at a current density of 150 mAh g^{-1} and 147 mAh g^{-1}at a current density of 500 mAh g^{-1}. When the current density is changed back to 30 mAh g^{-1}, its discharge capacity is 173 mAh g^{-1} which shows little capacity fading in the following cycles and is still as high as 174 mAh g^{-1} at the 50^{th} cycle. The capacity retention rate is 91.4 % after 50 cycles at different current densities (Figure 2-12b). In addition, the coulombic efficiency of HT-Mn-400 is above 97% during the whole testing process except in the initial cycles, indicating that this sample has a superior reversible capacity that contributes to the good cycling stability. For comparison, we also tested the capacity performance of TiO_2 nanosheet-based spheres without any doping or calcination (TiO_2-HT). In Figure 2-12c, its capacity drops from 240 mAh g^{-1} to 153 mAh g^{-1} after the first 10 cycles at the low current density of 30 mA g^{-1}, and the coulombic efficiency is lower than 95%. As the test continues, the capacity has a little fading at different current densities; after 50 cycles, the capacity is 137 mAh g^{-1} and the capacity retention is 57.0%.

All of these electrochemical results indicate that Mn-doped TiO_2 samples have noticeably better Li-ion storage capability than undoped ones when used as an anode at an elevated temperature of 55 °C. Furthermore, the kinetic properties of these samples are also measured by electrochemical impedance spectroscopy (EIS). As

shown in Figure 2-12d, the equivalent circuit (Figure 2-12d inset), R_s and R_{ct} are the ohmic resistance (total resistance of the electrolyte, separator and electrical contacts)

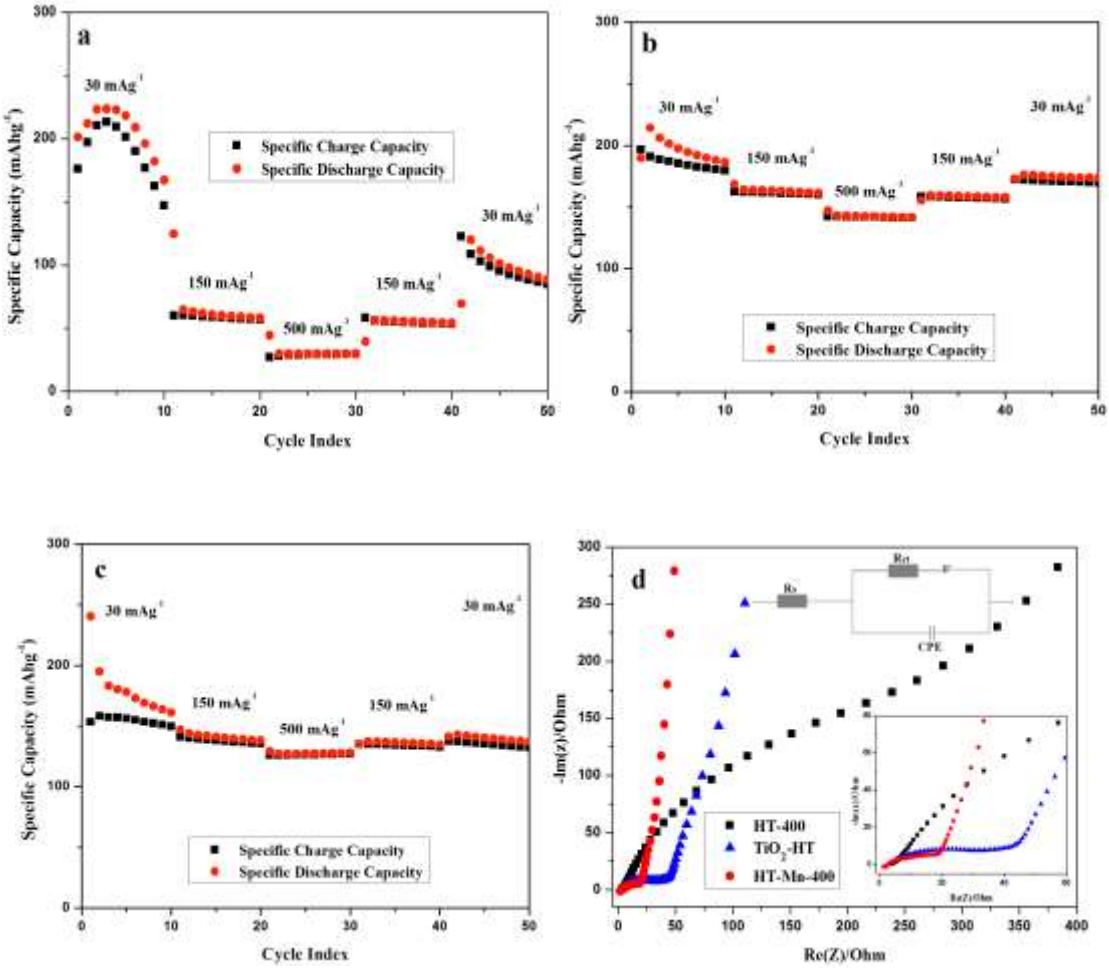

Figure 2-12. Charge/discharge capacity vs. cycle number of a) HT-400, b) HT-Mn-400 and c) TiO_2-HT cycled at different current densities of 30mAg^{-1}, 150 mAg^{-1} and 500mAg^{-1}. (d) Nyquist plots of HT-400, HT-Mn-400 and TiO_2-HT after cycling and the equivalent circuit (the inset shows an expanded view of the high frequency region of the plots).

and charge transfer resistance, respectively, and W represents the Warburg impedance of Li ion diffusion into the active materials. CPE is the constant phase-angle element, involving double layer capacitance. The system resistance of R_s is similar for HT-400, HT-Mn-400 and TiO_2-HT because of the fact that both materials are grown directly on the substrates that are used at the current collectors, which ensures good electrical

conductivity in the electrodes. The charge transfer resistance R_{ct} after cycling for the three samples is in the order of HT-400 (270.6 Ω)> TiO_2-HT (39.7 Ω)> HT-Mn-400(18.6 Ω), which indicates that Mn-ion doping can improve the charge transfer process at the electrode/electrolyte interface and maintain good electronic conductivity during long-term cycling. Thus, these improved interface properties are considered to be a factor in improving the performance of Mn-doped TiO_2. Together with the results from XRD and BET tests (Figures 2-4, 5, and 6), we can deduce the effects of Mn-ion doping in this experiment as follows: during ion-exchange, Mn^{2+} replaced some of the H^+ in the structure of $H_4Ti_2O_6$ to form a multi-structure, which improved the structure stability of flower-like TiO_2 nanosheets[51] i.e. it inhibited the crystal structure conversion under thermal treatment. As a result, the specific surface area and crystal structure of Mn-doped sample HT-Mn-400 had little change after calcination compared to the uncalcined sample TiO_2-HT. Meanwhile, doped Mn ions modified the surface chemistry of TiO_2 nanosheets and maintained their good interface electronic conductivity during long-term cycling. It took a couple of cycles for HT-Mn-400 to build up a more stable interface between the electrode and electrolyte in the electrochemical test. This could explain very well why the discharge curve shape of HT-Mn-400 did not stabilize in the initial discharge/charge cycle (Figure 2-10b). This stable interface contributed to the surface integrity of the Mn-doped TiO_2 electrode at elevated temperatures, as evidenced by the cyclic stability improvement during lithium ion insertion/extraction tests. Its possible roles include reduction of TiO_2 dissolution into the electrolyte and better retention of

nanosheet morphology, which keeps a comparably high electroactive area and thus causes less performance degradation. In addition, during recharge, doped Mn ions may have also made it easier to break some covalent Li-O bonds whose presence is believed to account for a partial loss of charge capacity as reported by Hadjean et al.[52]

3. Conclusion

In summary, a simple and effective strategy is developed based on the hydrothermal method and ion-exchange process to obtain Mn-doped TiO_2 nanosheet-based spheres. Compared to TiO_2 nanosheet-based spheres without doping, the Mn-doped sample exhibits superior reversible capacity, improved cycling stability and rate capability when used as lithium ion battery electrodes. The improved electrochemical performance can be ascribed to the roles of Mn ions in inhibiting crystal structure conversion under calcination and improving the electrode/electrolyte interface stability. All of these effects make Mn ion-exchanged TiO_2 a promising anode for a next generation of LIBs. And the proposed synthesis strategy would also open up new opportunities in the development of high performance nanostructures used in relevant fields.

C. Ni-Doped TiO_2 Derived from Protonated Layered Titanate

1. Experimental procedure

For the synthesis of Ni-doped TiO_2 structures, the precursor of layered protonated dititanate was first prepared *via* an aqueous solution based reaction at room

temperature similar to reported in the literature.[53] In a typical synthesis process, 2.9762 mL of titanium (IV) isopropoxide (TIP, 97%, Sigma-Aldrich) was added to 10 mL of anhydrous ethanol (>99.5%, Anhydrous, Sigma-Aldrich), followed by the addition of 40 mL of ammonium hydroxide (ACS, 30%, Alfa Aesar) under stirring. The milky white suspension was kept static for 10 min and then centrifuged; the precipitate was washed with DI water three times and suspended in 25 mL of ammonium carbonate (ACS, Fisher Chemical) solution (1.5 M). Then, 3 mL of hydrogen peroxide (ACS, 30.0 to 32.0 %, Fisher Chemical) was added to the solution and stirred overnight. The obtained products were washed with DI water three times and dried in air at 50 °C. After this treatment, the obtained precursors were dispersed in 200 mL of nickel chloride (98%, Anhydrous, Alfa Aesar) solution (0.09 M) under constant stirring for 2 h. After that, the powders were washed three times by DI water to remove excess ions and dried in air at 50 °C. For comparison, the precursor powders were also doped with Li and Mn ions in the same concentration of lithium hydroxide and manganese nitrate tetrahydrate (98%, Alfa Aesar) solutions. Finally, the doped and undoped TiO_2 powders were calcined at 400 °C for 3 h. Within this study, the samples are designated as TiO_2-P (precursor), TiO_2-400 (after calcination without ion doping), TiO_2-Ni-400 (after the Ni ion-exchange process and calcination), and TiO_2-Mn-400 (after the Mn ion-exchange process and calcination). The structural characterization and electrochemical measurement are similar as shown in part A.

2. Results and discussion

2.1 Characterization of Ni and Mn-doped TiO_2 structures

As shown in Figure 2-13a, the low-resolution scanning electron microscope (SEM) image shows that the synthesized TiO_2 precursor (TiO_2-P) is granular in nature. Furthermore, the transmission electron microscope (TEM) image in Figure 2-13b reveals that a single particle is formed by layered nanosheets overlapping each other. Figure 2-13c shows a SEM image of the TiO_2 after calcination at 400 °C for 3 h (TiO_2-400). Compared to the sample before calcination, there is little noticeable morphology change. Figure 2-13d shows the SEM image of TiO_2 doped with Ni, and then calcined under the same conditions at 400 °C (TiO_2-Ni-400). As shown in this image, TiO_2-Ni-400 has a similar morphology to TiO_2-400. The Mn ion doped sample TiO_2-Mn-400 also exhibits a similar morphology to TiO_2-400 and TiO_2-Ni-400 (Figure 2-13e). All these images indicate that this ion-exchange process has negligible influence on the morphology of prepared samples. However, obvious differences in crystallinity, surface composition, and surface area can be identified among them through the study of XRD patterns, XPS spectra, and nitrogen adsorption isotherms.

The effect of doped ions on crystallinity evolution of TiO_2 is studied by XRD and the patterns are shown in Figure 2-14. In Figure 2-14a, the XRD pattern of prepared protonated titanate has two diffraction peaks of $2\theta \approx 9.7°$, 27.6° corresponding to the first and second strongest diffraction peaks of $H_4Ti_2O_6$ (PDF, 047-0124, a=1.926, b=0.378, c=0.300). After calcination at 400 °C for 3 h, the undoped sample TiO_2-400 shows a typical anatase crystal structure (Figure 2-14b). The Ni-doped sample TiO_2-Ni-400 shows a similar anatase crystal structure but lower peak intensity, which suggests that nickel ions have inhibition effects on the TiO_2 phase transition.

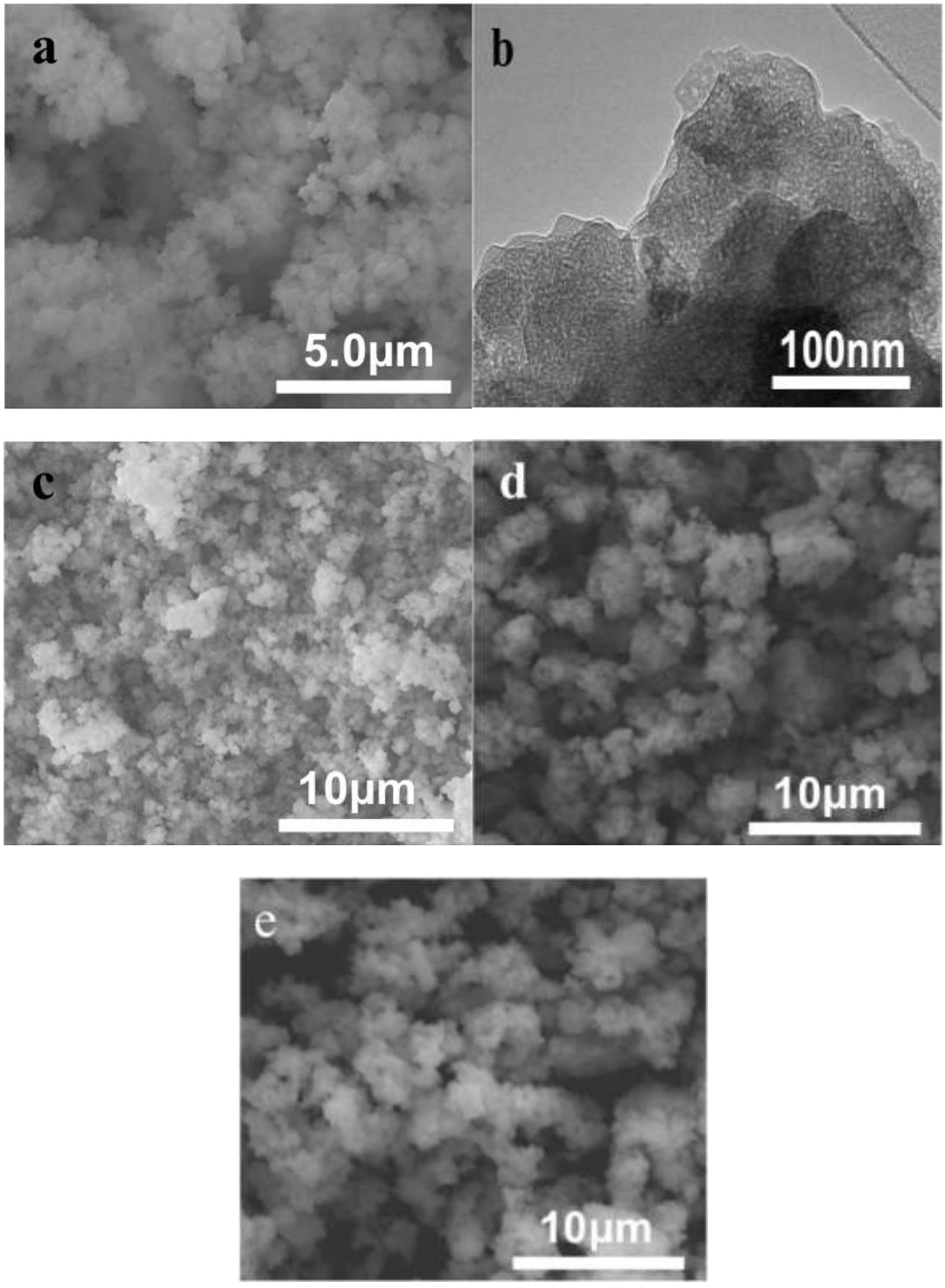

Figure 2-13. Images of TiO_2 structures obtained after different processes: a) SEM image of TiO_2 layered protonated titanate, b) TEM image of TiO_2 layered protonated titanate, c) SEM image of TiO_2 structure calcined at 400 °C for 3 h, d) and e) SEM image of TiO_2 structure doped by nickel, manganese ions, and then calcined at 400 °C for 3 h.

This inhibition effect is more noticeable in the case of manganese ion doping. As shown in the same figure, the Mn-doped sample TiO_2-Mn-400 shows very weak crystalline peaks in its XRD pattern, suggestion various ions have different level of delay for the crystallization temperature of TiO_2. To more clearly identify this result, high temperature XRD patterns of protonated titanate doped with and without Li^+ were recorded from 200 to 700 °C with the interval of 50 °C. As shown in Figure 2-14c, when the temperature increased to 350 °C, Li-doped sample exhibited a tiny diffraction peak around 25.6° corresponding to the first strongest diffraction peak of anatase. However, the similar diffraction peak can be clearly observed in undoped protonated titanate when the temperature is only at 250 °C (Figure 2-14d). Above inhibition effect was also observed in our work in part A. And some other groups also reported a similar result using a traditional calcination doping process.[28,38] However, the exact mechanism of surface ion-doping in inhibition of crystallization is still a subject of further study.

Besides the crystallinity inhibition effect, it is important to note that diffraction peak shift is identified in TiO_2-400 and TiO_2-Ni-400 patterns. The XRD patterns of these two samples fit the tetragonal structure of anatase well (PDF, 01-071-1166). The lattice parameters *a* and *c* for these two samples can be calculated by the software of TOPAS (Bruker, USA). TiO_2-Ni-400 has a larger lattice value of *a* (3.7938±0.0013 Å), and a smaller value of *c* (9.4830±0.0027 Å) than that of undoped sample TiO_2-400 (*a*= 3.7874±0.0007 Å, *c*=9.5021±0.0016 Å). The volume of the unit cell for TiO_2-Ni-400 (136.488 $Å^3$) is larger than TiO_2-400 (136.302 $Å^3$).

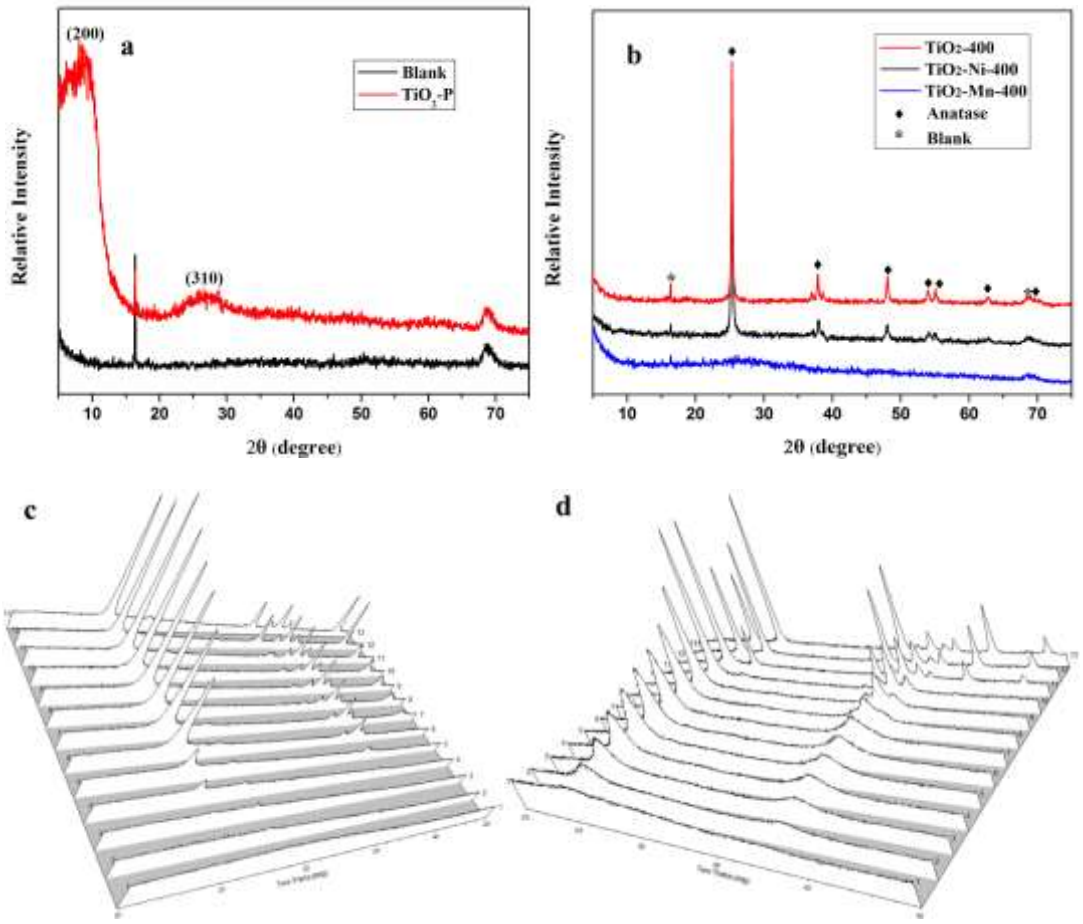

Figure 2-14. XRD patterns of different TiO_2 samples: a) Protonated titanate fabricated at room temperature, the black line represents the blank sample holder, which has diffraction peaks of $2\theta \approx 16^\circ$ and 74° existing in all samples, b) TiO_2-400, TiO_2-Ni-400 and TiO_2-Mn-400, c) and d) HTXRD patterns of protonated titanate doped with c) and without Li^+ d), the measurement were recorded from 200 to 700 °C with the interval of 50 °C.

This result suggests that after Ni doping the *c* axis of the anatase unit cell becomes shorter while the *a* and *b* axes become longer, making the tetragonal structure more cubic and the unit cell volume larger. According to previous studies, these two trends are both favorable for reversible lithium ion insertion.[21,54] In addition, the grain size of TiO_2-Ni-400 (33.4 nm) and TiO_2-400 (67.3 nm) are also different through the

calculation from TOPAS, which will affect their specific surface area after calcination.

To investigate the doping effect of the ion-exchange process, surface element compositions of TiO_2-400, TiO_2-Ni-400 and TiO_2-Mn-400 were studied by XPS. As shown in Figure 2-15, two distinct peaks at binding energies of 855.5 and 873.8 eV are observed in the Ni 2p high-resolution spectrum of TiO_2-Ni-400 (Figure 2-15a), which correspond well to the Ni $2p_{3/2}$ and Ni $2p_{1/2}$ peaks of Ni^{2+}.[55,56] In addition, two small peaks at 861.2 and 879.1 eV can be attributed to $2p_{3/2}$ sat and $2p_{1/2}$ sat of NiO.[56,57] Fig. 3b shows the Mn 2p high-resolution spectrum of TiO_2-Mn-400. There are two distinct peaks at 641.3 and 653.4 eV, which may be assigned to the 2p3/2 and 2p1/2 peaks of Mn^{2+}. And it can be further confirmed through the unique a broad shake-up satellite peak around 645 eV, which is not shared by the other oxidation states of Mn ions.[35,36] This suggests that the doped ions' oxidation state do not change after calcination at 400 °C for 3 h. This data provides direct evidence for the presence of Ni and Mn in TiO_2-Ni-400 and TiO_2-Mn-400. Furthermore, the concentration of Ni and Mn ions can also be obtained *via* high-resolution scans and the application of empirically derived relative sensitivity factors. The atomic ratio of Ni in TiO_2-Ni-400 is approximately 7 % and the atomic ratio of Mn in TiO_2-Mn-400 is approximately 4 %.

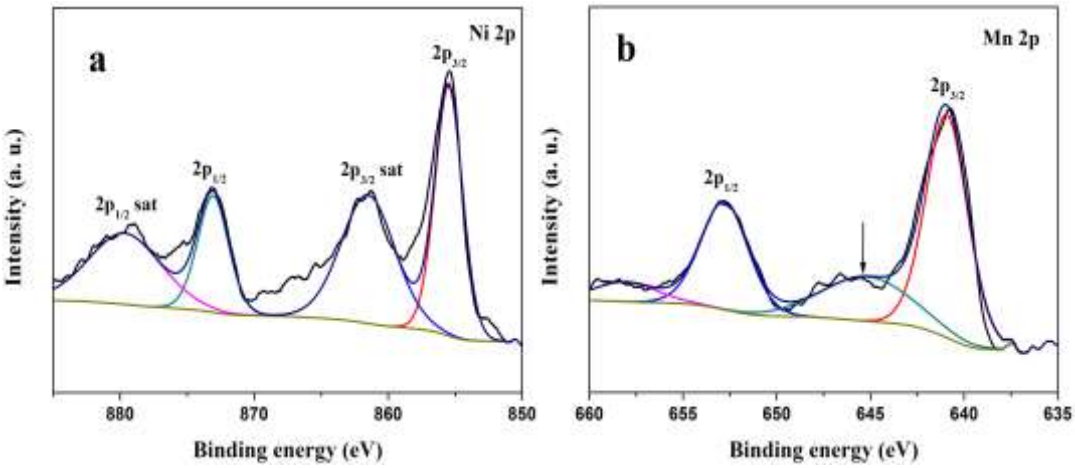

Figure 2-15. XPS spectra of TiO_2 samples: (a) TiO_2-Ni-400 and (b) TiO_2-Mn-400.

Ion doping also affects the specific surface area of TiO_2 after calcination. Here, we studied the surface area of different samples by using nitrogen adsorption-desorption measurements. Figure 2-16 shows the adsorption and desorption isotherm curves of these three samples. TiO_2-Ni-400 and TiO_2-Mn-400 exhibit adsorption hysteresis that belongs to type IV isotherm curves, indicating that these two samples have mesoporous structures.[58] Their specific surface areas are calculated using the BJH method to be 30.4 $m^2 g^{-1}$ and 46.3 $m^2 g^{-1}$, respectively. TiO_2-400 shows type II isotherm curves that suggest little porosity. The specific surface area is only 14.5 $m^2 g^{-1}$. Based on the above results, we can deduce that doped ions act as nucleation barriers to inhibit the crystallization process and phase transition during calcination. As a result, the doped TiO_2 has a less crystallinity than the undoped TiO_2. In addition, the doped ions also have effect on the reducing of TiO_2 grain size, which will finally result in the increasing of the specific surface area.[59,23] As a result, the doped sample has larger specific surface areas and less crystallinity than the undoped sample after calcination. In addition, this effect varies according to the different doped ions. As

shown in Fig. 2-14b and Fig. 2-16, the Mn ions doped TiO_2 (TiO_2-Mn-400) shows a larger surface area and less crystallinity than the Ni doped one (TiO_2-Ni-400).

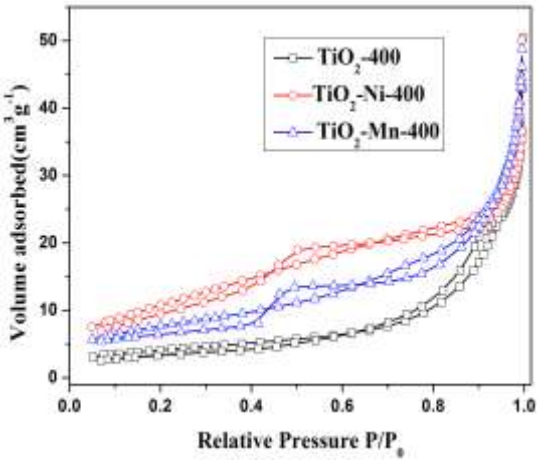

Figure. 2-16 Nitrogen sorption isotherms of TiO_2-400, TiO_2-Ni-400 and TiO_2-Mn-400.

2.2 Electrochemical performance of doped and undoped TiO_2

To study the effects of ion doping on the performance of anatase TiO_2 structures as lithium ion storage electrodes, the lithium-ion insertion/extraction properties of TiO_2 anatase (TiO_2-400) and doped TiO_2 (TiO_2-Ni-400 and TiO_2-Mn-400) were evaluated by galvanostatic discharge/charge tests at room temperature for 50 cycles. Fig. 2-17a-c shows discharge and charge curves of these three samples in the initial and last 3 cycles at a discharge/charge current density of 30 mAg^{-1} in the potential window of 1-2.5 V. It is observed that the initial discharge capacities of TiO_2-400, TiO_2-Ni-400 and TiO_2-Mn-400 are 128 mAh g^{-1}, 448 mAh g^{-1} (this high value was largely due to the parasitic reaction in the first cycle and will not be used for any capacity comparison in later discussions) and 145 mAh g^{-1}, respectively. As shown in Figure 2-17a, TiO_2-400 shows well-defined plateaus at approximately 1.8 V (discharge process) and 1.9 V (charge process) during the initial 3 cycles, which is

similar to reported nanostructured anatase.[16,60] In the last 3 cycles, the lengths of plateaus increased slightly as do the capacities. This result suggests that the as-synthesized anatase TiO_2 without doping can only be used as an anode for batteries that do not require high capacity but emphasize good stability. In contrast, Ni doped TiO_2 clearly exhibits higher capacities. As shown in Figure 2-17b, TiO_2-Ni-400 exhibits a remarkably higher initial discharge capacity of 448 mAh g^{-1}, which is almost four times that of TiO_2-400. This higher than theoretical value consists of irreversible capacity contributed by side reactions during electrode/electrolyte interface formation, which is demonstrated by subsequent capacity degradation from 448 mAh g^{-1} to 271 mAh g^{-1} at the 2nd cycle. After this initial capacity degradation, the nickel-doped sample TiO_2-Ni-400 exhibits relatively stable performance during cycling. It is also noticed that discharge and charge plateaus of TiO_2-Ni-400 are much less well defined as compared to those of TiO_2-400. Different from TiO_2-400 and TiO_2-Ni-400, TiO_2-Mn-400 shows a sloping profile of voltage-capacity relationship during discharge and charge processes (Figure 2-17c). These curves are typical for electrode materials with low crystallinity, which agrees well with the XRD finding. In addition, although the discharge capacity of TiO_2-Mn-400 in the 1st is a little higher than TiO_2-400, its capacity exhibits noticeable degradation in the subsequent cycles. Figure 2-17d displays the cyclic performance of these three samples at different current densities of 30 mA g^{-1}, 150 mA g^{-1} and 500 mA g^{-1}. As shown in this figure, TiO_2-400 exhibits a good cycling stability. The discharge capacity of TiO_2-400 shows a little increase from 128 mAh g^{-1} to 132 mAh g^{-1} after 50 cycles. However, its rate

performance is very poor, the discharge capacity is 88 mAh $g^{-1}$and 58 mAh g^{-1} under the current density of 150 mA g^{-1} and 500 mA g^{-1}, respectively. In contrast, TiO_2-Ni-400 starts with a remarkably high discharge capacity of 448 mAh g^{-1} followed by a noticeable decay in the 2nd cycle. After this degradation, capacity loss still exists in initial cycles but is much smaller. After 10 cycles, the discharge capacity is 230 mAh g^{-1}, which is more than twice that of TiO_2-400. In addition, the rate capability of TiO_2-Ni-400 is also obviously better than TiO_2-400: its discharge capacity is 200 mAh g^{-1} at a current density of 150 mA g^{-1} and 179 mAh g^{-1} at a current density of 500 mA g^{-1}. When the current density is changed back to 30 mA g^{-1}, its discharge capacity is 221 mAh g^{-1}, which fluctuates slightly in the following cycles and is as high as 226 mAh g^{-1} after 50 cycles. This value is obviously higher than doped TiO_2 samples reported by other papers. For instance, Djerdj et al. reported a mesoporous Nb-doped TiO_2 synthesized *via* a sol-gel process. The capacity was 168.4 $mAhg^{-1}$ at a rate of C/8 after 10 cycles.[61] Huang et al. synthesized a conformal N-doped carbon on nanoporous TiO_2 by a solution-phase process. The product exhibited a capacity of 170 mAh g^{-1} at a current density of 100 mA g^{-1} and 102 mAh g^{-1} at a current density of 200 mA g^{-1}.[62] Figure 2-17d also shows that TiO_2-Mn-400 possesses even lower performance than TiO_2-400. It has a lower capacity of 91 mAh g^{-1} after 50 cycles. And for higher current densities of 150 mA g^{-1} and 500 mA g^{-1}, the discharge capacity is only 60 mAh $g^{-1}$and 36 mAh g^{-1}, respectively. The contrasting performance of TiO_2-Mn-400 and TiO_2-Ni-400 indicates that only certain ion doping can enhance TiO_2's performance as a lithium ion insertion electrode. These different

ion doping effects on the electrode peroformance are also in agreement with the result reported by Jiao's group.[48]

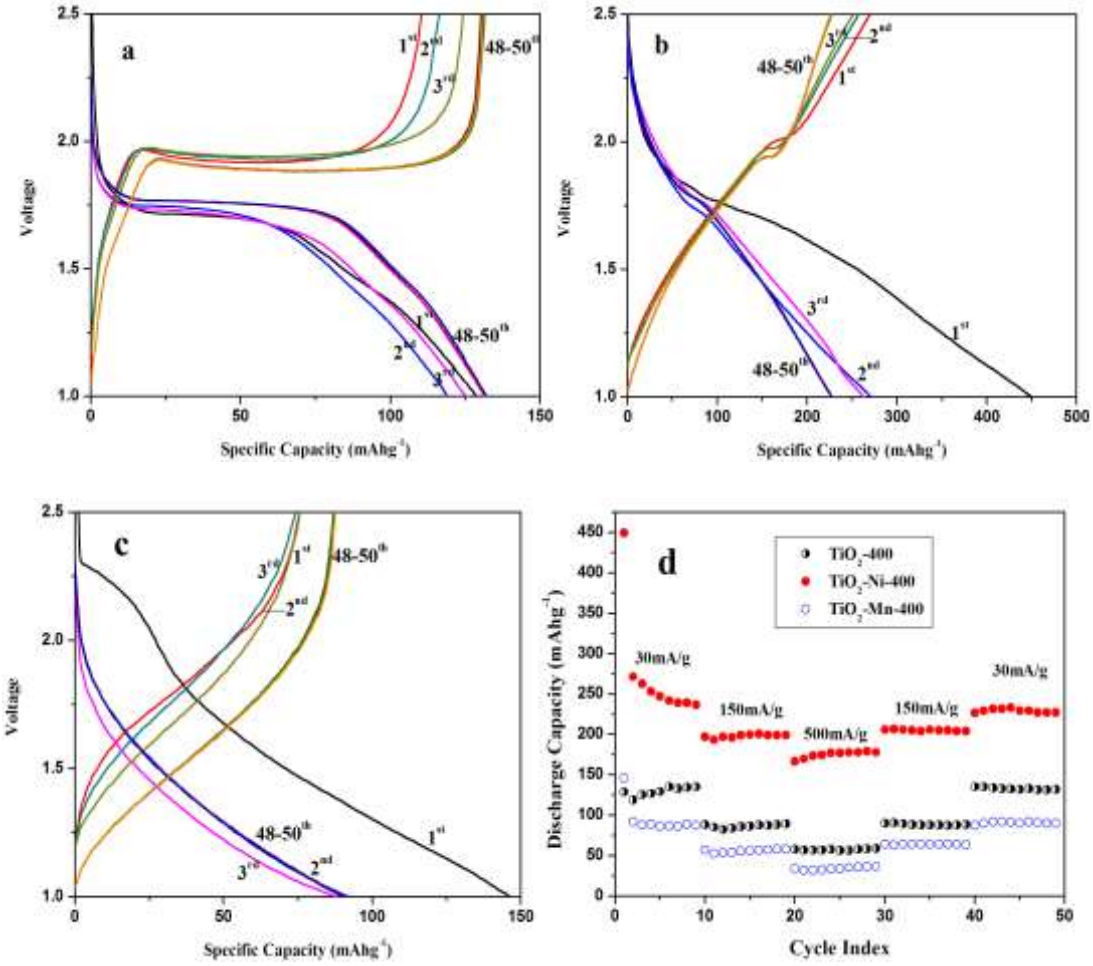

Figure 2-17. Galvanostatic discharge (lithium insertion)/charge (lithium extraction) curves vs. Li^+/Li of TiO_2-400, TiO_2-Ni-400 and TiO_2-Mn-400 cycled at a current of 30 mAg-1 in the initial and last 3 cycles of a 50-cycle test (a-c), (d) Rate performances of all these three samples, measured at various rates with a voltage window between 1.0 and 2.5 V.

Above results are also supported by the analysis of the kinetic properties of these samples. Here, electrochemical impedance spectroscopy (EIS) was used to test the charge transfer resistance (R_{ct}) before and after electrochemical cyclic tests. Figure 2-18a shows the equivalent circuit: R_s, R_f and R_{ct} are ohmic resistance (total resistance

of the electrolyte, separator and electrical contacts), film resistance, and charge transfer resistance, respectively, and Z_w represents the Warburg impedance of Li ion diffusion into active materials. CPE is the constant phase-angle element, involving double layer capacitance.

The system resistance of R_s is similar for TiO_2-400, TiO_2-Ni-400 and TiO_2-Mn-400 because of the fact that all the materials are coated directly on copper substrates that are used as current collectors, which ensures good electrical conductivity in the electrodes. Before the cycling, the total resistance of R_f and R_{ct} for three samples are in the order of TiO_2-Ni-400 (110 Ω)> TiO_2-Mn-400 (89 Ω)> TiO_2-400 (80 Ω) (Figure 2-18b). After cycling, the film resistance of R_f is similar for these three samples, the charge transfer resistance R_{ct} is in the order of TiO_2-Mn-400 (57 Ω)> TiO_2-400 (41 Ω)> TiO_2-Ni-400 (29 Ω) (Figure 2-18c), respectively. Before cycling, both doped samples exhibit higher resistance than the undoped one, which can be ascribed to the formation of a more complicated electrode/electrolyte interface induced by ion doping. After electrochemical cycling, TiO_2-Ni-400 shows the lowest R_{ct}, which explains its high discharge capacity and good rate capability. To the opposite, TiO_2-Mn-400's charge transfer resistance R_{ct} is much higher than that of TiO_2-Ni-400's after electrochemical tests. This explains well the different performance of Ni and Mn doped samples. Furthermore, all these three samples exhibit impedance reduction after cycling, which can be ascribe to the electrode activated before and after cycling, and also due to the effects of doped ions on the

electronic conductivity of the whole electrode. The similar impedance reduction has been reported before.[63]

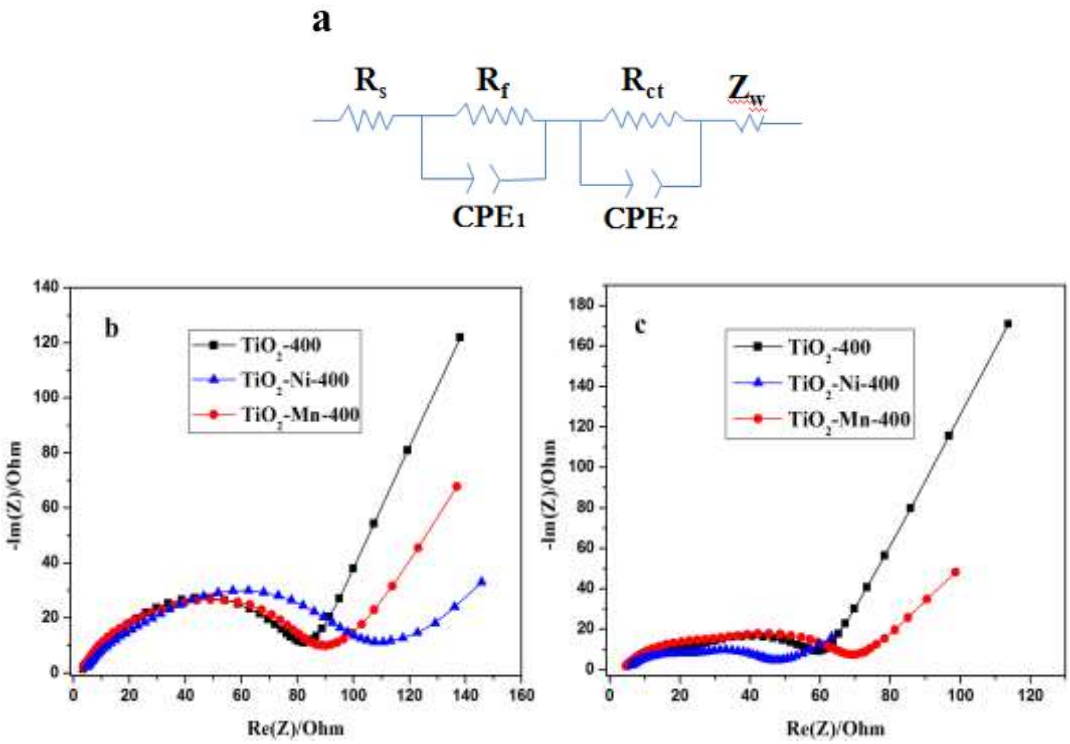

Figure 2-18. The equivalent circuit of EIS (a), Nyquist plots of TiO_2-400, TiO_2-Ni-400, and TiO_2-Mn-400 before (b) and after cycling (c).

Based on above results, we can summarize the effects of nickel ion doping on TiO_2 as follows: during ion-exchange, Ni^{2+} ions replaced the removable H^+ in the protonated titanate, which would form a multi-structured TiO_2. During calcination, the existence of Ni^{2+} ions induced an unit cell volume increase of the crystal structure and also casued lattice distortion, which would partially inhibit the growth of crystalline phase and reduce the grain size of TiO_2. As a result, more lithium ions could be inserted into Ni-TiO_2, justifying the high capacity during cycling. At the same time, Ni ions contributed to the formation of a more favorable electrode/electrolyte interface during cycing, as demonstrated in the EIS study. This

interface facilitated the charge transfer process during lithium ion insertion and its existence explained why TiO_2-Ni-400 possessed a better rate capability than other samples.

3. Conclusion

In summary, an effective doping strategy was developed based on the ion-exchange process to obtain Ni-doped TiO_2 structures at room temperature. Compared to the undoped anatase TiO_2, Ni ion doping improved the electrochemical performance of as-prepared TiO_2 notably when used as lithium ion battery electrodes. This enhancement can be ascribed to the effect of doped Ni ions on the TiO_2 structure, including the inhibition of crystallinity under calcination, by causing lattice distortion. In addition, the introduction of Ni ions onto the surface of TiO_2 structure contributed to the formation of a favorable electrode/electrolyte interface that reduced the charge transfer resistance significantly during repeated lithium ion insertion. All of these effects were achieved by a simple surface doping process. And the product can be easily scaled up at room temperature. This proposed synthesis strategy would provide a novel and feasible doping method in the development of high performance materials used in lithium ion batteries and relevant fields.

References

[1] N.-S. Choi, Z.H. Chen, S.A. Freunberger, X.L. Ji, Y.K. Sun, K. Amine, G, Yushin, L.F. Nazar, J. Cho, and P.G. Bruce, “Challenges Facing Lithium Batteries and Electrical Double-Layer Capacitors,” *Angew. Chem. Int. Ed.*, **51** 9994-10024 (2012).

[2] Y.S. Hu, Y.G. Guo, W. Sigle, S. Hore, P. Balaya, and J. Maier, "Electrochemical Lithiation Synthesis of Nanoporous Materials with Superior Catalytic and Capacitive Activity," *Nat. Mater.*, **5** 713 (2006).

[3] S.R.S. Prabaharan, M.S. Michael, S. Radhakrishna, and C. Julien, "Novel Low-Temperature Synthesis and Characterization of $LiNiVO_4$ for High-Voltage Li Ion Batteries," *J. Mater. Chem.*, **7** 1791-1796 (1997).

[4] D.D. MacNeil, and J.R. Dahn, "The Reactions of $Li_{0.5}CoO_2$ with Nonaqueous Solvents at Elevated Temperatures," *J. Electrochem. Soc.*, **149** A912-A919 (2002).

[5] I. Saadoune, and C. Delmas, "$LiNi_{1-y}Co_yO_2$ Positive Electrode Materials: Relationships Between the Structure, Physical Properties and Electrochemical Behavior," *J. Mater. Chem.*, **6** 193-199 (1996).

[6] J.B. Goodenough, H.D. Abruña, and M.V. Buchanan, *Basic Research Needs for Electric Energy Storage: Report of the Basic Energy Sciences Workshop on Electrical Energy Storage*. U.S. Department of Energy, Office of Basic Energy Sciences, Washington, DC, 2007.

[7] M.R. Palacín, "Recent Advances in Rechargeable Battery Materials: A Chemist's Perspective," *Chem. Soc. Rev.*, **38** 2565-2575 (2009).

[8] P.G. Bruce, S.A. Freunberger, L.J. Hardwick, and J.M. Tarascon, "Li-O_2 and Li-S Batteries with High Energy Storage," *Nat. Mater.*, **11** 19-29 (2012).

[9] M. Armand, and J.M. Tarascon, "Building Better Batteries," *Nature*, **451** 652-657 (2008).

[10] A.M. Andersson, and K. Edström, "Chemical Composition and Morphology of the Elevated Temperature SEI on Graphite," *J. Electrochem. Soc.*, **148** A1100-A1109 (2001).

[11] A.M. Andersson, K. Edström, J.O. Thomas, "Characterization of the Ambient and Elevated Temperature Performance of a Graphite Electrode," *J. Power Sources*, **81** 8-12 (1999).

[12] S.T. Myung, N. Takahashi, S. Komaba, C.S. Yoon, Y.K. Sun, K. Amine, and H. Yashiro, "Nanostructured TiO_2 and Its Application in Lithium-Ion Storage," *Adv. Funct. Mater.*, **21** 3231-3241 (2011).

[13] H. Han, T. Song, J.Y. Bae, L.F. Nazar, H. Kim, and U. Paik, "Nitridated TiO_2 Hollow Nanofibers as an Anode Material for High Power Lithium Ion Batteries," *Energy Environ. Sci.*, **4** 4532-4536 (2011).

[14] G. Armstrong, A.R. Armstrong, P.G. Bruce, P. Reale, and B. Scrosati, "TiO_2(B) Nanowires as an Improved Anode Material for Lithium-Ion Batteries Containing $LiFePO_4$ or $LiNi_{0.5}Mn_{1.5}O_4$ Cathodes and a Polymer Electrolyte," *Adv. Mater.*, **18** 2597-2600 (2006).

[15] T. Fröschl, U. Hörmann, P. Kubiak, G. Kučerová, M. Pfanzelt, C.K. Weiss, R. Behm, N. Hüsing, U. Kaiser, and K. Landfester, "High Surface Area Crystalline Titanium Dioxide: Potential and Limits in Electrochemical Energy Storage and Catalysis, " *Chem. Soc. Review,* **41** [15] 5313-5360 (2012).

[16] J.-Y. Shin, D. Samuelis, and J. Maier, "Sustained Lithium-Storage Performance of Hierarchical Nanoporous Anatase TiO_2 at High Rates: Emphasis on Interfacial Storage Phenomena," *Adv. Funct. Mater.*, **21** 3464-3472 (2011).

[17] S.Y. Huang, L. Kavan, I. Exnar, and M. Grätzel, "Rocking Chair Lithium Battery Based on Nanocrystalline TiO_2 (Anatase)," *J. Electrochem. Soc.*, **142** L142-L144 (1995).

[18] V. Subramanian, A. Karki, K.I. Gnanasekar, F.P. Eddy, and B. Rambabu, "Nanocrystalline TiO_2 (Anatase) for Li-Ion Batteries," *J. Power Sources,* **159** 186-192 (2006).

[19] L. Kavan, "Lithium Insertion Into TiO_2 (anatase): Electrochemistry, Raman Spectroscopy, and Isotope labeling," *J. Solid State Electrochem.,* **18** 2297 (2014).

[20] L. Kavan, M. Graetzel, J. Rathousky, and A. Zukal, "Nanocrystalline TiO_2 (Anatase) Electrodes: Surface Morphology, Adsorption, and Electrochemical Properties," *J. Electrochem. Soc.*, **143** 394-400 (1996).

[21] A.A. Belak, Y. Wang, and A. van der Ven, "Kinetics of Anatase Electrodes: The Role of Ordering, Anisotropy, and Shape Memory Effects," *Chem. Mater.*, **24** 2894 (2012).

[22] S. Yang, X. Feng, and K. Muellen, "Sandwich-Like, Graphene-Based Titania Nanosheets with High Surface Area for Fast Lithium Storage," *Adv. Mater.*, **23** 3575-3579 (2011).

[23] I. Moriguchi, R. Hidaka, H. Yamada, T. Kudo, H. Murakami, and N. Nakashima, "A Mesoporous Nanocomposite of TiO_2 and Carbon Nanotubes as a High-Rate Li-Intercalation Electrode Material," *Adv. Mater*., **18** 69-73 (2006).

[24] H. Han, T. Song, E.K. Lee, A. Devadoss, Y. Jeon, J. Ha, Y.C. Chung, Y.M. Choi, Y.G. Jung, and U. Paik, "Dominant Factors Governing the Rate Capability of a TiO_2 Nanotube Anode for High Power Lithium Ion Batteries," *ACS Nano*, **6** 8308-8315 (2012).

[25] J. Liu, J.S. Chen, X. Wei, X.W. Lou, and X.W. Liu, "Sandwich-Like, Stacked Ultrathin Titanate Nanosheets for Ultrafast Lithium Storage," *Adv. Mater.*, **23** 998-1002 (2011).

[26] J. Ye, W. Liu, J. Cai, S. Chen, X. Zhao, H. Zhou, and L. Qi, "Nanoporous Anatase TiO_2 Mesocrystals: Additive-Free Synthesis, Remarkable Crystalline-Phase Stability, and Improved Lithium Insertion Behavior," *J. Am. Chem. Soc.*, **133** 933-940 (2011).

[27] P.G. Bruce, B. Scrosati, and J.M Tarascon, "Nanomaterials for Rechargeable Lithium Batteries," *Angew. Chem. Int. Ed.*, **47** 2930-2946 (2008).

[28] J.W. Zhang, J.W. Zhang, Z.S. Jin, Z.S. Wu, and Z.J. Zhang, "Electrochemical Lithium Storage Capacity of Nickel Mono-oxide Loaded Anatase Titanium Dioxide Nanotubes," *Ionics*, **18** 861-866 (2012).

[29] M. Mancini, P. Kubiak, J. Geserick, R. Marassi, N. Huesing, and M. Wohlfahrt-Mehrens, "Mesoporous Anatase TiO_2 Composite Electrodes: Electrochemical Characterization and High Rate Performances," *J. Power Sources*, **189** 585-589 (2009).

[30] X.C. Xiao, P. Lu, and D. Ahn, "Ultrathin Multifunctional Oxide Coatings for Lithium Ion Batteries," *Adv. Mater.*, **23** 3911-3915 (2011).

[31] D.H. Chen, L. Cao, F.Z. Huang, P. Imperia, Y.B. Cheng, and R.A. Caruso, "Synthesis of Monodisperse Mesoporous Titania Beads with Controllable Diameter, High Surface Areas, and Variable Pore Diameters (14-23 nm)," *J. Am. Chem. Soc.*, **132** 4438-4444 (2010).

[32] P. Szirmai, E. Horváth, B. Náfrádi, Z. Mickovic, R. Smajda, D.M. Djokic, K. Schenk, L. Forró, and A. Magrez, "Synthesis of Homogeneous Manganese-Doped Titanium Oxide Nanotubes from Titanate Precursors," *J. Phys. Chem. C*, **117** 697-702 (2013).

[33] S. Södergren, H. Siegbahn, H. Rensmo, H. Lindström, A. Hagfeldt, and S.E. Lindquist, "Lithium Intercalation in Nanoporous Anatase TiO_2 Studied with XPS," *J. Phys. Chem. C*, **101** 3087-3090 (1997).

[34] M.A. Langell, C.W. Hutchings, G.A. Carson, and M.N. Nassir, "High Resolution Electron Loss Spectroscopy of MnO(100) and Oxidized MnO(100)," *J. Vac. Sci. Technol. A*, **14** 1656-1661 (1996).

[35] H.W. Nesbitt, and D. Banerjee, "Interpretation of XPS Mn(2p) Spectra of Mn Oxyhyroxides and Constraints on the Mechanism of MnO_2 precipitation," *Am. Mineral.*, **83** 305-315 (1998).

[36] S. Lowell, J.E. Shields, M.A. Thomas, and M. Thommes, *Characterization of Porous Solids and Powders: Surface Area, Pore Size and Density*. Kluwer: London, 2004.

[37] J.X. Guo, D.D. Wu, L. Zhang, M.C. Gong, M. Zhao, and Y.Q. Chen, "Preparation of Nanometric CeO_2-ZrO_2-Nd_2O_3 Solid Solution and Its Catalytic Performances," *J. Alloy. Compd*., **460** 485-490 (2008).

[38] O. Vázquez-Cuchillo, A. Cruz-López, L.M. Bautista-Carrillo, A. Bautista-Hernández, L.M. Torres Martínez, and S.W. Lee, "Synthesis of TiO_2 Using Different Hydrolysis Catalysts and Doped with Zn for Efficient Degradation of Aqueous Phase Pollutants under UV Light," *Res. Chem. Intermed.*, **36** 103-113 (2010).

[39] G. Xi, K. Xiong, Q. Zhao, R. Zhang, H. Zhang, and Y. Qian, "Nucleation-Dissolution-Recrystallization: A New Growth Mechanism for *t*-Selenium Nanotubes," *Crystal Growth and Design*, **6** 577-582 (2006).

[40] N. Sutradhar, S.K. Pahari, M. Jayachandran, A.M. Stephan, J.R. Nair, B. Subramanian, H.C. Bajaj, H.M. Mody, and A.B. Panda, "Organic Free Low Temperature Direct Synthesis of Hierarchical Protonated Layered Titanates/Anatase TiO_2 Hollow Spheres and their Task-Specific Applications," *J. Mater. Chem. A*, **1** 9122-9131 (2013).

[41] Y.G. Tao, Y.Q. Xu, J. Pan, H. Gu, C.Y. Qin, and P. Zhou, "Glycine Assisted Synthesis of Flower-Like TiO_2 Hierarchical Spheres and Its Application in Photocatalysis," *Mater. Sci. Eng. B*, **177** 1664-1671 (2012)**.**

[42] L.S. Zhang, W.Z. Wang, Z.G. Chen, L. Zhou, H.L. Xu, and W. Zhu, "Fabrication of Flower-Like Bi_2WO_6 Superstructures as High Performance Visible-Light Driven Photocatalysts," *J. Mater. Chem*., **17** 2526-2532 (2007).

[43] B. Liu, J.E. Boercker, and E.S. Aydil, "Oriented Single Crystalline Titanium Dioxide Nanowires**,"** *Nanotechnology***, 19** 505604 (2008).

[44] S.W. Pradhan, Y. Mao, S.S. Wong, P. Chupas, and V. Petkov, "Atomic-Scale Structure of Nanosize Titania and Titanate: Particles, Wires and Tubes," *Chem. Mater.*, **19** 6180-6186 (2007).

[45] M.D. Ye, C. Chen, M.Q. Lv, D.J. Zheng, W.X. Guo, and C.J. Lin, "Facile and Effective Synthesis of Hierarchical TiO_2 Spheres for Efficient Dye-Sensitized Solar Cells," *Nanoscale*, **5** 6577-6583 (2013).

[46] H. Zhang, D. Yang, D.S. Li, X.Y. Ma, S.Z. Li, and D.L. Que, "Controllable Growth of ZnO Microcrystals by a Capping-Molecule-Assisted Hydrothermal Process," *Crystal Growth and Design*, **5** 547-550 (2005).

[47] S.J. Dong, and F.B. Li, "Researches on Chemically Modified Electrodes: Part XV. Preparation and Electrochromism of the Vanadium Hexacyanoferrate Film Modified Electrode**,"** *J. Electroanal. Chem.*, **210** 31-44 (1986).

[48] G.S. Hutching, Q. Lu, and F. Jiao, "Synthesis and Electrochemistry of Nanocrystalline M-TiO_2 (M = Mn, Fe, Co, Ni, Cu) Anatase," *J. Electrochem. Soc.*, **160** A511-A515 (2013).

[49] J.Y. Shins, D. Samuelis, and J. Maier, "Sustained Lithium-Storage Performance of Hierarchical, Nanoporous Anatase TiO_2 at High Rates: Emphasis on Interfacial Storage Phenomena," *Adv. Funct. Mater.*, **21** 3464-3472. (2011)**.**

[50] D.W. Liu, Y.Y. Liu, B.B. Garcia, Q.F. Zhang, A.Q. Pan, Y.H. Jeong, and G. Z. Cao, "V_2O_5 Xerogel Electrodes with Much Enhanced Lithium-Ion Intercalation Properties with N_2 Annealing," *J. Mater. Chem.*, **19** 8789-8795 (2009).

[51] D.M. Yu, S.T. Zhang, D.W. Liu, X.Y. Zhou, S. H. Xie, Q.F. Zhang, Y.Y. Liu, and G.Z. Cao, "Effect of Manganese Doping on Li-ion Intercalation Properties of V_2O_5 Films," *J. Mater. Chem.*, **20** 10841-10846 (2010).

[52] R. Baddour-Hadjean, and J.P. Pereira-Ramos, "New Structural Approach of Lithium Intercalation Using Raman Spectroscopy," *J. Power Sources*, **174** 1188-1192 (2007).

[53] N. Sutradhar, A. Sinhamahapatra, S.K. Pahari, H.C. Bajaj, and A.B. Panda, "Room Temperature Synthesis of Protonated Layered Titanate Sheets Using Peroxo Titanium Carbonate Complex Solution," *Chem. Commun.*, **47** [27] 7731 (2011).

[54] M. Yoshio, H. Noguchi, J.-I. Itoh, M. Okada, and T. Mouri, "Preparation and Properties of $LiCo_yMn_xNi_{1-x-y}O_2$ as a Cathode for Lithium Ion Batteries," *J. Power Sources*, **90** 176-181 (2000).

[55] G. Ertl, R. Hierl, H. Knozinger, N. Thiele, and H.P. Urbach, "XPS Study of Copper Aluminate Catalysts," *Appl. Surf. Sci.*, **5** 49 (1980).

[56] A.N. Mansour, "Characterization of NiO by XPS," *Surf. Sci. Spectra*, **3** 231 (1994).

[57] K.K. Lian, D.W. Kirk, and S.J. Thorpe, "Investigation of a 'Two-State' Tafel Phenomenon for the Oxygen Evolution Reaction on an Amorphous Ni-Co Alloy," *J. Electrochem. Soc.*, **142** 3704 (1995).

[58] B.J. Tan, K.J. Klabunde, and P.M.A. Sherwood, "XPS Studies of Solvated Metal Atom Dispersed (SMAD) Catalysts. Evidence for Layered Cobalt-Manganese Particles on Alumina and Silica," *J. Am. Chem. Soc.*, **113** 855 (1991).

[59] K.H. Wu, E.G. Wang, Z.X. Cao, Z.L. Wang, and X. Jiang, "Microstructure and Its Effect on Field Electron Emission of Grain-Size-Controlled Nanocrystalline Diamond Films," *J. Appl. Phys.*, **88** 2967 (2000).

[60] N.S. Chen, X.J. Yang, E.S. Liu, and J.L. Huang, "Reducing Gas-Sensing Properties of Ferrite Compounds MFe_2O_4 (M=Cu, Zn, Cd and Mg)," *Sensors and Actuators B*, **66** 178-180 (2000).

[61] Y. Wang, B.M. Smarsly, and I. Djerdj, "Niobium Doped TiO_2 with Mesoporosity and Its Application for Lithium Insertion," *Chem. Mater.*, **22** 6624-6631 (2010).

[62] Y. Qiao, X.L. Hu, Y. Liu, C.J. Chen, H.H. Xu, D.F. Hou, P. Hu, and Y.H. Huang, "Conformal N-doped Carbon on Nanoporous TiO_2 Spheres as a High-Performance Anode Material for Lithium-Ion Batteries," *J. Mater. Chem. A*, **1** 10375-10381 (2013).

[63] J. Xiao, X.J. Wang, X.Q. Yang, S.D. Xun, G. Liu, P.K. Koech, J. Liu, and J.P. Lemmon, "Electrochemically Induced High Capacity Displacement Reaction of PEO/MoS_2/Graphene Nanocomposites with Lithium," *Adv. Funct. Mater.*, **21** 2840-2846 (2011).

Effect of Calcination Atmosphere on Electrodes: Macro-/Mesoporous TiO_2 Anode as an Example

A. Introduction

Hybrid electric vehicles and renewable energy devices are with enormous potentials for low-emission and they have been the impetus for the research and development of high performance lithium ion batteries,[1-3] wherein increasing the performance of such batteries at elevated temperatures (typically up to 55-70 ºC) is of ultimate relevance to their safe use. Normally, elevated temperatures can accelerate the degradation of battery materials, causing capacity degradation and premature cell death. Furthermore, raising the temperature can also provoke the onset of thermal runaway, where the cell temperature increases uncontrollably as a result of some exothermic side reactions.[4] Therefore, the thermal stability of electrode materials is critical for practical battery applications. Unfortunately, the conventional lithium-ion intercalation anode, graphite, faces the challenge of severe decomposition of the solid electrolyte interphase (SEI) on lithiated graphite at elevated temperatures, i.e. above 50 ºC.[5] Irreversible reactions can begin below 60 ºC at the surface of graphite, which will badly diminish its performance, causing lower capacity, poorer cycling stability, etc. Therefore, materials with higher thermal stability are needed to replace graphite as lithium ion battery anode at elevated temperatures. Titanium dioxide (TiO_2) is one valuable candidate material for investigation because of its high chemical stability, low price, abundance, and nontoxicity.[6,7] However, low intrinsic electrical

conductivity has impeded its application in practice.[8,9] To solve this problem, nanostructuring is often implemented and it has been proved to be effective in improving the electrochemical performance of TiO_2 at room temperature *via* shortening Li-ion and electron diffusion paths, enlarging the electrode/electrolyte interfacial area, and facilitating strain relaxation during the insertion/extraction processes.[10-13] However, the complicated fabrication process and relatively low yields are major problems to restrain this method from practical applications. In addition, the large specific surface area of nanostructured TiO_2 can induce faster performance degradation at elevated temperatures. To date, it is still a challenge to devise nanostructured TiO_2 with stable performance at elevated temperatures.

The most widely adopted strategy of improving the stability of nanostructured electrodes is surface modification. There are various surface modification approaches that have been reported for enhancing materials' cyclic performance, such as solvothermal deposition,[14] doping,[15] and atomic layer deposition.[16] These methods normally introduce extra elements to improve the performance of native electrode materials. A few papers reported an alternative strategy of introducing frozen native defects (e.g., frozen oxygen nonstoichiometry in oxides) to the crystal structure of the electrode material.[17-19] Compared to the former approaches, the strategy of introducing surface defects is a simple and useful way to improve the material's lithium ion intercalation performance by avoiding side reactions. The presence of defects at the electrode/electrolyte interface could possibly facilitate the phase transition experienced during lithium ion reactions due to modified surface

thermodynamics. In addition, the electrode layer consisting of defects at the electrode/ electrolyte interface could well preserve the integrity of the electrode surface morphology, improving the cyclic stability of intercalation electrodes.[19]

Based on the above statement, in this chapter, we fabricated a macro-/mesoporous TiO_2 nanostructure of a high specific area (473 m^2 g^{-1}) by a facile and large-scale method at room temperature[20] and used the nitrogen-treated macro-/mesoporous TiO_2 as electrode materials for lithium-ion batteries at an elevated temperature of 55 ºC. This nitrogen-treated TiO_2 exhibited noticeable improvement in lithium ion intercalation capability compared to air-treated sample and can be considered as a very promising anode material for a new generation of lithium-ion batteries working at elevated temperatures.

B. Experimental Procedure

1. Materials synthesis

For the synthesis of nitrogen-treated macro-/mesoporous TiO_2 nanostructures, the precursor of macro-/mesoporous TiO_2 was first prepared *via* a hydrolysis reaction at room temperature according to a modified approach as reported by Yu's group.[20] In a typical synthesis process, 2 mL of titanium (IV) isopropoxide (TIP, 97%, Sigma-Aldrich) was added dropwise to 40 mL water without any surfactant and stirring. The white suspension was kept static and aging for 6 h. Then, the precipitates were removed and washed with DI water three times. Then, the obtained products were dried in air at 40 °C. After this treatment, the obtained precursors were calcined

at 300 °C for 3 h under nitrogen and air atmosphere, respectively. Within this study, the samples are designated as TiO_2 (precursor), TiO_2-N (calcination under nitrogen atmosphere), and TiO_2-A (calcination under air atmosphere).

2. Structural characterization

The morphology of the obtained samples were studied by scanning electron microscopy (SEM, FEI Quanta 200) with the accelerating voltage at 20 kV. The crystal structures were determined by X-ray diffraction (XRD, Bruker D2) on a Scintag diffractometer with $CuK\alpha_1$ radiation (λ= 1.54060 Å) at a scanning rate of 0.03 $°s^{-1}$ in the 2θ range from 5° to 75°. The surface chemistry was measured by X-ray photoelectron spectroscopy (XPS, PHI Quantera) with Al Kα X-rays (monochromatic, beam size=100 μm) at an output power of 25.5 W, with an electron energy of 1486.6 eV and a step size of ~0.025 eV. The optical absorption spectra of the samples were recorded with an UV−visible spectrophotometer (PerkinElmer Lambda 950). The wavelength range and step size used was 200–600 nm and 1 nm, respectively. The nitrogen adsorption and desorption isotherms were collected at 77 K in the range of relative pressures of 0.0002-0.99P/P_0 using a TriStar II 3020 surface area and porosity measurement system (Micromeritics Instrument Corp.) and used for estimation of the pore size distribution in the 1.7-300 nm range.

3. Electrochemical evaluation

Electrochemical impedance spectroscopy (EIS) study was carried out using CHI650E electrochemical workstation. The frequency range was from 100 kHz to 0.1

Hz. Lithium ion battery performance tests were carried out with a half-cell configuration using CR-2032 coin cells. Li foil was used as both the counter and reference electrode. The working electrode was prepared by mixing active materials (80%), carbon black (Alfa Aesar, 10%), and polyvinylidene fluoride (PVDF, Alfa Aesar, 10%) in N-methyl-2-pyrrolidone (NMP, Alfa Aesar). After uniform stirring, the above slurries were coated on copper foils and dried at 120 °C in vacuum for 6 h. Then, the electrode was pressed and cut into disks before assembly in an Argon-filled glove box for coin-cell assembling (MSK-110, MTI). 1 M $LiPF_6$ in a mixed solution of ethylene carbonate and diethyl carbonate (1:2 volume ratio, Novolyte, USA) was used as the electrolyte. Galvanostatical discharge/charge tests were performed using an Arbin-BT 2000 measurement system in the potential window of 1-2.5 V versus Li^+/Li at different current densities of 30 mA g^{-1}, 150 mA g^{-1} and 500 mA g^{-1} at both room temperature and 55 °C.

C. Results and Discussion

1. Characterization of the nitrogen-treated macro-/mesoporous TiO_2 nanostructure

Figure 3-1a shows the low- and high-magnification scanning electron microscope (SEM) images of hierarchical macro-/mesoporous TiO_2 prepared at room temperature. As shown in Fig. 1a, the as-synthesized macro-/mesoporous TiO_2 exhibits relatively homogeneous and long-range periodical pores with pore diameters of 2-6 μm and pore-wall thicknesses around 2-4 μm. In addition, it can also be clearly seen that the

pore-walls of the macroporous TiO_2 are composed of small-interconnected TiO_2 particles with sizes from tens of nm to one hundred nm (the inset of Figure 3-1a). Yu's group reported a similar nanostructure of TiO_2 synthesized *via* a different titanium salt as the reactant.[20] However, our macro-/mesoporous TiO_2 shows more visible mesopores in SEM images and a higher specific surface area (to be discussed later), which will provide larger interface for lithium ion intercalation reactions. After calcination under nitrogen or air atmosphere at 300 °C for 3 h, the morphology of the macro-/mesoporous structure had no obvious change (Figure 3-1b and c). Although SEM images do not show noticeable morphology difference between nitrogen-treated TiO_2 and air- treated TiO_2, nitrogen adsorption isotherms and XRD patterns reveal remarkable differences between them in surface area and crystallinity.

The effect of atmosphere calcination on crystallinity evolution of TiO_2 was studied by XRD and the patterns are shown in Figure 3-1d. After calcination at 300 °C for 3 h, the sample under the air atmosphere (TiO_2-A) exhibits a typical anatase crystal structure, although TiO_2-A is not fully crystallized due to the relatively low calcination temperature. Compared to TiO_2-A, the nitrogen-treated sample TiO_2-N shows much lower crystallinity: only the first strongest diffraction peak of anatase TiO_2 can be observed, which suggests that nitrogen atmosphere had inhibition effects on the TiO_2 phase transition. This inhibition effect was also observed in other papers that used nitrogen atmosphere in calcining samples.[21,22]

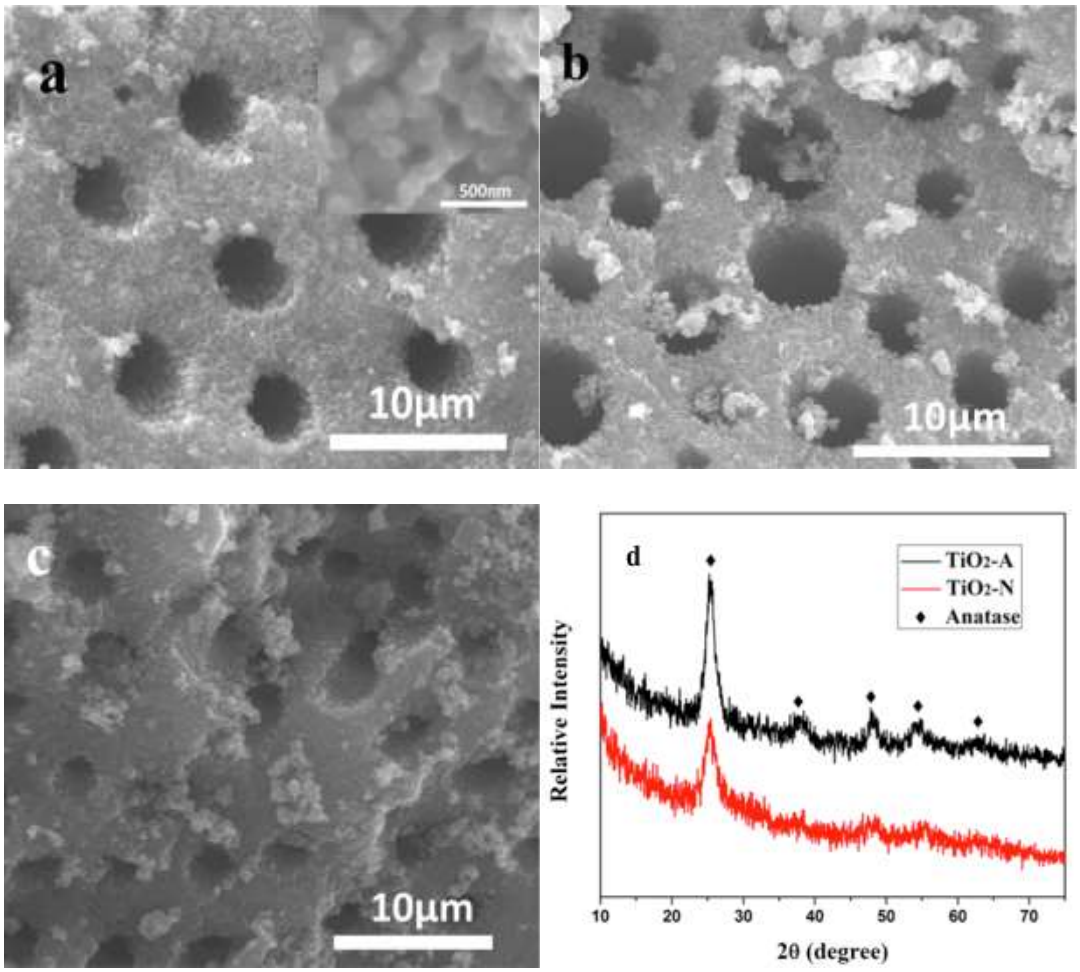

Figure 3-1. SEM images of macro-/mesoporous TiO_2 before a) and after calcination at 300 °C for 3h under nitrogen b) and air c) atmosphere, respectively, d) XRD patterns of TiO_2 samples calcined under air (TiO_2-A) and nitrogen (TiO_2-N) atmosphere at 300 °C for 3 h.

Figure 3-2 shows the nitrogen adsorption–desorption isotherm curves of TiO_2, TiO_2-A, and TiO_2-N. The specific surface area of these three samples were calculated using the BJH method to be 473.5 m^2 g^{-1}, 330.2 m^2 g^{-1}, and 248.1 m^2 g^{-1}, respectively (TiO_2, TiO_2-N and TiO_2-A). They are much higher than that of the similar TiO_2 nanostructure reported in the literature.[20] As shown in Figure 3-2a, all these samples have type I isotherm curves and exhibit no adsorption hysteresis. Besides, all the isotherm curves have two very distinct regions: at the low relative pressure, the

isotherm curves exhibit high adsorption, suggesting the presence of micropores. However, when the pressure approaches the saturation vapor pressure, the isotherm curves exhibit a very fast increase, suggesting that there are gaps between micro-particles, which can induce a phenomenon similar to macropores' adsorption. Meanwhile, the adsorption isotherm of the TiO_2 sample exhibits a large increase in the relative pressure (P/P_0) range of 0.2–0.4, which is characteristic of capillary condensation within mesopores.[23] Figure 3-2b shows the corresponding pore-size distribution curves of the TiO_2 samples. It can be observed that the all these three TiO_2 samples exhibit a narrow pore-size distribution range centered at 2 nm (Figure 3-2b inset), which indicates that this hierarchical macro-/mesoporous nanostructure TiO_2 is stable under calcination at 300 °C for 3h. It is well-known that thermal

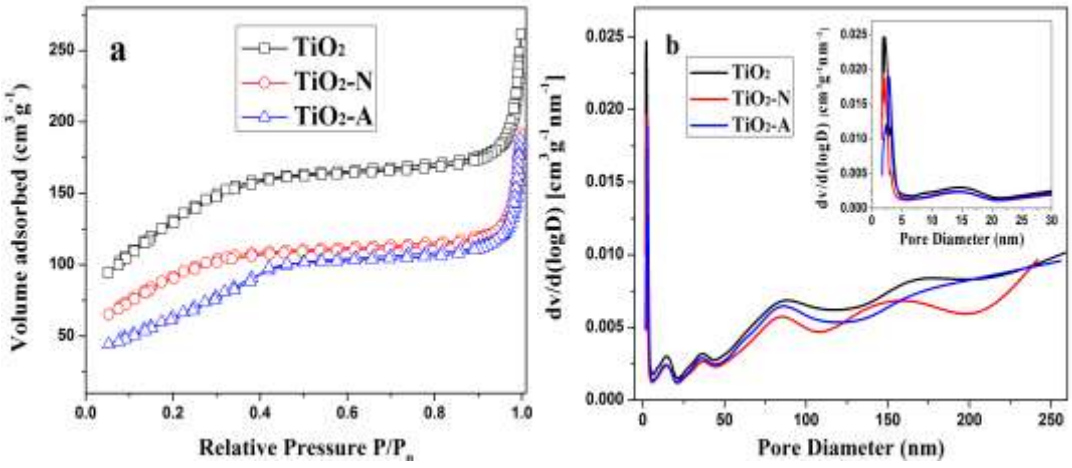

Figure 3-2. a) Nitrogen-adsorption–desorption isotherms and b) pore-size distribution curves of TiO_2, TiO_2-N and TiO_2-A (the inset shows an expanded view of the small diameter region of the plots).

treatment will decrease the specific surface area of oxides because of particle growth and agglomeration.[24] However, the nitrogen environment leads to less surface area

reduction than air environment, which can be ascribed to the oxygen-deficiency environment that inhibits particle growth.[25]

To get more insight into the effect of nitrogen atmosphere in the calcination process, the surface element compositions of TiO_2-N and TiO_2-A were studied by XPS. As shown in Figure 3-3a, sample TiO_2-A exhibits two clear peaks at binding energies of 458.33 and 464.19 eV in the Ti 2p high-resolution spectrum, which correspond well to the Ti $2p_{3/2}$ and Ti $2p_{1/2}$ peaks of Ti^{4+}.[26,27] Compared to TiO_2-A, TiO_2-N has two similar peaks that belong to Ti $2p_{3/2}$ and Ti $2p_{1/2}$ peaks of Ti^{4+} with the binding energies of 458.50 and 464.19 eV.[27,28] However, in addition to these peaks, there is another small peak existing at a binding energy of 457.90 eV in the spectrum of TiO_2-N, which could be assigned to the Ti^{3+} species according to the reference (Figure 3-3b).[29] The presence of Ti^{3+} suggests that oxygen vacancies also exist in sample TiO_2-N considering the charge balance principle. In other words, some defects were created on the surface of TiO_2 after calcination under nitrogen atmosphere.

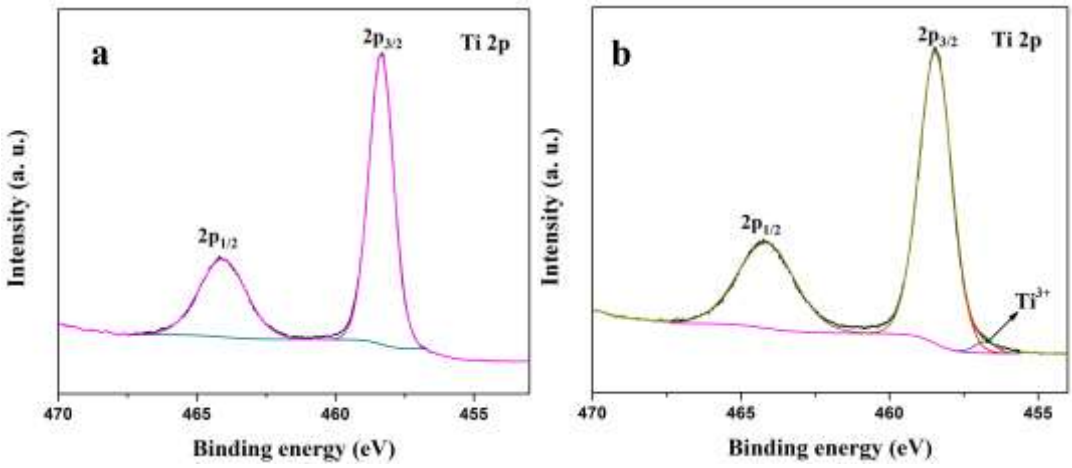

Figure 3-3. XPS spectra of TiO_2 samples: a) TiO_2-A, and b) TiO_2-N.

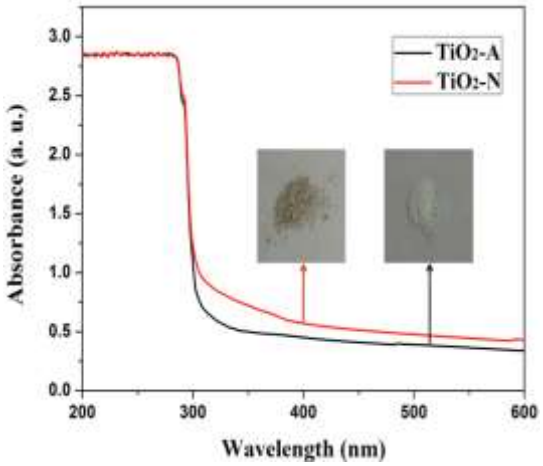

Figure 3-4. UV-visible absorption spectra of samples TiO_2-N and TiO_2-A.

Furthermore, the existence of surface defects was also demonstrated by UV-visible absorption spectra. As shown in Figure 3-4, in contrast to the air-treated sample TiO_2-A, an additional visible-light absorption shoulder appears around 320-450 nm in sample TiO_2-N, which is consistent with its yellow color as shown by the inset in Figure 3-4. This observed extra absorption shoulder was reported in the literature and was believed to be caused by defects corresponding to the existing Ti^{3+} species.[30,31] From the XPS and UV-Vis results, it can be deduced that there are some Ti^{3+} species and oxygen vacancies created after nitrogen calcination in our sample.

2. Lithium-ion intercalation properties investigation

To study the effects of various atmospheres' calcination on the performance of hierarchical macro-/mesoporous TiO_2 nanostructures as lithium ion storage electrodes at elevated temperatures, the lithium-ion insertion/extraction properties of macro-/mesoporous TiO_2-N and TiO_2-A were evaluated by galvanostatic discharge/charge tests at 55 °C for 50 cycles. Figure 3-5 shows the discharge and charge curves of these two samples in the first and last 3 cycles at a discharge/charge

current density of 30 mA g^{-1} in the potential window of 1-2.5 V. It is observed that the initial discharge capacities of TiO_2-N and TiO_2-A are 360 mAh g^{-1} and 496 mAh g^{-1}, respectively. As shown in Figure 3-5a, TiO_2-A shows plateaus at approximately 1.8 V (discharge process) and 1.9 V (charge process) during the first 3 cycles, which is similar to reported nanostructured anatase.[9] In the last 3 cycles, both the discharge and charge plateaus become much less well-defined. Correspondingly, the discharge capacity is only 187 mAh g^{-1} at the 50th cycle. However, this plateau shrinkage is remarkably less noticeable in TiO_2-N. As shown in Figure 3-5b, TiO_2-N exhibits plateaus of relatively shorter length than TiO_2-A during the first 3 cycles, which suggests its less crystallinity and agrees well with the XRD finding for these two samples. However, unlike in TiO_2-A, the position and size of these plateaus in TiO_2-N show negligible change after 50 cycles, suggesting that the crystal structure of TiO_2-N experiences little change after cycling at elevated temperatures. Above results indicate that surface defects created by nitrogen-based calcination contributed to the stabilization of the intercalation capacity of macro-/mesoporous TiO_2.[32] In comparison, these two samples were also tested at room temperature for their lithium ion intercalation properties by running the same 50-cycle measurement. For the air-treated TiO_2, plateau shrinkage was also observed but less noticeable than that of the elevated-temperature measurement; in addition, the nitrogen-treated TiO_2 didn't show as much improvement on the stability of plateaus as at elevated temperature (Figure 3-6).

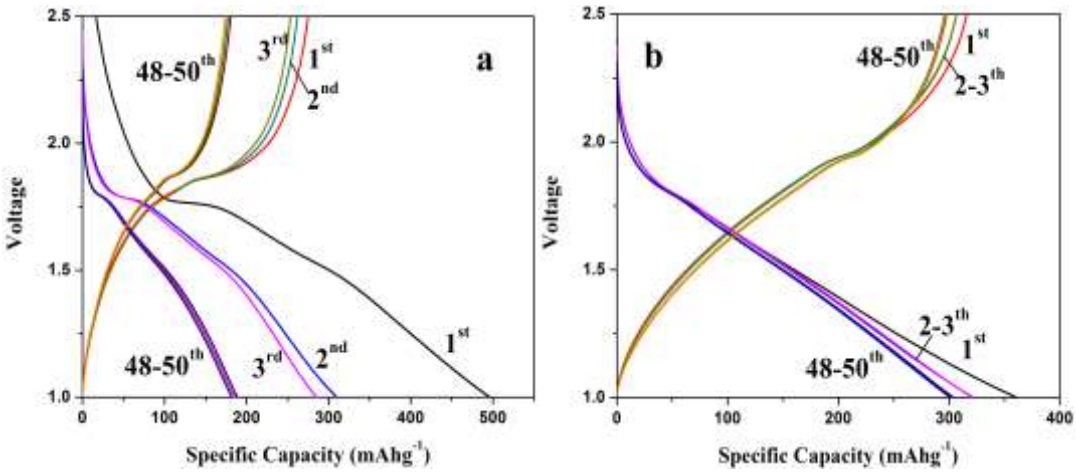

Figure 3-5. Galvanostatic discharge (lithium insertion)/charge (lithium extraction) curves vs. Li^+/Li of (a) TiO_2-A and (b) TiO_2-N at a current density of 30 mA g^{-1} in the first 3 and last 3 cycles of the 50-cycle tests at an elevated temperature of 55 ºC.

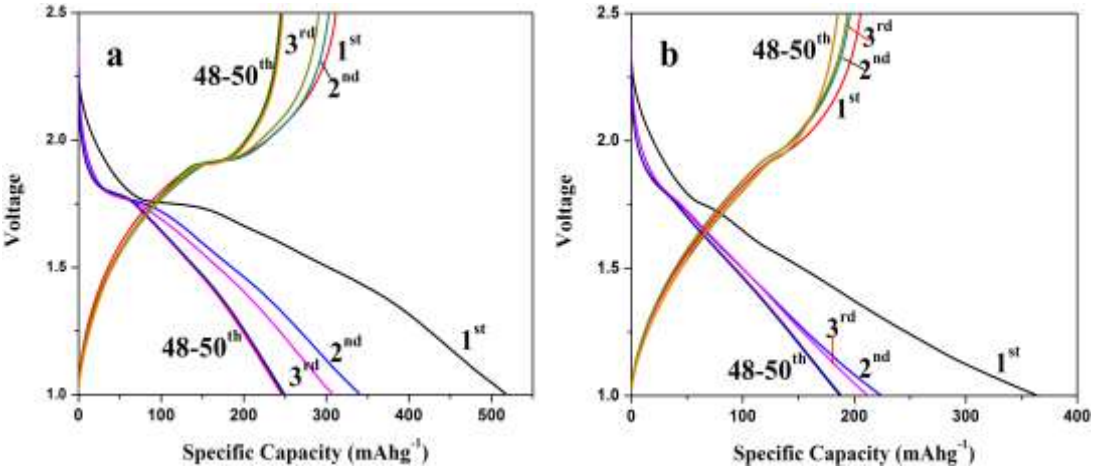

Figure 3-6. Galvanostatic discharge (lithium insertion)/charge (lithium extraction) curves vs. Li^+/Li of (a) TiO_2-A and (b) TiO_2-N at a current density of 30 mA g^{-1} in the first 3 and last 3 cycles of the 50-cycle tests at room temperature.

Figure 3-7a displays the cyclic performance of these two samples in the 50-cycle test at 55 °C at different current densities of 30 mA g^{-1}, 150 mA g^{-1} and 500 mA g^{-1}. As shown in Figure 3-7a, TiO_2-A exhibits a much higher discharge capacity in the first cycle than TiO_2-N. The capacity is 496 mAh g^{-1}. However, this capacity drops continuously, with a capacity of 187 mAh g^{-1} left after 50 cycles and the capacity retention rate is only 31.7%. Furthermore, its rate performance is also poor: the

discharge capacity is 147 mAh $g^{-1}$and 76 mAh g^{-1} at the current densities of 150 mA g^{-1} and 500 mA g^{-1}， respectively. This obvious performance degradation was greatly inhibited when the nitrogen-treated sample TiO_2-N was used as the electrode material. As shown in the same figure, TiO_2-N starts with a relatively lower initial discharge capacity of 360 mAh g^{-1} but experiences much less capacity degradation in the first 10 cycles. The rate performance of TiO_2-N is also obviously better than TiO_2-A: its discharge capacity is 248 mAh g^{-1} at a current density of 150 mA g^{-1} and 181 mAh g^{-1} at a current density of 500 mA g^{-1}. When the current density is changed back to 30 mA g^{-1}, its discharge capacity is 301 mAh g^{-1}, which shows little capacity fading in the following cycles and is still as high as 293 mAh g^{-1} at the 50th cycle. The capacity retention rate is 84.1% after 50 cycles at different current densities. However, this notable performance improvement of TiO_2-N cannot be observed when these two samples were tested at room temperature. Although TiO_2-N exhibited decent cyclic stability, its capacity was obviously lower than TiO_2-A in each cycle of a similar 50-cycle test (Figure 3-8a). This demonstrates that while the existence of surface defects of Ti^{3+} species and oxygen vacancies on the electrode surface might improve the electrode performance at elevated temperatures significantly, they diminish the room temperature performance.

According to above results, we can conclude the reasons as below: the nitrogen-treated TiO_2 would have a thin layer of surface defects after calcination, which enhanced the initial electrical conductivity of the electrode (Figure 3-7c). However, these surface defects also resulted in an extra less active layer by reducing

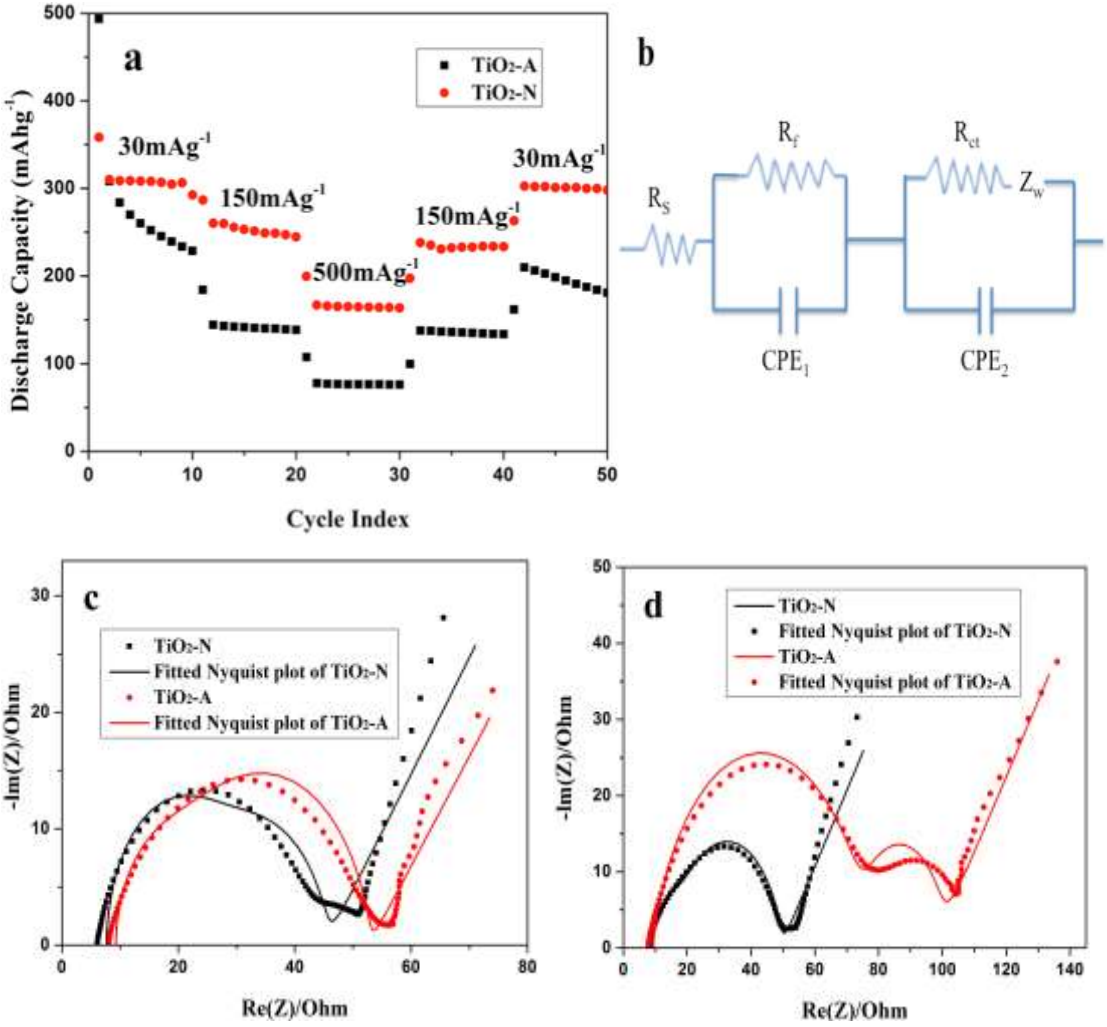

Figure 3-7. a) Rate performances of TiO_2-N and TiO_2-A, measured at various current densities of 30, 150 and 500 mAh g^{-1}, with a voltage window between 1.0–2.5 V at 55 °C, b) The equivalent circuit of EIS, c) and d) Nyquist and fitted plots of TiO_2-N and TiO_2-A before and after cycling.

the number of available Ti^{4+} that can transform to Ti^{3+} compared to the pristine TiO_2. This explained why the nitrogen-treated TiO_2 (TiO_2-N) exhibited lower initial capacity compared to the air-treated TiO_2 (TiO_2-A) during cycling at both room and elevated temperatures. This less active layer also increased the Li-ion diffusion path length into TiO_2-N, causing poor cyclic stability at room temperature. However, at the elevated temperature, the diffusion coefficient of Li-ion diffusion would increase,[33] which enhanced the insertion/extraction speed of lithium ions into the TiO_2,

compensating for the longer diffusion path. In addition, the common problem of excessive electrode and electrolyte reactions at elevated temperatures were alleviated

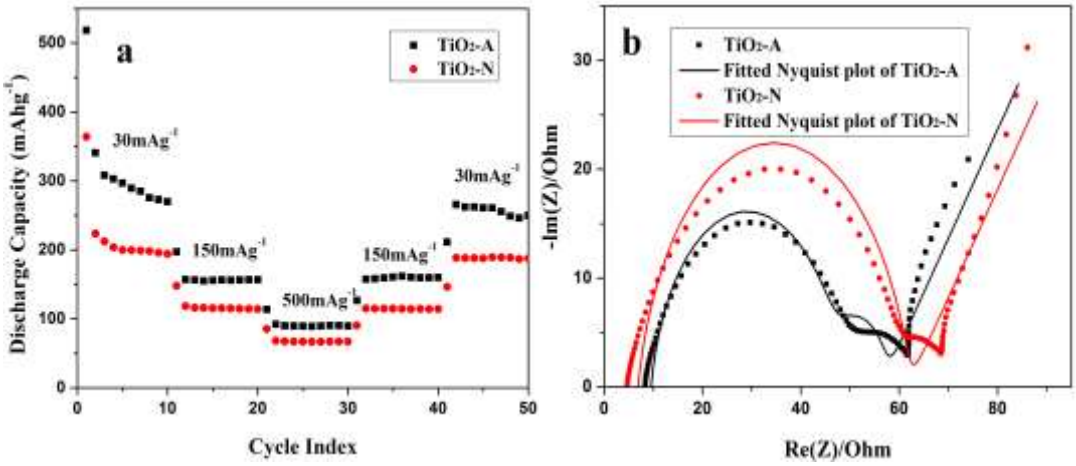

Figure 3-8. a) Rate performances of TiO_2-N and TiO_2-A, measured at various current densities of 30, 150 and 500 mAh g^{-1}, with a voltage window between 1.0-2.5 V at room temperature, and b) Nyquist and fitted plots of TiO_2-N and TiO_2-A after cycling.

by the existence of the surface defects, which would act as protective barrier layer between the liquid electrolyte and the electrode surface to inhibit electrolyte oxidization during cycling and the HF etching generated by trace amount of moisture reacting with $LiPF_6$ based electrolyte.[34,35] As a result, TiO_2-N has a noticeably better cyclic stability at 55 °C than at room temperature. Similar results have also been reported by other research groups where surface modified samples had worse cyclic performances at room temperature than the pristine ones.[36-38]

Meanwhile, above electrochemical test results at the elevated temperature are also supported by the measurement of the kinetic properties of these samples. Electrochemical impedance spectroscopy (EIS) was used to test the resistance before and after electrochemical cyclic tests. Figure 3-7b shows the equivalent circuit for

fitting Nyquist plots: R_s, R_f and R_{ct} are ohmic resistance (total resistance of the electrolyte, separator and electrical contacts), film resistance and charge transfer resistance respectively, and Z_w represents the Warburg impedance of Li ion diffusion into active materials. CPE is the constant phase-angle element, involving double layer capacitance. Figure 3-7c and d show the fitted Nyquist plots of these two samples before and after cycling at 55 °C by using the equivalent circuit. Before cycling, it is found that nitrogen-treated sample TiO_2-N (37 Ω) has a smaller charge transfer resistance than air-treated sample TiO_2-A (45 Ω) (Figure 3-7c). After cycling, the charge transfer resistance of sample TiO_2-N (41 Ω) increases slightly while that of sample TiO_2-A increases to almost double its value before cycling (89 Ω) (Figure 3-7d). For both of the samples, the charge transfer resistance increased after test due to the complicated interface formation between the electrode and electrolyte during cycling. However, for TiO_2-N, due to the calcination in a non-oxidizing environment, the existence of surface defects acted as a thin layer of conductive coating, which would inhibit the charge transfer resistance increase from the formed complex interface. Therefore, it only had a little increase after 50 cycles. By contrast, there was no such inhibition effect existing for TiO_2-A. As a result, the charge transfer resistance increased to almost double its pre-cycling value after cycling. In addition, the charge transfer resistance of these two samples is in the order of TiO_2-N (56 Ω) > TiO_2-A (48 Ω) tested after cycling at room temperature, which also agrees well with the result of discharge capacities for these two samples (Figure 3-8b). It is well-known that thermal treatment in a non-oxidizing environment will enhance the

electrical conductivity of TiO_2,[17-19,39] which is also observed in the EIS results of sample TiO_2-N and TiO_2-A before cycling. However, for the nitrogen-treated TiO_2 here, the result shows that the introduction of surface defects has little effect on the improvement of electrochemical performance of TiO_2 tested at room temperature. A similar enhancement like other gas-thermal treatment[17-19,39] will be observed if the nitrogen-treated TiO_2 is tested at elevated temperatures. This result also agrees well with the EIS result after cycling at elevated and room temperature, respectively. The TiO_2-N shows little increase at elevated temperatures but obvious increase at room temperature (Figure 3-7d and Figure 3-8b). Therefore, it can be found that nitrogen-based calcination can improve the charge transfer process at the electrode/electrolyte interface and maintain good electronic conductivity during long-term cycling at elevated temperatures. Thus, this improved interface property is considered to be a factor in improving the performance of TiO_2-N at elevated temperatures.

Base on above results, we can deduce the effects of nitrogen treatment in this experiment as follows: the nitrogen calcination created Ti^{3+} and oxygen vacancies on the surface of macro-/mesoporous TiO_2, which are important for the cyclic stability of nanostructured TiO_2 as lithium ion battery anode at elevated temperatures. It is reasonable that elevated temperatures can contribute to a high capacity compared to room temperature. However, without these surface defects, the capacity degradation will be obvious during cycling as demonstrated in TiO_2-A. With these surface defects, the capacity retention is much better as demonstrated in TiO_2-N. These surface

defects are just acting as a thin layer of conductive coating because of the narrowed intrinsic banding gap of TiO_2,[40] which will enhance the performance of electrodes in two aspects. On one hand, it increases conductivity (lower resistance and better rate performance); on the other hand, it protects the electrode surface at elevated temperatures to keep interface stability. All these reasons explain why nitrogen-treated sample TiO_2-N possesses a better electrochemical performance than air-treated one (TiO_2-A).

D. Conclusions

In summary, hierarchical macro-/mesoprous TiO_2 were prepared and calcined under different atmospheres (nitrogen and air). Nitrogen-treated and air-treated TiO_2 exhibited varied crystallinity, surface chemistry, and electrochemical performance. Compared to air-treated TiO_2, nitrogen-treated TiO_2 exhibited notable improvement in the electrochemical performance when used as a lithium ion battery electrode at elevated temperatures. This improvement can be ascribed to the contribution of surface defects, in addition to higher specific surface area and lower crystallinity. The existence of Ti^{3+} species and oxygen vacancies not only enhanced the charge-transfer conductivity but also behaved as a protecting layer to ensure the interface stability of the TiO_2 sample during cycling. This proposed calcination strategy would provide a novel and feasible method in the development of high performance materials used in lithium ion batteries at elevated temperatures and relevant fields.

References

[1] B. Scrosati, “Recent Advances in Lithium Ion Battery Materials,” *Electrochim. Acta*, **45** 2461-2466 (2000).

[2] N.-S. Choi, Z.H. Chen, S.A. Freunberger, X.L. Ji, Y.K. Sun, K. Amine, G, Yushin, L.F. Nazar, J. Cho, and P.G. Bruce, “Challenges Facing Lithium Batteries and Electrical Double-Layer Capacitors,” *Angew. Chem. Int. Ed.*, **51** 9994 (2012).

[3] M. Broussely, P. Biensan, and B. Simon, “Lithium Insertion Into Host Materials: the Key to Success for Li Ion Batteries,” *Electrochim. Acta*, **45** 3-22 (1999).

[4] A.M. Andersson, and K. Edström, “Chemical Composition and Morphology of the Elevated Temperature SEI on Graphite,” *J. Electrochem. Soc.*, **148** A1100-A1109 (2001).

[5] A.M. Andersson, K. Edström, and J.O. Thomas, “Characterization of the Ambient and Elevated Temperature Performance of a Graphite Electrode,” *J. Power Sources*, **81** 8-12 (1999).

[6] J.W. Xu, C.H. Jia, B. Cao, and W.F. Zhang, “Electrochemical Properties of Anatase TiO_2 Nanotubes as an Anode Material for Lithium-Ion Batteries,” *Electrochim. Acta*, **52** 8044-8047 (2007).

[7] T. Fröschl, U. Hörmann, P. Kubiak, G. Kucěrovoa, M. Pfanzelt, C.K. Weiss, R.J. Behm, N. Hüsing, U. Kaiser, K. Landfester, and M. Wohlfahrt-Mehrens, “High Surface Area Crystalline Titanium Dioxide: Potential and Limits in Electrochemical Energy Storage and Catalysis,” *Chem. Soc. Rev.*, **41** 5313-5360 (2012).

[8] S. Yang, X. Feng, and K. Muellen, “Sandwich-Like, Graphene-Based Titania Nanosheets with High Surface Area for Fast Lithium Storage,” *Adv. Mater.*, **23** 3575−3579 (2011).

[9] I. Moriguchi, R. Hidaka, H. Yamada, T. Kudo, H. Murakami, and N. Nakashima, “A Mesoporous Nanocomposite of TiO_2 and Carbon Nanotubes as a High-Rate Li-Intercalation Electrode Material,” *Adv. Mater.*, **18** 69-73 (2006).

[10] H. Han, T. Song, E.K. Lee, A. Devadoss, Y. Jeon, J. Ha, Y.C. Chung, Y.M. Choi, Y.G. Jung, and U. Paik, “Dominant Factors Governing the Rate Capability of a TiO_2 Nanotube Anode for High Power Lithium Ion Batteries,” *ACS Nano*, **6** 8308-8315 (2012).

[11] J. Liu, J.S. Chen, X. Wei, X.W. Lou, and X.W. Liu, “Sandwich-Like, Stacked Ultrathin Titanate Nanosheets for Ultrafast Lithium Storage, *Adv. Mater.*, **23** 998-1002 (2011).

[12] J. Ye, W. Liu, J. Cai, S. Chen, X. Zhao, H. Zhou, and L. Qi, "Nanoporous Anatase TiO_2 Mesocrystals: Additive-free Synthesis, Remarkable Crystalline-Phase Stability, and Improved Lithium Insertion Behavior," *J. Am. Chem. Soc.*, **133** 933-940 (2011).

[13] P.G. Bruce, B. Scrosati, and J.M. Tarascon, "Nanomaterials for Rechargeable Lithium Batteries," *Angew. Chem. Int. Ed.*, **47** 2930-2946 (2008).

[14] G.D. Du, Z.P. Guo, P. Zhang, Y. Li, M.B. Chen, D. Wexler, and H.K. Liu, "SnO_2 Nanocrystals on Self-organized TiO_2 Nanotube Array as Three-Dimensional Electrode for Lithium Ion Microbatteries," *J. Mater. Chem.*, **20** 5689-5694 (2010).

[15] W. Zhang, W.D. Zhou, J.H. Wright, Y.N. Kim, D.W. Liu, and X.C. Xiao, "Mn-Doped TiO_2 Nanosheet-Based Spheres as Anode Materials for Lithium-Ion Batteries with High Performance at Elevated Temperatures," *ACS Appl. Mater. Interfaces*, **6** 7292-7300 (2014).

[16] J.W. Zhang, J.W. Zhang, Z.S. Jin, Z.S. Wu, and Z.J. Zhang, "Electrochemical Lithium Storage Capacity of Nickel Mono-oxide Loaded Anatase Titanium Dioxide Nanotubes," *Ionics*, **18** 861-866 (2012).

[17] J.-Y. Shin, J.H. Joo, D. Samuelis, and J. Maier, "Oxygen-Deficient $TiO_{2-\delta}$ Nanoparticles *via* Hydrogen Reduction for High Rate Capability Lithium Batteries," *Chem. Mater.*, **24** 543-551 (2012).

[18] D. Liu, Y. Zhang, P. Xiao, B.B. Garcia, Q. Zhang, X. Zhou, Y.-H. Jeong, and G.Z. Cao, "TiO_2 Nanotube Arrays Annealed in CO Exhibiting High Performance for Lithium Ion Intercalation," *Electrochim. Acta*, **54** 6816 (2009).

[19] D.W. Liu, Y.Y. Liu, A.Q. Pan, K.P. Nagle, G.T. Seidler, Y.H. Jeong, and G.Z. Cao, "Enhanced Lithium-Ion Intercalation Properties of V_2O_5 Xerogel Electrodes with Surface Defects," *J. Phys. Chem. C*, **115** 4959 (2011).

[20] J. Yu, Y. Su, and B. Cheng, "Template-Free Fabrication and Enhanced Photocatalytic Activity of Hierarchical Macro/Mesoporous Titania," *Adv. Funct. Mater.*, **17** 1984-1990 (2007).

[21] M. Kitano, K. Funatsu, M. Matsuoka, M. Ueshima, and M. Anpo, "Preparation of Nitrogen-Substituted TiO_2 Thin Film Photocatalysts by the Radio Frequency Magnetron Sputtering Deposition Method and Their Photocatalytic Reactivity under Visible Light Irradiation," *J. Phys. Chem. B*, **110** 25266-25272 (2006).

[22] J. Wang, D.N. Tafen, J.P. Lewis, Z.L. Hong, A. Manivannan, M. Zhi, M. Li, and N.Q. Wu, "Origin of Photocatalytic Activity of Nitrogen-Doped TiO_2 Nanobelts," *J. Am. Chem. Soc.*, **131** 12290-12297 (2009).

[23] S. Lowell, J.E. Shields, M.A. Thomas, and M. Thommes, *Characterization of Porous Solids and Powders: Surface Area, Pore Size and Density*, Kluwer, London, 2004.

[24] S. Yamanaka, and G.W. Brindley, "High Surface Area Solids Obtained by Reaction of Montmorillonite with Zirconyl Chloride," *Clays Clay Miner.*, **27** 119-124 (1979).

[25] X.Y. Pan, M.-Q. Yang, X.Z. Fu, N. Zhang, and Y.-J. Xu, "Defective TiO_2 with Oxygen Vacancies: Synthesis, Properties and Photocatalytic Applications," *Nanoscale*, **5** 3601-3614 (2013).

[26] R.P. Netterfield, P.J. Martin, C.G. Pacey, W.G. Sainty, and D.R. Mckenzie, "Ion-Assisted Deposition of Mixed TiO_2-SiO_2 Films," *J. Appl. Phys.*, **66** 1805 (1989).

[27] R. Sanjines, H. Tang, H. Berger, F. Gozzo, G. Margaritondo, and F. Levy, "Electronic Structure of Anatase TiO_2 Oxide," *J. Appl. Phys.*, **75** 2945 (1994).

[28] V.I. Nefedov, Y.V. Salyn, A.A. Chertkov, and L.N. Padurets, "X-ray Electron Study of the Electron Density Distribution in Hydrides of the Transition Elements," *Zh. Neorg. Kimii*, **16** 1443-1445 (1974).

[29] C.M. Chan, S. Trigwell, and T. Duerig, "Oxidation of an NiTi Alloy," *Surf. Interface Anal.*, **15** 349-354 (1990).

[30] H. Noda, K. Oikawa, T. Ogata, K. Matsuki, and H. Kamata, "Preparation of Titanium (IV) Oxides and Its Characterization," *Chem. Soc. Jpn.*, **8** 1084 (1986).

[31] G. Liu, Y.N. Zhao, C.H. Sun, F. Li, G.Q. Lu, and H.M. Cheng, "Synergistic Effects of B/N Doping on the Visible-Light Photocatalytic Activity of Mesoporous TiO_2," *Angew. Chem. Int. Ed.*, **47** 4516 (2008).

[32] M.V. Ganduglia-Pirovano, and J. Sauer, "Stability of Reduced V_2O_5 (001) Surfaces," *Phys. Rev. B*, **70** 045422 (2004).

[33] P. Xu, B.N. Popov, J.A. Ritter, and R.E. White, "Determination of Lithium Ion Diffusion Coefficient in Graphite," *J. Electrochem. Soc.*, **146** 8 (1999).

[34] L. Yu, X. Qiu, J. Xi, W. Zhu, and L. Chen, "Enhanced High Potential and Elevated Temperature Cycling Stability of $LiMn_2O_4$ Cathode by TiO_2 Modification for Li-Ion Battery," *Electrochim. Acta*, **51** 6406 (2006).

[35] S.T. Myung, K. Izumi, S. Komaba, Y.K. Sun, H. Yashiro, and N. Kumagai, "Role of Alumina Coating on Li-Ni-Co-Mn-O Particles as Positive Electrode Material for Lithium-Ion Batteries," *Chem. Mater.*, **17** 3695 (2005).

[36] W.H. Jang, M.C. Kim, S.H. Kim, V. Aravindan, W.S. Kim, W.S. Yoon, and Y.S. Lee, "Understanding the Exceptional Elevated Temperature Performance of High Voltage $LiNi_{0.5}Mn_{1.5}O_4$ Cathodes by $LiFePO_4$ Modification," *Electrochim. Acta*, **137** 404 (2014).

[37] K.A. Walz, C.S. Johnson, J. Genthe, L.C. Stoiber, W.A. Zeltner, M.A. Anderson, and M.M. Thackeray, "Elevated Temperature Cycling Stability and Eectrochemical Impedance of $LiMn_2O_4$ Cathodes with Nanoporous ZrO_2 and TiO_2 Coatings," *J. Power Sources*, **195** 4943 (2010).

[38] Y.L. Chen, V. Aravindan, and S. Madhavi, "Improved Elevated Temperature Performance of Al-intercalated V_2O_5 Electrospun Nanofibers for Lithium-Ion Batteries," *ACS Appl. Mater. Interfaces*, **4** 3270 (2012).

[39] S.M. Dong, X. Chen, L. Gu, X.H. Zhou, H.X. Xu, H.B. Wang, Z.H. Liu, P.X. Han, J.H. Yao, L. Wang, G.L. Cui, and L.Q. Chen, "Facile Preparation of Mesoporous Titanium Nitride Microspheres for Electrochemical Energy Storage," *ACS Appl. Mater. Interfaces*, **3** 93-98 (2011).

[40] P. Liu, G. Liu, and H.-M. Cheng, "Nitrogen Vacancy-Promoted Photocatalytic Activity of Graphitic Carbon Nitride," *J. Phys. Chem. C*, **116** 11013-11018 (2012).

FACILE SYNTHESIS OF NANOCOMPOSITES FOR HIGH PERFROMANCE LITHIUM-ION BATTERY ANODES

A. Introduction

Lithium-ion batteries (LIBs) have been considered to be one of the most promising energy storage devices for powering electric vehicles and other large-scale facilities.[1-3] In the previous chapters, we have demonstrated the important of using surface-modified approaches (doping and atmosphere calcination) to enhance the performance of nanostructured TiO_2, which show obvious improvement on the both capacity and cyclic stability compared to bare ones. Besides TiO_2, lithium titanate ($Li_4Ti_5O_{12}$) has also been recognized as one high-profile alternative to carbonaceous anodes, which suffer well-known safety issues due to their unique, intrinsic characteristics.[4-6] One of the notable advantages of $Li_4Ti_5O_{12}$ (LTO) is that it does not undergo significant structure change during lithiation, which makes it a zero-strain insertion material.[7,8] In addition, the high thermodynamic stability of LTO will address the safety limitations of lithium-ion batteries in the applications.[9-11] Zhong *et al.* reported that $Li_4Ti_5O_{12}$ can be lithiated up to $Li_{8.5}Ti_5O_{12}$, which provides a theoretical capacity about 1.5 times higher than that of the compound lithiated to $Li_7Ti_5O_{12}$ by means of first-principles calculations.[9] And Yi *et al.* also investigated the structure and thermal stability of LTO through density functional theory (DFT) plane-wave pseudopotential technique and experimental methods, indicating that LTO has very high structural and thermodynamic stability. The reason can be ascribed to

the strong covalent bonding characteristic between Ti and O according to the electron density difference diagram.[10] Another advantage of LTO is that it exhibits a flat potential plateau and high operating voltage of approximately 1.55 V vs. Li^+/Li, which can avoid excessive reduction of electrolyte on the surface of the electrode and formation of the solid-electrolyte interphase (SEI) layer.[12,13] These two features make it a promising candidate for the anode material of LIBs. However, LTO also suffers major drawbacks, including low electronic conductivity (ca. 10^{-13} S cm^{-1}) and comparatively low theoretical capacity of 175 mAh g^{-1}.[14-16] To address the above issues, many efforts have been made to improve the capacity and conductivity of LTO. Common methods include reducing the particle size of the materials,[14] doping with foreign atoms,[17] and introducing conductive coatings.[18] For example, Bai et al. reported a La-doped $Li_4Ti_5O_{12}$, which exhibited excellent long-term cyclic stability, high coloumbic efficiency, and outstanding capacity retention at high current rates of 10-50 C. The reversible capacity was 157 mAh g^{-1} after 30 cycles at a rate of 0.1 C [17]. All of these methods significantly improve the electrochemical performance of LTO. However, most of the processes are either complicated or require specialized instruments.

Recently, combine LTO with other anode materials has been found to be an effective way of improving the performance of LTO electrodes. For example, there have been successful attempts involving graphene, Fe_2O_3, and TiO_2. [19-21] Through previous work, we have proved TiO_2 is one of the best candidates as a lithium ion host. Therefore, mixing LTO with TiO_2 is considered to be an advisable approach to

improve the capacity. Wang et al. reported a successful route to synthesize rutile terminated dual phase LTO-TiO_2 composites without other conductive materials. These composites exhibited much higher capacity than that of pure LTO at various rates.[22] Rahman et al. also developed amorphous carbon-coated dual phase LTO-TiO_2 (anatase) nanocomposites through *in situ* conversion of citric acid to amorphous carbon by low-temperature molten salt precipitation; such dual-phase LTO-TiO_2 possessed high capacity (166 mAh g^{-1} at a current density of 0.5 C) and excellent rate capability (110 mAh g^{-1} at a current density of 10 C).[23] However, the introduced TiO_2 (anatase) decreased the length of the typical potential plateau in LTO. In addition, the synthesis process was complicated and the amounts of the phases LTO and TiO_2 were not adjustable in the final products. Therefore, there is still an immediate need for a simple, low cost, and reliable synthesis method to fabricate homogeneous LTO-TiO_2 composites with the tunable phase assemblage that can be used as anode materials for lithium-ion batteries.

Therefore, in this chapter, we tried to enhance the performance of LTO *via* two aspects: phase tunable synthesis of LTO-TiO_2 composites and facile doping. The results were shown in part A and B. In part A: we reported a one-step room temperature approach for the rapid fabrication of LTO-TiO_2 nanoporous precursor, which was followed by a simple calcination to obtain homogeneous LTO-TiO_2 composites. Phases of the composites could be tuned by employing different calcination temperatures. In part B: we fabricated similar LTO-TiO_2 composites that were doped with nickel ion through our former ion-exchange approach. Finally, all

the samples in these two parts were calcined under the nitrogen atmosphere to create surface defects, which was believed to be a novel and useful way to improve the material's lithium ion intercalation performance by improving the conductivity of the composites.[24] These processes of synthesizing the LTO-TiO_2 composites has never before been reported. The as-prepared samples possessed high charge-discharge capacities and good cyclic performance and rate capability, when used as an anode material for lithium-ion batteries at both room temperature and 55 °C. They demonstrate a great practical application potential for the next generation of lithium ion batteries.

B. Facile Synthesis of Nanoporous $Li_4Ti_5O_{12}$-TiO_2 Composites

1. Experimental procedure

$Li_4Ti_5O_{12}$-TiO_2 (LTO-T-NPs) nanoporous precursors were synthesized by a one-step procedure at room temperature. Typically, lithium hydroxide monohydrate (ACS, Alfa Aesar) (1.3473 g, 32.1 mM) and hydrogen peroxide (ACS, 30.0-32.0 %, Fisher Chemical) (2.1632 mL) were mixed in deionized (DI) water (20 mL) at ambient temperature. The solution was stirred for 10 min using a magnetic stirrer. Then, titanium (IV) isopropoxide (TIP, 97%, Sigma-Aldrich) (2 mL, 6.6 mM) was added drop-wise to the solution without using any surfactant. The light yellow suspension was kept static and aging for 1 h before the precipitates were removed and washed with DI water three times. The obtained products were dried in air at 40 °C. Finally, the obtained precursors were calcined at 700 °C, 750 °C, and 800 °C for 2 h

under nitrogen atmosphere. Within this study, the samples are designated as LTO-T-NPs (precursor), S-700-N, S-750-N, and S-800-N (calcination at 700 °C, 750 °C, and 800 °C under nitrogen atmosphere), respectively. Structural characterization and electrochemical evaluation were similar to the previous chapters.

2. Results and discussion

2.1 Structural and morphological analysis

Figures 4-1a and 4-1b show typical scanning electron microscope (SEM) images of the nanoporous $Li_4Ti_5O_{12}$-TiO_2 precursor (LTO-T-NPs) prepared at room temperature. The SEM images clearly show that the as-synthesized nanoporous structure is composed of amorphous interconnected nanoparticles, which have diameters of around 100 nm. After calcination under nitrogen at 700, 750, and 800 °C for 2 h, all the as-obtained LTO-T-NPs remain in the original nanoporous morphology except for increased agglomeration between particles compared with the precursor. No fundamental morphology difference was observed between these samples (Figure 4-2). SEM images of the sample, calcined under nitrogen atmosphere at 750 °C (S-750-N), are shown in Figures 4-1c and 4-1d. It can be observed that nanoporous structure was still clearly seen in S-750-N, except that agglomeration was observed with obvious particle size increase. As the calcination temperature was increased in this experiment, the agglomeration would aggravate (Figure 4-2 c and d).

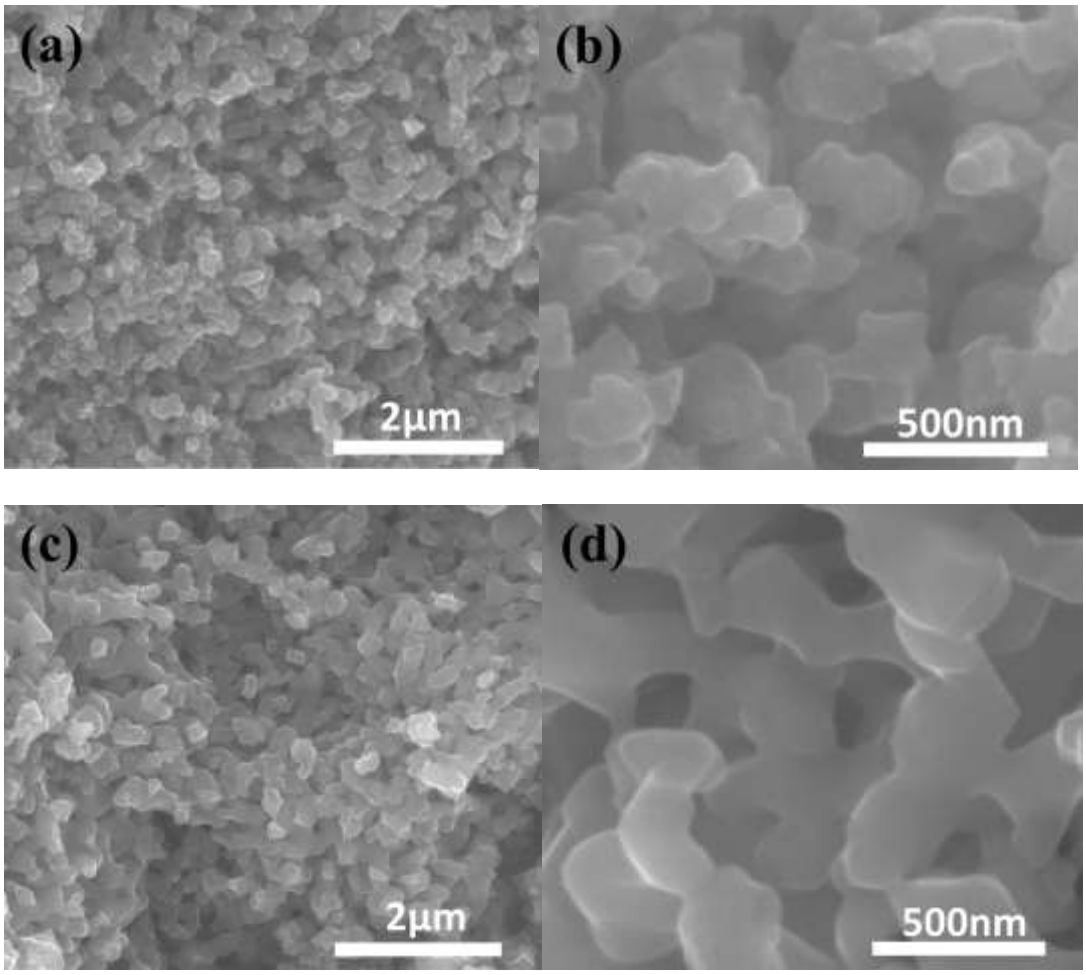

Figure 4-1. SEM images of LTO NPs structures obtained after different processes: low a) and high-magnification b) SEM images of LTO NPs precursor fabricated at room temperature; low c) and high-magnification d) SEM images of LTO NPs calcined under nitrogen atmosphere at 750 °C for 2 h.

To further investigate the structure and morphology of the synthesized LTO composites, transmission electron microscope (TEM) images and selected-area diffraction (SAED) patterns of S-750-N were shown in Figure 4-3. It can be clearly found that the nanograins comprised two components (Figure 4-3a and 4-3c), and the corresponding SAED proved the coexistence of TiO_2 rutile (Figure 4-3b) and $Li_4Ti_5O_{12}$ (Figure 4-3d), giving clear clues on the dual-phase formation of S-750-N.

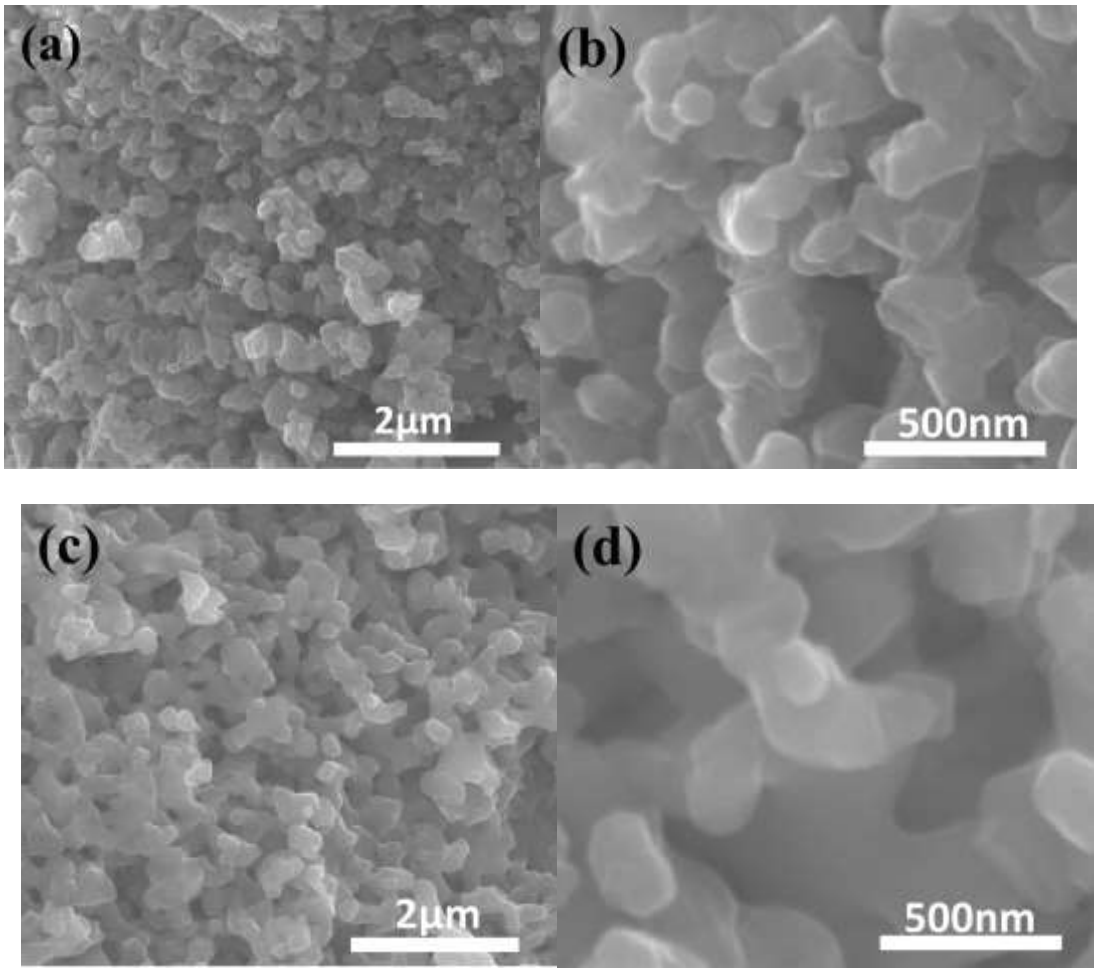

Figure 4-2. Low and high-magnification SEM images of LTO NPs calcined under nitrogen atmosphere at 700 °C a), b), and 800 °C c), d) for 2 h.

Furthermore, the high-resolution (HR) TEM images of S-750-N in Figure 2e-f provide clear microstructure details for the nanograins. The clear lattice fringes demonstrated the high crystallinity of the S-750-N, which is consistent with the sharp reflections in the XRD (Figure 4-4). The lattice fringes had spacings of 0.48 and 0.25 nm, corresponding to the {111} and {311} planes of the $Li_4Ti_5O_{12}$ (Figure 4-3f). Upon observation at HRTEM, the nanoporous S-750-N still had porous structures after calcination at a high temperature. The observed pores in Figure 4-3e ranged from 2-5 nm (a pore with ~ 4 nm diameter highlighted in Figure 4-3e).

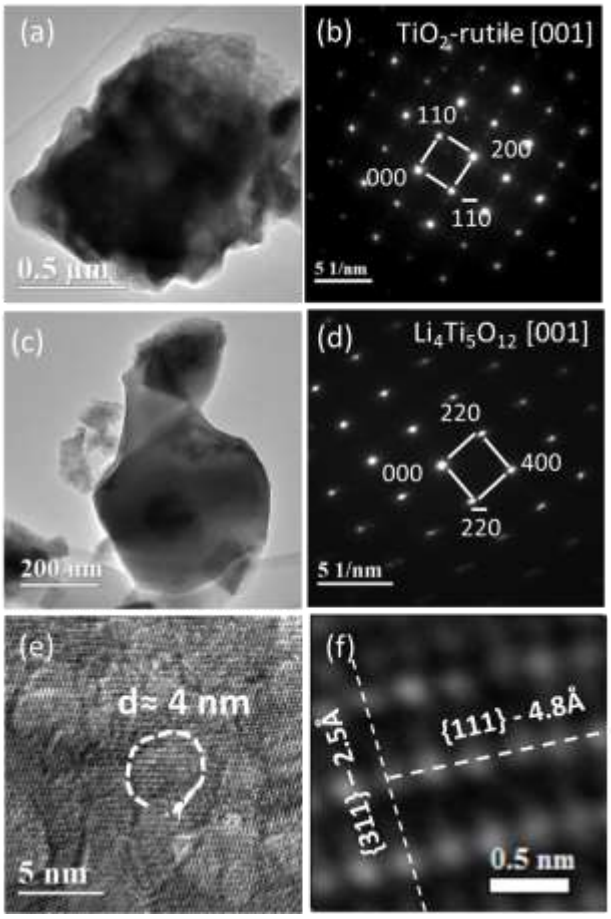

Figure 4-3. a, c)TEM images and b, d)corresponding SAED patterns of LTO NPs calcined under nitrogen atmosphere at 750 °C for 2 h (S-750-N), the SAED patterns showing the co-existence of LTO and rutile-TiO_2 in the composite; e, f) HRTEM images of S-750-N.

The effect of different calcination temperatures on the crystalline evolution of LTO NPs was studied *via* X-ray diffraction (XRD) and the diffraction patterns are shown in Figure 4-4. Before calcination, the room temperature synthesized LTO-T-NPs showed an amorphous crystal structure, no diffraction peaks could be observed in the XRD pattern. The only little diffraction peak existed around $2\theta \approx 66°$, which can be assigned to the background peak of the sample holder. After calcination under nitrogen atmosphere at 700, 750, and 800 °C for 2 h, all three samples (S-700-N, S-750-N, S-800-N) exhibited the spinel phase $Li_4Ti_5O_{12}$ (PDF No. 00-049-0207, space group

$Fd\bar{3}m$(227), a= 8.36 Å), and the peaks are indexed in Figure 4-4. In addition, diffraction peaks of rutile-TiO_2 (PDF No. 03-065-0191) are also observed in these three samples. Additional diffraction peaks of anatase-TiO_2 (PDF No. 01-071-1168) also appear when the samples were calcined at the temperature of 700 °C. As the calcination temperature was increased from 700 °C to 750 °C, anatase-TiO_2 transformed into rutile-TiO_2. At a further increased calcination temperature of 800 °C, the peak intensity of rutile-TiO_2 decreased with the increased intensity of $Li_4Ti_5O_{12}$ peaks. This result indicates that the phase composition of $Li_4Ti_5O_{12}$-TiO_2 (LTO-T) composites can be easily tuned by changing calcination temperature. Another noteworthy observed result is that the temperature required for the complete conversion from anatase-TiO_2 to rutile-TiO_2 is much higher than that of nanophase TiO_2 calcined in an ambient environment,[22,25,26] which suggests that nitrogen atmosphere has inhibiting effects on the samples' phase transition. This inhibiting effect was also reported in other papers.[27-29]

To further characterize the calcination effect on LTO NPs, we studied surface areas of the samples before and after calcination by using nitrogen adsorption-desorption measurements. Figure 4-5 shows the nitrogen adsorption-desorption isotherm curves of LTO-T-NPs, S-700-N, S-750-N, and S-800-N. The specific surface areas of these four samples were calculated using the BJH method, and found to be 78.7, 3.4, 2.4, and 1.6 $m^2\ g^{-1}$. As shown in Figure 4-5a, all these four samples have type I isotherm curves and exhibit no adsorption hysteresis. Besides, all the isotherm curves have two distinct regions: at the low relative pressure, the isotherm curves exhibit high

adsorption, suggesting the presence of micropores; when the pressure approaches the saturation vapor pressure, the isotherm curves exhibit a very fast increase, suggesting

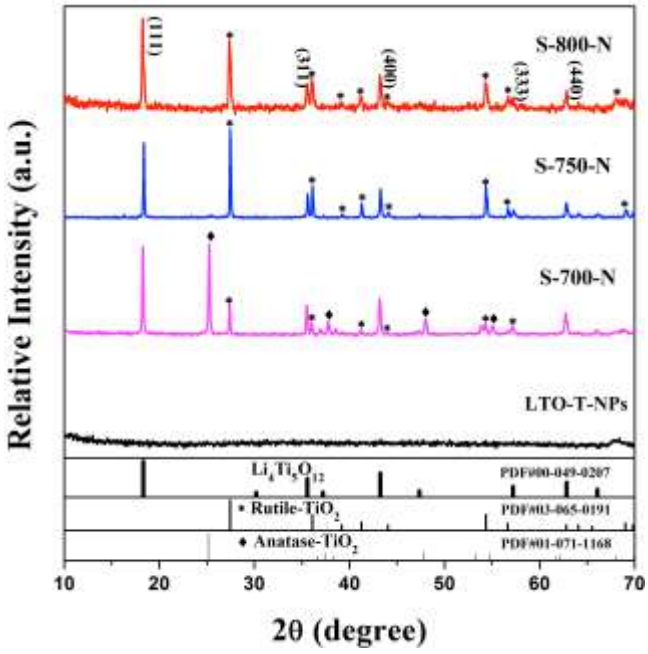

Figure 4-4. XRD patterns of the as-prepared LTO NPs, and corresponding samples calcined under nitrogen atmosphere at 700, 750, and 800 °C for 2h.

that there are gaps between micro-particles, which can induce a phenomenon similar to macropores' adsorption.[30] Corresponding pore-size distribution curves of these samples are shown in Figure 4-5b. As shown in this figure, pores with size of less than 100 nm decreased noticeably after calcination. However, the samples still exhibited large porosity with pore sizes under 100 nm, which agrees well with the TEM results. Above results explain the theory that thermal treatment decreases the specific surface area of materials because of particle growth and agglomeration.[31] However, the samples still keep the nanoporous structure after nitrogen calcination.

To get more insight into the effects of nitrogen atmosphere on the surface chemistry of the samples during the calcination process, surface element compositions

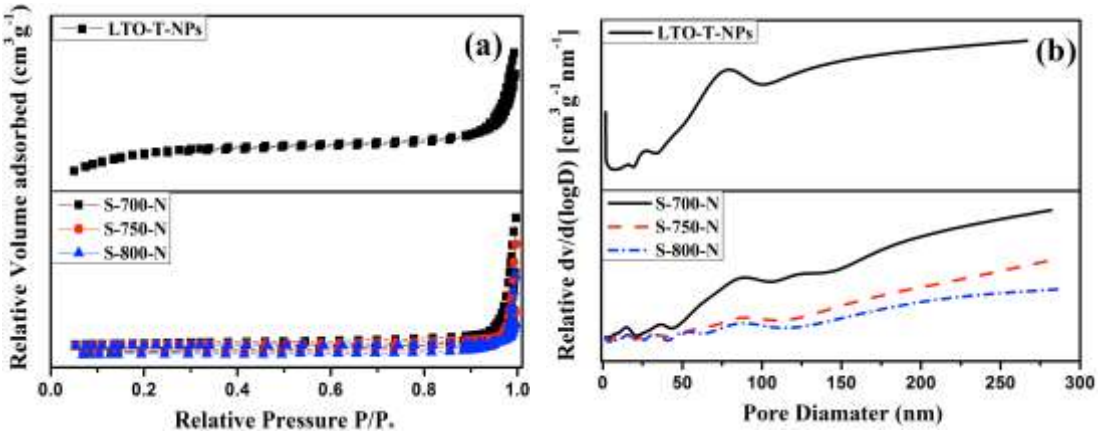

Figure 4-5. a) Nitrogen-adsorption–desorption isotherms and b) pore-size distribution curves of as-prepared LTO NPs, and corresponding samples calcined under nitrogen atmosphere at 700, 750, and 800 °C, respectively. All the samples were calcined for 2 h.

of samples S-700-N, S-750-N, and S-800-N were studied by X-ray photoelectron spectroscopy (XPS). As shown in Figure 4-6, all three samples exhibit two clear peaks at binding energies of 463.4, 458.0; 463.6, 458.5; and 463.6, 458.3 eV in the Ti 2p high-resolution spectra, respectively (error is ±0.26 eV). All these data correspond well with the Ti $2p_{3/2}$ and Ti $2p_{1/2}$ peaks of Ti^{4+}.[32-36] Furthermore, in addition to these peaks, there is another peak existing at the binding energies of 465.5, 457.4, and 457.3 eV for these three samples. These extra peaks appear 1.7 eV to the right of the main $2p_{3/2}$ peak, which can be assigned to the Ti^{3+} species according to references.[37,38] The presence of Ti^{3+} suggests that oxygen vacancies exist in the nitrogen-treated samples when considering the charge balance principle. This is consistent with the creation of defects on the surface after calcination under nitrogen atmosphere. In addition, the intensity of Ti^{3+} peaks becomes higher with increased calcination temperature. This result clearly indicates that nitrogen calcination under different

temperatures significantly influences the surface chemistry of the samples, resulting in different Li^+ storage performances that will be discussed in the next section.

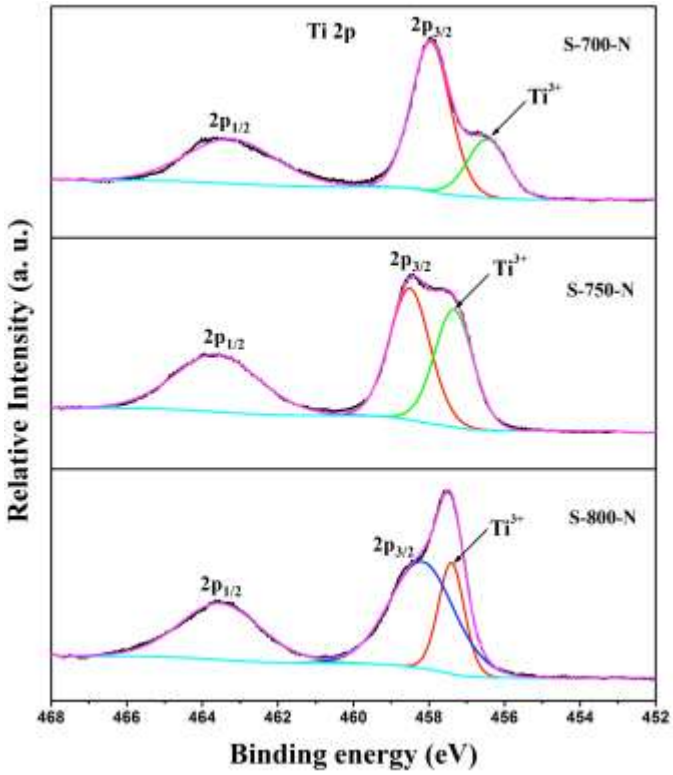

Figure 4-6. XPS spectra of the as-prepared LTO NPs calcined under nitrogen atmosphere at 700, 750, and 800 °C, respectively. All the samples were calcined for 2 h.

2.2 Electrochemical performance

To study the performance of LTO-T composites as lithium-ion storage electrodes, the lithium-ion insertion/extraction properties of the S-700-N, S-750-N, and S-800-N electrodes were characterized by galvanostatic discharge/charge measurements at both room temperature and 55 °C for 50 cycles. Figure 4-7a shows cyclic performance profiles of these samples during the 50-cycle test at room temperature, with different current densities of 30 mA g^{-1}, 150 mA g^{-1}, and 500 mA g^{-1}. As shown in this plot, at the current density of 30 mA g^{-1}, S-750-N-R (R denotes that the sample

was tested at room temperature) shows a capacity of 212 mAh g^{-1} after an initial degradation, which is higher than the theoretical capacity of $Li_4Ti_5O_{12}$ (175 mAh g^{-1}), owing to capacity contribution from rutile-TiO_2 (336 mAh g^{-1}). It is also higher than those of S-700-N-R (138 mAh g^{-1}) and S-800-N-R (157 mAh g^{-1}). At a high current density of 500 mAg^{-1}, S-750-N-R can still deliver a capacity of 117 mAh g^{-1}, while the S-700-N-R and S-800-N-R only deliver capacities of 73 and 78 mAh g^{-1}, respectively. After 50 cycles, S-750-N-R exhibits a capacity of 187 mAh g^{-1}, which is much higher than those of the other two samples (S-700-N-R, 127 mAh g^{-1}; S-800-N-R, 141 mAh g^{-1}). All the mentioned data are listed in Table I, as shown below. Above results indicate that samples composed of two phases (rutile-TiO_2 and LTO) (S-750, S-800) exhibit better performance than those composed of three phases (anatase-TiO_2, rutile-TiO_2, and $Li_4Ti_5O_{12}$) (S-700). This can be explained by the presence of the extra anatase phase, which contributes less capacity improvement than rutile phase to the LTO composites.[22,23] The outstanding performance of the S-750 samples could be attributed to two factors: 1) A well-known theory is that electronic transport properties can be tuned by interfacial design and by varying the spacing of interfaces down to the nanoscale regime, in which grain boundaries apparently act as channels to allow Li^+ to enter the particles. Therefore, lithium ions can reversibly react with atoms at and within the grain boundaries.[23,39,40] Compared with S-800-N, S-750-N possesses a higher specific surface area, which may provide more grain boundary interface for the reaction of Li^+ ion insertion/extraction, resulting in higher capacity; 2) As the temperature increased, the amount of rutile phase, which has

higher capacity than LTO, decreased in the final composites. Therefore, the S-750 sample has more rutile phase than the S-800 sample, which also accounts for its higher capacity.

Similar to measurements at room temperature, the performances of the samples at 55 °C are shown in Figure 4-7b. As shown in this figure, S-750-N-E (E denotes that the sample was tested at 55 °C) delivers capacities of 209, 170, 141 mAh g^{-1} at the three different current densities, which are higher than the other two samples. After 50 cycles at different current densities, the capacities for these three samples scale as: S-750-N-E > S-800-N-E > S-700-N-E (detailed data is shown in Table I). This result indicates that nitrogen-treated samples display higher capacities at the elevated temperature (55 °C) than at room temperature. Furthermore, the rate performances of these nitrogen-treated samples are also improved at 55 °C, compared to the results at room temperature (Figure 4-7a). As shown in Figure 4-7b, compared to the capacities of 185, 209, and 182 mAh g^{-1} at the current density of 30 mA g^{-1}, S-700-N-E, S-750-N-E, and S-800-N-E still have capacities of 82 mAh g^{-1}, 141 mAh g^{-1}, and 98 mAh g^{-1} at the current density of 500 mA g^{-1}. The capacity losses are apparently lower than those of the corresponding samples tested at room temperature. This enhancing effect on the rate performance of tests at elevated temperatures can be attributed to the accelerated diffusion of lithium ions, which will be explained in more detail.

To further study the electrochemical performance of LTO-T composites in Li-ion batteries, sample S-750-N, which had the best performance of these three samples,

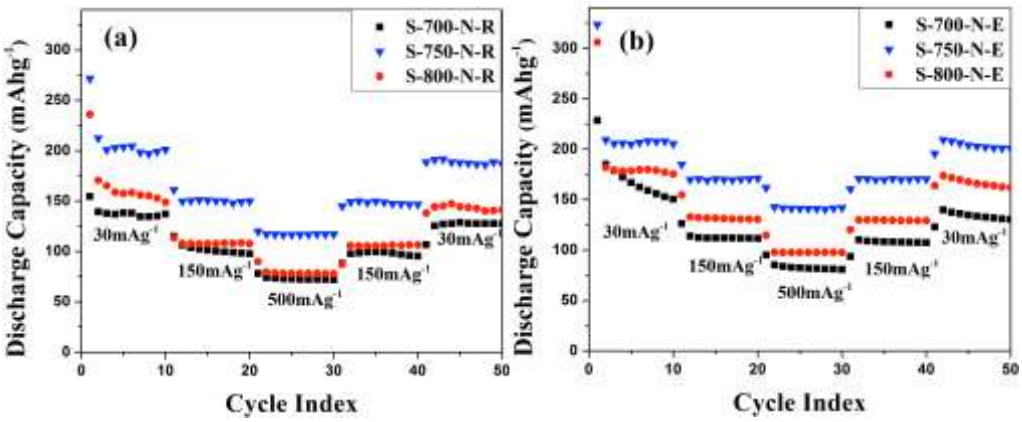

Figure 4-7. Discharge capacity vs. cycle number of S-700-N, S-750-N, and S-800-N cycled at different current densities a) at room temperature and b) the elevated temperature of 55 °C.

Table I. Discharge Capacities of LTO-T Composites at 25 and 55 °C [mAh g^{-1}]

	S-700-N-R	S-700-N-E	S-750-N-R	S-750-N-E	S-800-N-R	S-800-N-E
*30 mA g^{-1}	138	185	212	209	157	182
150 mA g^{-1}	95	107	147	170	106	129
500 mA g^{-1}	73	82	117	141	78	98

* Discharge capacities of the 2nd cycle at the current density of 30 mA g^{-1}

was chosen for additional study. Figure 4-8a displays its discharge/charge voltage profiles in the initial and final three cycles at the current density of 30 mA g^{-1}, tested at room temperature. It shows a long flat voltage plateau at the potential of ~1.55 V vs. Li^+/Li, which can be assigned to the reversible conversion reaction of $Li_{4+x}Ti_5O_{12}$ to $Li_4Ti_5O_{12}$ similar to reported LTO.[7] It is observed that the initial discharge capacity of S-750-N-R is 271 mAh g^{-1}. In the 2nd cycle, there is an obvious degradation due to irreversible electrochemical decomposition of the electrolyte or impurity phase over the LTO/TiO_2 surface.[23,41] After this capacity degradation, S-750-N-R shows reasonable capacity fading in the following cycles. Finally, S-750-N-R delivers a

capacity of 187 mAh g^{-1} at the 50th cycle, which is still higher than the theoretical capacity of LTO. The discharge/charge voltage profiles of S-750-N at 55 °C are also shown in Figure 4-8b. Similar to the room temperature test, it experiences a remarkable discharge capacity degradation from the initial cycle to the 2nd cycle. However, very little capacity fading can be observed in the following cycles. As shown in this figure, the capacity curves of the 2-3th and 48-50th cycles almost overlap. It delivers a capacity of 201 mAh g^{-1} after 50 cycles, which is comparable to the capacity of mesoporous TiO_2 reported recently.[42] Furthermore, capacities of 186 and 201 mAh g^{-1} at room temperature and 55 °C are both higher than those of nanoporous LTO,[43] carbon-coated LTO composites,[23] and TiN-coated LTO[18] reported in other recent papers. Figure 4-8c compares the cyclic performance of sample S-750-N at both room temperature and 55 °C with different current densities. After initial degradation, the capacity of S-750-N-E only has a minor decrease from 209 mAh g^{-1} to 201 mAh g^{-1}, and the capacity retention rate is 96.1%. In comparison, S-750-N-R has a decrease from 212 mAh g^{-1} to 187 mAh g^{-1} with a capacity retention rate of 88.2%. Additionally, S-750-N-E kept 70% of its capacity when tested at a higher current density of 500 mA g^{-1}, while S-750-N-R only kept 62.6% of its capacity when tested under the same condition. The better performance of S-750-N-E than that of S-750-N-R can be attributed to several reasons.

Samples calcined under nitrogen atmosphere generated a thin layer of surface defects, which results in an extra, less active coating on the electrode by reducing the number of available Ti^{4+} that can transform to Ti^{3+} (Figure 4-6). This less active layer

may reduce the diffusion rate of lithium ions into the electrode, causing samples to exhibit relatively low rate performance at room temperature. While being tested at 55 °C, the elevated temperature will enhance the insertion/extraction rate of lithium ions into the electrode,[44] compensating for the loss from less active layers. Furthermore, this less active layer also acts as a protective layer between the liquid electrolyte and electrode surface, which obviously alleviates the excessive electrode and electrolyte reactions at elevated temperatures.[45] Together with the above effects, we can conclude that sample S-750-N exhibits both higher capacity and better rate performance at 55 °C than at room temperature.

Generally, capacity degradation can be more readily observed when tested using a small current density.[46,47] Herein, to investigate the cycle stability, sample S-750-N was also tested using a small constant current density of 30 mA g^{-1} for 50 cycles both at room temperature and 55 °C. As shown in Figure 4-8d, S-750-N delivered a capacity of 345 mAh g^{-1} and 287 mAh g^{-1} in the initial cycle at room temperature and 55 °C, respectively. After 50 cycles, the discharge capacity for S-750-N was measured to be 184 and 197 mAh g^{-1} at room temperature and 55 °C, respectively. The capacity losses were 15.6% and 6.2% after the initial capacity fading. The results indicated that S-750-N has good cyclic stability under these operating conditions. In addition, it was remarkably stable when tested at the elevated temperature of 55 °C. The morphology of S-750-N after cycling at 55 °C was also investigated, the results showed that there were no much morphology difference between the samples before

and after cycling. The nanoporous structure can be also observed in the cycled $Li_4Ti_5O_{12}$-TiO_2 electrode (Figure 4-9).

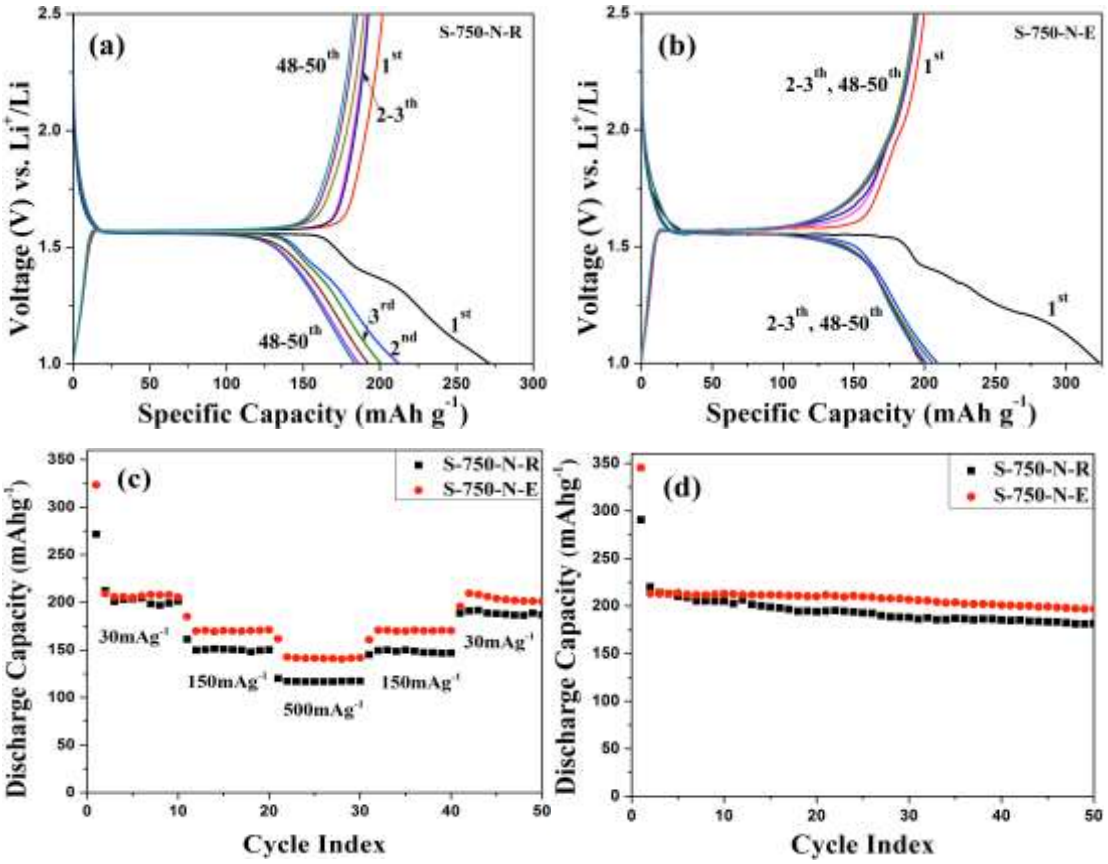

Figure 4-8. Galvanostatic discharge/charge voltage profiles of S-750-N cycled in the initial and final 3 cycles at different current densities at a) room temperature and b) 55 °C; c) discharge capacity vs. cycle number of S-750-N cycled at different current densities at room temperature and 55 °C; d) cyclic performance of S-70-N at the current density of 30 mA g^{-1} at both room temperature and 55 °C.

To further investigate the electrochemical behavior of the S-750-N electrode, cyclic voltammetry (CV) in the potential range of 1.0-2.5 V vs. Li^+/Li at a scan rate of 0.1 mVs^{-1} was performed (Figure 4-10a). The clear cathodic/anodic peaks around 1.55 V can be attributed to the redox reaction of Ti^{4+}/Ti^{3+}, respectively, which is associated with lithium insertion/extraction in the spinel $Li_4Ti_5O_{12}$ lattice.[48] This result agrees

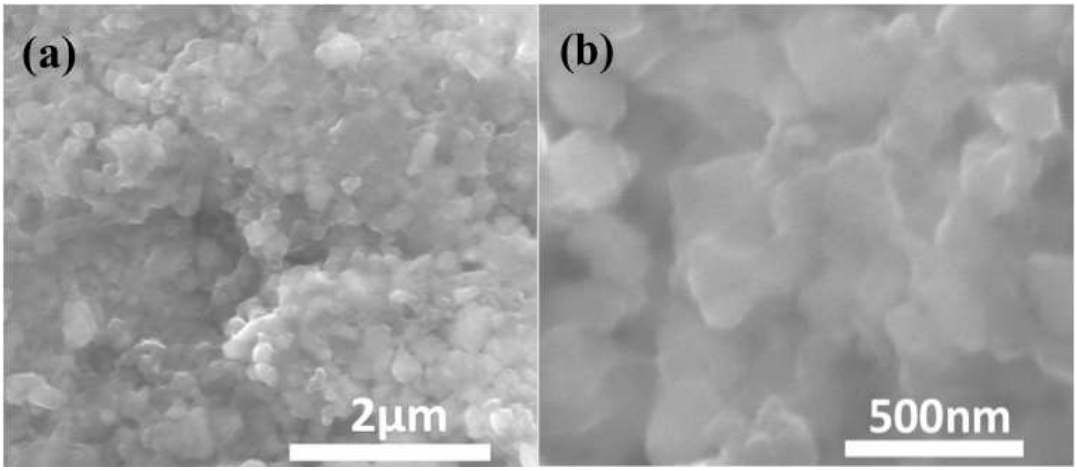

Figure 4-9. Low and high-magnification SEM images of S-750-N after cycling at 55 °C.

well with the voltage plateaus in the discharge/charge voltage profiles (Figure 4-8a and 4-8b). In addition, electrochemical impedance spectroscopy (EIS) was used to probe the charge transfer resistance of S-750-N before and after electrochemical cyclic tests. As shown in the set of Figure 4-10b, in the equivalent circuit, R_s, R_f, and R_{ct} are ohmic resistance (total resistance of the electrolyte, separator, and electrical contacts), film resistance, and charge transfer resistance respectively; Z_w represents the Warburg impedance of Li ion diffusion into active materials. CPE is the constant phase-angle element, symbolizing double layer capacitance. The system resistances of R_s and R_f are similar for samples measured at room temperature and 55 °C because of the fact that both materials are pasted directly on the substrates used as current collectors, which ensures good electrical conductivity in the electrodes. Before cycling, the charge transfer resistance R_{ct} is 26 Ω. After cycling, sample S-750-N-E (35 Ω) has an almost equal charge transfer resistance compared with sample S-750-N-R (38 Ω) measured at room temperature. Compared to the samples S-700-N and S-800-N, for sample S-750-N, the charge transfer resistance R_{ct} had only a little

increase after testing (Figure 4-10c), which agrees well with the result of discharge capacities for these three samples (Figure 4-7). The increased R_{ct} is due to the interface formation between the electrode and electrolyte during cycling. In addition, the almost equal resistances of R_{ct} at room temperature and 55 °C suggest that the sample's charge transfer resistance did not increase more when tested at elevated temperatures than at room temperature. The reason can be ascribed to the existence of surface defects that acted as a protective layer between the liquid electrolyte and electrode surface, which inhibited the charge transfer resistance increase resulting from the excessive interface formed during cycling at elevated temperatures.

Based on the above results, the much improved electrochemical performance of the nitrogen-treated LTO-T nanoporous composites can be attributed to the following: 1) The nanoporous morphology offers the possibility to benefit from small transport lengths for both Li^+ ions and electrons diffusion; 2) A possible mechanism for lithium storage is that Li^+ ions are stored by reaction with the grain boundary phase in polycrystalline materials[36] or by reaction with the liquid electrolyte at the solid/liquid interface.[49] Therefore, an appropriate composition of rutile-TiO_2 and LTO in the composites (S-750-N) will increase the relatively low capacity of pure LTO by offering more grain boundary interfaces for Li^+ ion insertion/extraction reactions; 3) The nitrogen calcination treatment created surface defects that acted as a protective layer when tested at room temperature and the elevated temperature of 55 °C, which enhanced the performance of electrodes through stabilizing the interface during

cycling. All these reasons explain why nitrogen-treated dual phase $Li_4Ti_5O_{12}$-TiO_2 (S-750-N) exhibited superior electrochemical performance.

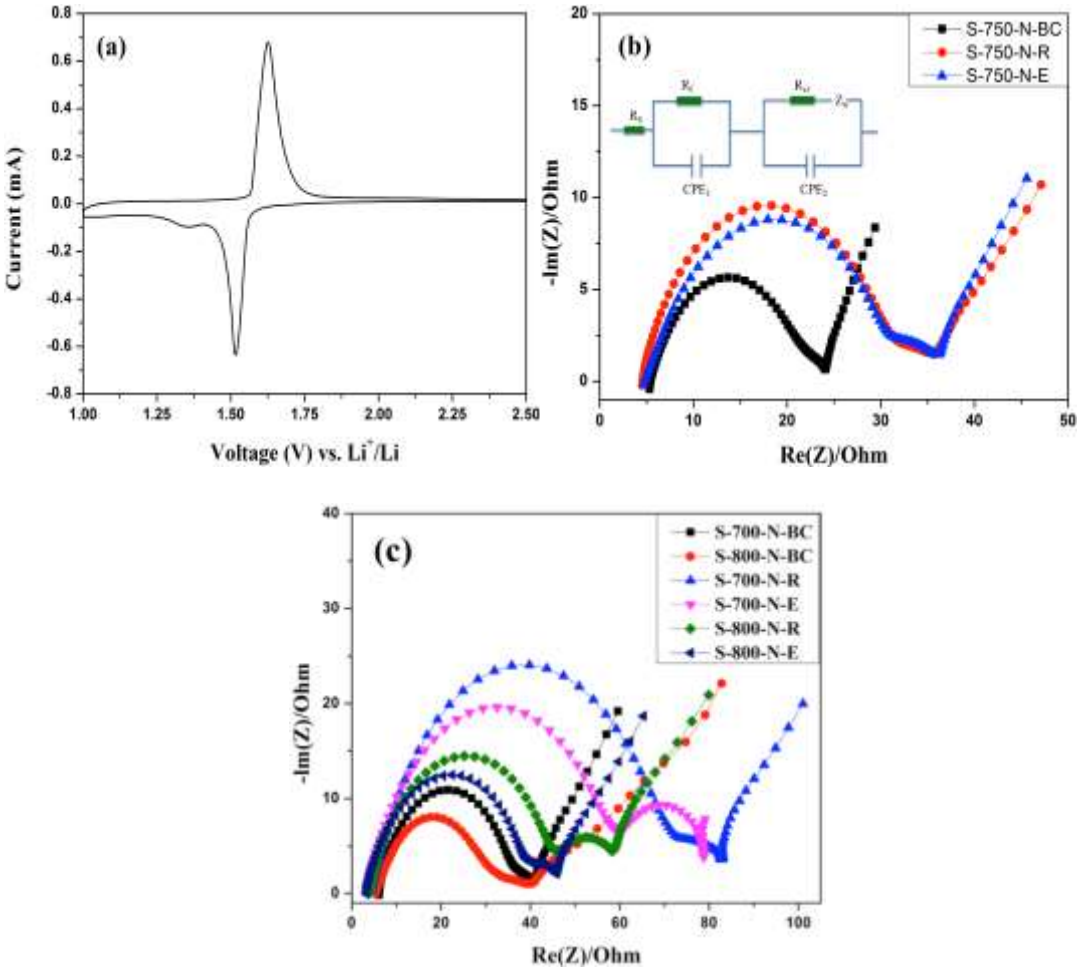

Figure 4-10. a) Cyclic voltammetry curve at a scan rate of 0.1 mV s^{-1} for S-750-N; b) Nyquist plots of S-750-N before cycling and after cycling at room temperature and 55 °C (the inset shows the equivalent circuit used for fitting the experimental EIS data); c) Nyquist plots of S-700-N and S-800-N before cycling (BC) and after cycling at room temperature (R) and 55 °C (E).

3. Conclusion

In summary, a simple and effective strategy was developed centered on a solution-based method and nitrogen treatment process to obtain LTO-TiO_2 nanoporous composites. Compared to the samples calcined at 700 °C and 800 °C,

LTO-T-NPs precursor, calcined at 750 °C, exhibited high capacity and improved cyclic stability and rate capability when used as lithium ion battery electrodes at both room temperature and the elevated temperature of 55 °C. The improved electrochemical performance can be attributed to the synergistic effects of nanostructure, the composition of phases in the product, and surface defects derived from nitrogen treatment. These effects contribute to enhancing structural/interface stability and improving lithium storage capacity by offering more grain boundary interface during cycling. This proposed synthesis and calcination strategy will provide a novel and feasible method for the synthesis of metal oxide composites, and also open up new avenues to the development of high-performance nanostructures in electrochemical energy storage and relevant fields.

C. Ni-Doped $Li_4Ti_5O_{12}$-TiO_2 Composites as Anode Materials for LIBs

1. Experimental procedure

Ni-doped $Li_4Ti_5O_{12}$-TiO_2 nanoporous composites have been synthesized in two steps. First, $Li_4Ti_5O_{12}$-TiO_2 (LTO-T) nanoporous precursors were synthesized by a one-step procedure at room temperature. Typically, 1.3473 g (32.1 mM) of $LiOH{\cdot}H_2O$ (ACS, Alfa Aesar) and 2.1632 mL of hydrogen peroxide (ACS, 30.0-32.0 %, Fisher Chemical) were mixed in 20 mL deionized (DI) water at ambient temperature. The solution was stirred for 10 min using a magnetic stirrer. Then, 2 mL (6.6 mM) of titanium (IV) isopropoxide (TIP, 97%, Sigma-Aldrich) was added drop-wise to the solution without using any surfactant. The light yellow suspension

was kept static and aging for 1 h before the precipitates were removed and washed with DI water three times. The obtained product was dried in air at 40 °C. Then, 0.19 g of the as-prepared product was dispersed in 100 mL of nickel chloride (98%, Anhydrous, Alfa Aesar) solution (0.008 mM) under constant stirring for 1 h. After that, it was washed three times by DI water to remove excess ions and dried in air at 40 °C. Finally, the obtained precursors were calcined at 750 °C for 2 h. For comparison, LTO-T-NPs powders without Ni-doping were also calcined under the same conditions. Within this study, the samples are designated as LTO-P (precursor), LTO-T-Ni (after Ni ion-exchange process and calcination), and LTO-T (after calcination without Ni ion doping), respectively. Structural characterization and electrochemical evaluation were similar to the previous chapters.

2. Results and discussion

2.1 Structural and morphological analysis

Figure 4-11a shows a typical scanning electron microscope (SEM) image of the precursor (LTO-P) for the $Li_4Ti_5O_{12}$ nanoporous composite prepared at room temperature. The SEM image clearly shows that the as-synthesized structure was composed of amorphous interconnected nanoparticles, which had diameters of around 100 nm. After calcination, LTO composites with and without Ni ion doping (LTO-T, LTO-T-Ni) exhibited no fundamental morphology difference in their SEM images (Figure 4-11b and 4-11c). In addition, they both showed some sintering neck between particles compared with the precursor. While the ion-exchange process had negligible influence on the morphology of prepared samples, it did produce obvious differences

in crystallinity, chemical bonding, and surface area as determined by XRD patterns, FT-IR spectra, and nitrogen adsorption isotherms (to be discussed later).

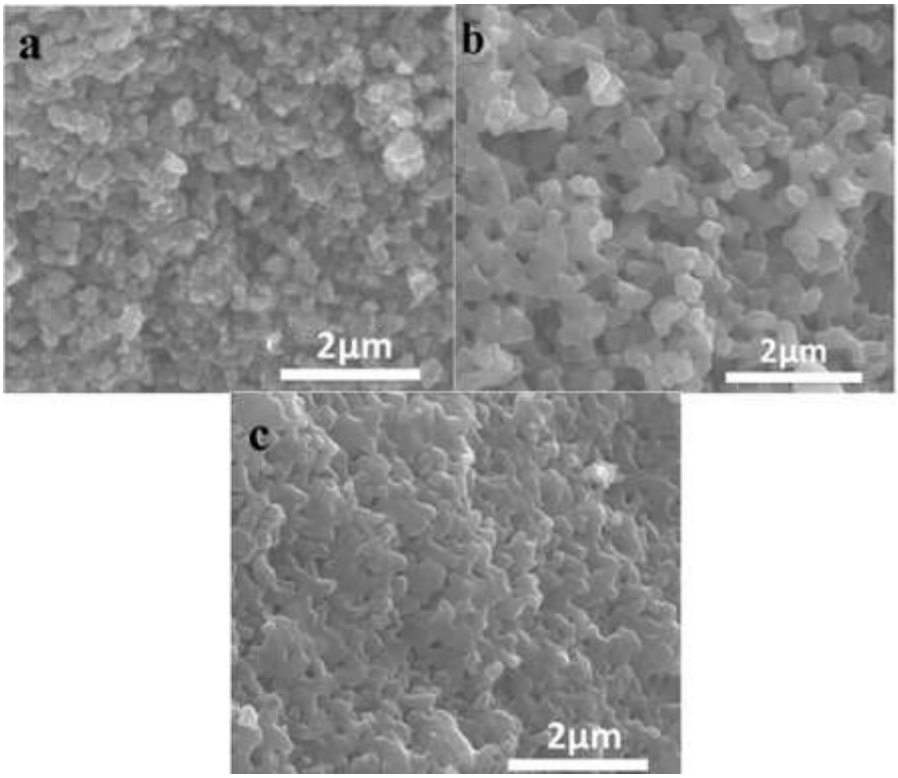

Figure 4-11. SEM images of LTO nanoporous structures obtained after different processes: a) LTO-P fabricated at room temperature, b) LTO-T composite calcined at 750 °C for 2 h, and c) LTO-T composite doped with nickel ions and calcined at 750 °C for 2 h.

The effect of Ni ion doping on the crystallinity evolution of LTO composites was studied by X-ray diffraction (XRD) and the patterns are shown in Figure 4-12. After calcination at 750 °C for 2 h, both samples exhibited the spinel phase $Li_4Ti_5O_{12}$ (PDF No. 00-049-0207, space group $Fd\bar{3}m(227)$, a= 8.36 Å) and rutile-TiO_2 (PDF No. 03-065-0191) (Fig. 2). In addition, compared with the undoped sample, the Ni-doped sample showed additional diffraction peaks of anatase-TiO_2 (PDF No. 01-071-1168), which is a low-temperature phase that transforms into rutile-TiO_2 at a higher temperature.

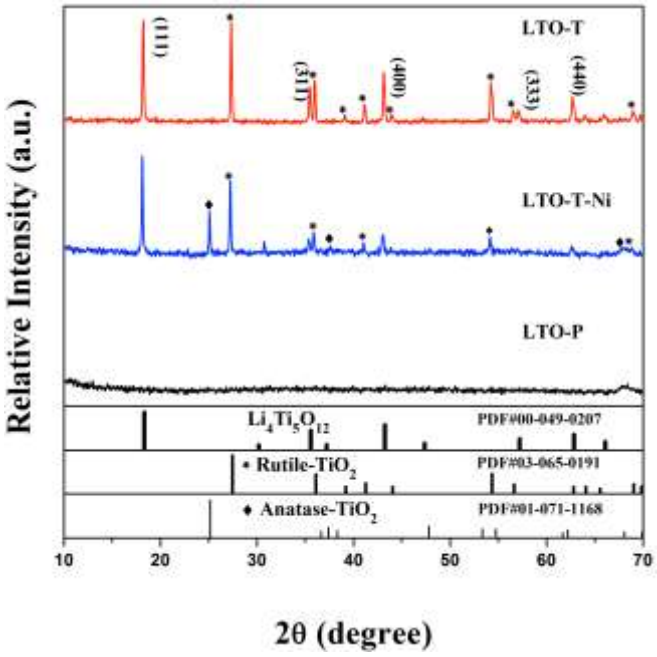

Figure 4-12. XRD patterns of as-prepared LTO composites LTO-P, and corresponding samples doped with and without nickel ions calcined at 750 °C for 2 h.

This result indicates that nickel ions inhibit the phase transition from anatase to rutile. This inhibition effect has widely been observed in our previous work. The diffraction peaks in the Ni-doped sample shifted slightly towards a lower diffraction angle compared to peaks in the patterns of the undoped samples, indicating that the incorporation of nickel ions increased lattice parameters, which may be favorable for reversible lithium ion insertion.[50,51] The LTO-T-Ni had a larger lattice value of a (8.2237 ± 0.0015 Å) for LTO than that of undoped sample LTO-T (a = 8.2209 ± 0.0013 Å). In addition, the crystallite size of LTO-T-Ni (24.3 nm) and LTO-T (26.6 nm) were also different, which would affect their specific surface area after calcination (to be discussed later).

To investigate the doping effect of the ion-exchange process, surface element compositions of LTO-T-Ni was studied by XPS. As shown in Figure 4-13, two distinct peaks at binding energies of 855.6 and 873.0 eV are observed in the Ni 2p

high-resolution spectrum, which correspond well to the Ni 2p3/2 and Ni 2p1/2 peaks of Ni^{2+}.[52,53] In addition, two satellite peaks at 861.6 and 879.1 eV can be attributed to 2p3/2 sat and 2p1/2 sat of NiO.[54] This suggests that the doped nickel ions' oxidation state did not change after calcination. The concentration of doped Ni was further confirmed by inductively coupled plasma mass spectrometry (ICP-MS). The weight ratio of Ni in LTO-T-Ni was approximately 0.36%.

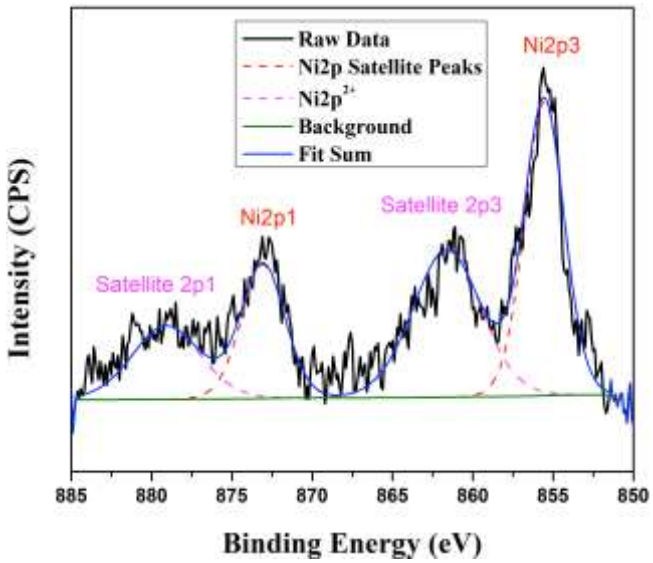

Figure 4-13 XPS spectra of as-prepared LTO composites doped with nickel ions calcined at 750 °C for 2 h.

In addition, the doping effect on LTO composites can also be observed in FT-IR spectra. As shown in Figure 4-14, the FT-IR spectra of the LTO-T and LTO-T-Ni exhibited similar characteristics after calcination. The absorption peak at ~ 3403 cm^{-1} was ascribed to the stretching vibration of O-H groups,[55] while the absorption bands at ~ 1638 cm^{-1} were caused by the bending vibration of coordinated H_2O.[56] The small peaks at ~ 2362 and 2331 cm^{-1} were attributed to the stretching and bending vibration of C-O group,[57] which may be derived from the gas-phase CO_2 in the sample compartment of the IR spectrometer.

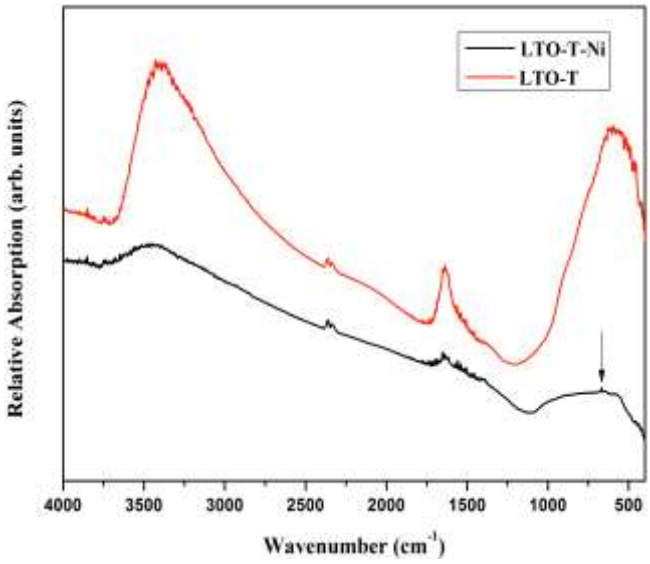

Figure 4-14. FT-IR spectra of LTO composites doped with and without nickel ions calcined at 750 °C for 2 h. The arrow shows the extra peak existing at ~668 cm^{-1} in LTO-T-Ni.

However, the peak in LTO-T at ~595 cm^{-1} was likely due to the vibration of Ti-O bond,[58] while the similar peak in the LTO-T-Ni was located at ~530 cm^{-1}. The decrease in FT-IR frequency of Ti-O for the Ni-doped sample may be due to the smaller particle size,[59] which agrees well with the BET result to be discussed later. In addition, there was an extra peak existing at ~ 668 cm^{-1} in LTO-T-Ni, which can be ascribed to the doped Ni ions in the composites as this peak was absent in the undoped sample.[60]

Ion doping also affects the specific surface area of LTO composites after calcination. Here, we studied the surface area of different samples before and after calcination by using nitrogen adsorption-desorption measurements. Figure 4-15a shows the nitrogen adsorption-desorption isotherm curves of LTO-P, LTO-T, and LTO-T-Ni. The specific surface areas of these three samples were calculated using the

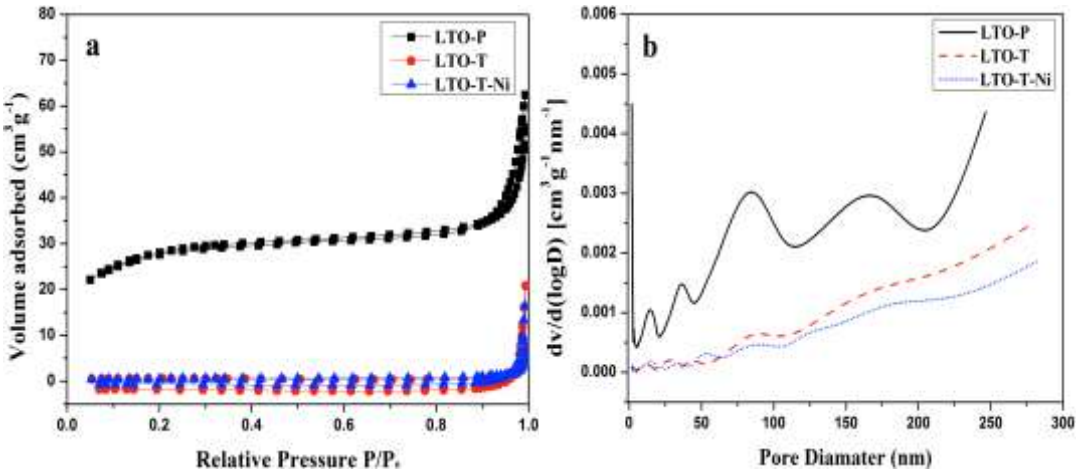

Figure 4-15. a) Nitrogen-adsorption–desorption isotherms and b) pore-size distribution curves of as-prepared LTO nanocomposite precursor, and corresponding samples doped with and without nickel ions after calcination at 750 °C for 2 h.

Barrett-Joyner-Halenda (BJH) method to be 71.6 m^2 g^{-1}, 1.6 m^2 g^{-1}, and 2.3 m^2 g^{-1}, respectively. All these three samples had type I isotherm curves and exhibited no adsorption hysteresis.[30] Figure 4-15b shows the corresponding pore-size distribution curves of these samples. It can be observed that pores with sizes of less than 100 nm decreased noticeably after calcination, which is consistent with the theory that thermal treatment decreases the specific surface area of materials because of particle growth and agglomeration.[32] However, LTO-T-Ni still exhibited more pores (< 50 nm) after calcination, which agrees well with the result that LTO-T-Ni possessed a larger specific surface area than LTO-T after calcination. The reason could be attributed to the doped ions that act as nucleation barriers to inhibit the crystallization and phase transition process during calcination. As a result, doped LTO-T-Ni has extra low-temperature phase (anatase) and smaller grains compared with undoped LTO-T. Smaller grain sizes will generally result in smaller particle sizes or the same particle

size with larger surface roughness. In other words, a smaller grain size will lead to a larger surface area.[7]

2.2 Electrochemical performance

The electrochemical performance of the prepared $Li_4Ti_5O_{12}$ (LTO) composites with and without Ni doping was systematically investigated as lithium-ion storage electrodes. Lithium-ion insertion/extraction properties of the LTO-T-Ni and LTO-T electrodes were characterized by galvanostatic discharge/charge measurements at both room temperature and 55 °C. Figure 4-16a shows the discharge/charge voltage profiles of these two samples at different current densities in the voltage range of 1.0-2.5 V vs Li^+/Li tested at room temperature. As shown in this Figure, both samples exhibited a long flat voltage plateau around the potential of ~1.55 V at different current densities, which is similar to reported LTO.[45] It is observed that the discharge capacities of LTO-T-Ni-R (R denotes that the sample was tested at room temperature) and LTO-T-R were 195 mAh g^{-1} and 184 mAh g^{-1} at the current density of 30 mA g^{-1} (higher than the theoretical capacity of $Li_4Ti_5O_{12}$ (175 mAh g^{-1}), owing to capacity contribution from rutile-TiO_2 (336 mAh g^{-1}) whose molar ratio was estimated to be around 19.43 % according to ICP results, and could retain a capacity of 110-120 mAh g^{-1} at the higher current density of 500 mA g^{-1}. The result demonstrates the high-performance of LTO-T composites as anode materials for LIBs. The higher discharge capacity of Ni-doped LTO-T composite could be attributed to the Ni ions, which improved the interface stability during cycling and increased the lattice parameters of the crystal structure for easier Li ion insertion/extraction. Similar to

measurements at room temperature, the discharge/charge voltage profiles of the samples at 55 °C are shown in Figure 4-16b. As shown in this plot, LTO-T composites with and without Ni doping had similar flat plateaus, similar to what is observed at room temperature (Fig. 4-16a). LTO-T-Ni-E (E denotes that the sample was tested at 55 °C) exhibited a discharge capacity of 196 mAh g^{-1} at the current density of 30 mA g^{-1}, which was higher than that of LTO-T tested under the same condition (175 mAh g^{-1}). At the high current density of 500 mA g^{-1}, LTO-T-Ni-E could still deliver a higher capacity than LTO-T-E (114, 100 mAh g^{-1}). Compared with the results obtained at room temperature (Figure 4-16a), it can be found that the sample without Ni doping had notable capacity degradation when tested at the elevated temperature of 55 °C. The reason can be ascribed to the excessive electrode and electrolyte reaction at elevated temperatures.[41] However, the sample doped with Ni ions not only showed little capacity drop when tested at 55 °C, but also exhibited better rate performance compared with the undoped one. Figure 4-16c shows the cyclic performance profile of these two samples in a 50-cycle test at different current densities of 30 mA g^{-1}, 150 mA g^{-1}, and 500 mA g^{-1} in the potential window of 1-2.5 V at both room temperature and 55 °C. As shown in this Figure, the Ni-doped sample exhibited higher specific capacity and better rate performance than the undoped one especially when tested at the elevated temperature of 55 °C. After 50 cycles at different current densities, LTO-T-Ni delivered a capacity of 186 and 191 mAh g^{-1} at 55 °C and room temperature, respectively. However, LTO-T only exhibited a corresponding capacity of 176 and 166 mAh g^{-1}. Above results suggest that Ni doping

will enhance the performance of the LTO-T composites, and also has notable stability effects on the electrode at elevated temperatures.

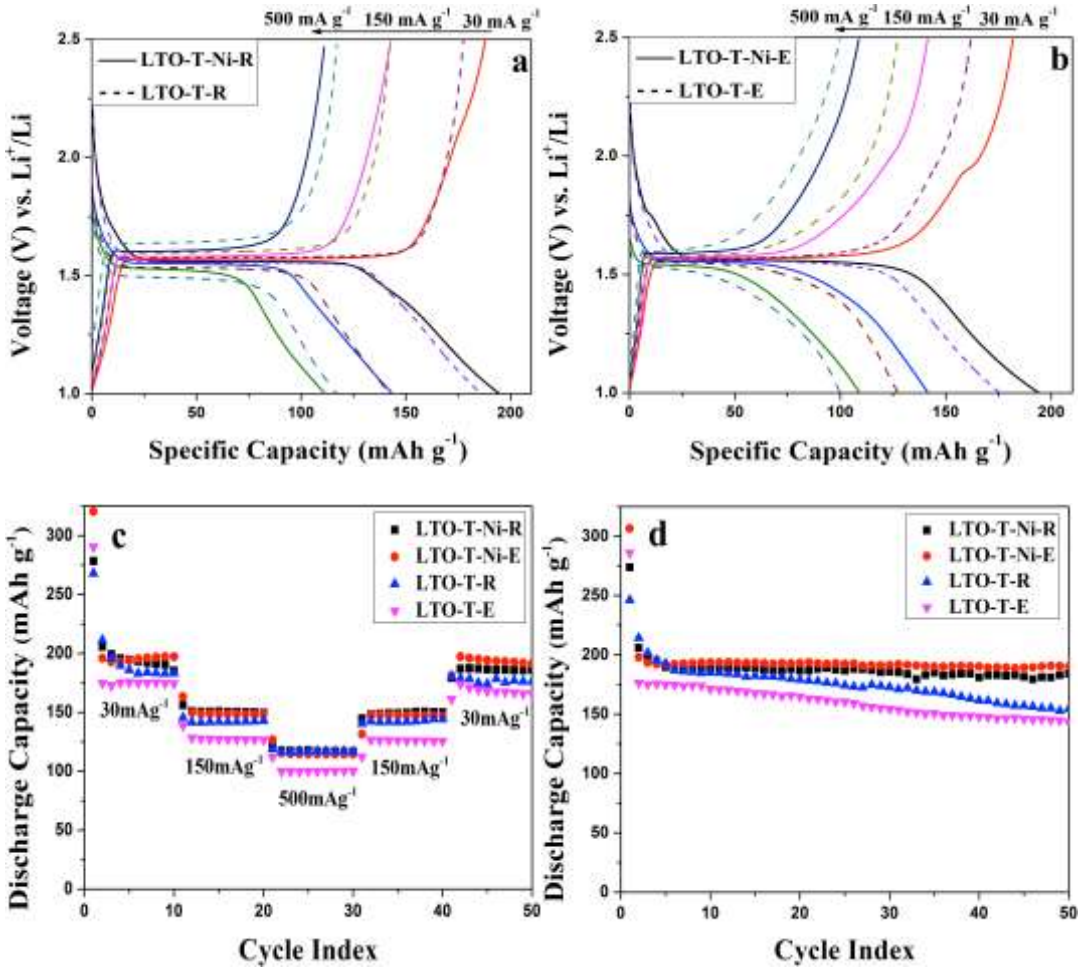

Figure 4-16. Electrochemical performance of LTO-T-Ni and LTO-T: galvanostatic discharge/charge voltage profiles cycled at different current densities at room a) and elevated temperatures of 55 °C b); c) discharge capacity vs. cycle number of LTO-T-Ni and LTO-T cycled at different current densities of 30, 150, and 500 mA g-1 at both room temperature and 55 °C; d) cyclic performance of LTO-T-Ni and LTO-T at the current density of 30 mA g^{-1} at the same temperatures of c).

To further investigate the effect of Ni ion doping on the electrode property of cyclic stability, above two samples were tested using a small constant current density of 30 mA g^{-1} for 50 cycles both at room temperature and 55 °C. As shown in Figure 4-16d, obvious capacity degradation can be observed between the initial and subsequent

cycles in all tests, which can be ascribed to side reactions during electrode/electrolyte interface formation or impurity phase over the LTO/TiO_2 surface.[23] After this degradation, samples LTO-T-R and LTO-T-E showed noticeable capacity fading in the following cycles. Finally, they delivered capacities of 154 mAh g^{-1} and 144 mAh g^{-1} at the 50th cycle for the tests at room temperature and 55 °C, respectively. The corresponding capacity retention rates were 72% and 81%. In comparison, samples LTO-T-Ni-R and LTO-T-Ni-E only experienced minor decrease after the initial degradation: LTO-T-Ni-R delivered a capacity of 205 mAh g^{-1} in the second cycle and decreased to 184 mAh g^{-1} in the 50th cycle, with a capacity retention rate of 90%. LTO-T-Ni-E delivered a capacity of 198 mAh g^{-1} in the second cycle and decreased to 190 mAh g^{-1}, with a capacity retention rate of 96%. The results indicate that Ni-doped LTO nanocomposites have good cyclic stability under these operating conditions. In addition, they were remarkably stable when tested at the elevated temperature of 55 °C. These capacities are higher than those of carbon-coated LTO composites,[23] La-doped LTO,[17] and mesoporous Au/LTO spheres[61] reported in other papers. In addition, these values are still higher than that of the LTO-TiO_2 (S-750-N) reported in part A, suggesting the strategy of doping together with nitrogen calcination is a better approach than either of them.

To clarify the effects of Ni ion doping on the electrochemical properties of LTO nanocomposites, electrochemical impedance spectroscopy (EIS) was used to probe the kinetic properties of samples LTO-T-Ni and LTO-T before and after cycling. As shown in Figure 4-17a, the equivalent circuit (Figure 4-17a inset): R_s, R_f, and R_{ct} are

ohmic resistance (total resistance of the electrolyte, separator and electrical contacts), film resistance, and charge transfer resistance respectively; Z_w represents the Warburg impedance of Li ion diffusion into active materials; CPE is the constant phase-angle element, symbolizing double layer capacitance. The system resistances of R_s and R_f are similar for LTO-T-Ni and LTO-T because of the fact that both materials are grown directly on the substrates that are used as current collectors, which ensures good electrical conductivity in the electrodes. Before cycling, the charge transfer resistance R_{ct} of LTO-T-Ni was 97 Ω. After cycling at room temperature and 55 °C, the charge transfer resistance decreased to 57 Ω and 51 Ω, respectively. However, for the undoped sample LTO-T, the charge transfer resistance was 88 Ω before cycling, and increased to 94 Ω and 109 Ω after cycling at room temperature and 55 °C, respectively (Figure 4-17b). Before cycling, the Ni-doped sample exhibited higher resistance than the undoped one, which can be ascribed to the formation of a more complicated electrode/electrolyte interface induced by ion doping. After electrochemical cycling, it showed lower R_{ct}, which fits well with its higher discharge capacity, better rate capability, and cyclic stability.

Based on the above results, the much improved electrochemical performance of the Ni-doped LTO nanoporous composites could be attributed to the following aspects: (1) an appropriate composition of TiO_2 and LTO in the composites increased the relatively low capacity of pure LTO by offering more grain boundary interfaces for Li^+ ion insertion/extraction reactions [36, 40, 41];[7,49,31] (2) the existence of Ni^{2+} ions induced an increased lattice parameters of the crystal structure, which made lithium

ions insertion into electrodes easier;[40] (3) Ni ions contributed to the formation of a more favorable electrode/electrolyte interface during cycling. This interface enhanced the performance of electrodes through increased conductivity (lower resistance and better rate performance) and improved interface stability. All these reasons explain why the Ni-doped sample LTO-T-Ni possessed better electrochemical performance than the undoped one LTO-T.

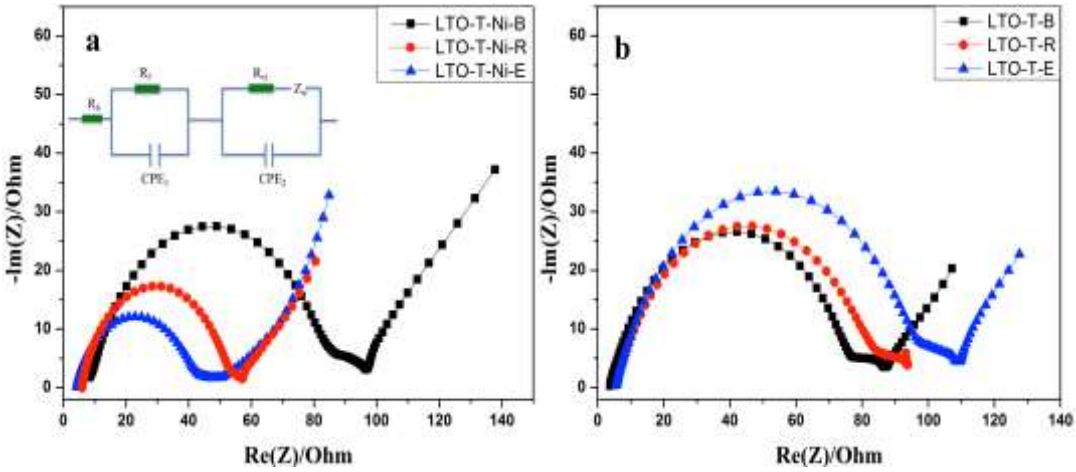

Figure 4-17. a) Nyquist plots of LTO-T-Ni before cycling (LTO-T-NiB) and after cycling at room temperature (LTO-T-Ni-R) and the elevated temperature of 55 °C (LTO-T-Ni-E). The inset shows the equivalent circuit used for fitting the experimental EIS data; b) Nyquist plots of LTO-T before cycling (LTO-T-B) and after cycling at room temperature (LTO-T-R) and the elevated temperature of 55 °C (LTO-T-E).

3. Conclusions

In summary, Ni-doped LTO nanoporous composites have been synthesized through a simple solution-based method and ion-exchange process at room temperature followed by calcination. Compared to undoped LTO-T composites, the Ni-doped sample exhibited high capacity, improved rate capability and excellent cyclic stability

when used as lithium ion battery electrodes tested at both room temperature and 55 °C. This improvement can be ascribed to the roles of nickel ions in improving the electrode/electrolyte interface stability, increasing lattice parameters, and reducing the charge transfer resistance during repeated lithium ion insertion. The simple surface doping process can be easily scaled up at room temperature, and requires only thermal treatment to obtain final products. The method presented here can also be adopted to synthesize other doped metal oxide composites, and will also open up new opportunities in the development of high performance materials used in lithium ion batteries and relevant fields.

References

[1] P.G. Bruce, B. Scrosati, and J.M. Tarascon, "Nanomaterials for Rechargeable Lithium Batteries," *Angew. Chem. Int. Ed.*, **47** [16] 2930-2946 (2008).

[2] W. Dreyer, J. Jamnik, C. Guhlke, R. Huth, J. Moskon, and M. Gaberscek, "The Thermodynamic Origin of Hysteresis in Insertion Batteries," *Nat. Mater.*, **9** [5] 448-453 (2010).

[3] D.W. Liu, B.B. Garcia, Q.F. Zhang, Q. Guo, Y.H. Zhong, S. Sepehri, and G. Z. Cao, "Mesoporous Hydrous Manganese Dioxide Nanowall Arrays with Large Lithium Ion Energy Storage Capacities," *Adv. Funct. Mater.*, **19** [7] 1015-1023 (2009).

[4] H.-G. Jung, M.W. Jang, J. Hassoun, Y.-K. Sun, and B. Scrosati, "A High-rate Long-life $Li_4Ti_5O_{12}/Li[Ni_{0.45}Co_{0.1}Mn_{1.45}]O_4$ Lithium-Ion Battery," *Nat. Commun.*, **2** 516-521 (2011).

[5] W.J.H. Borghols, M. Wagemaker, U. Lafont, E.M. Kelder, and F.M. Mulder, "Size Effects in the $Li_{4+x}Ti_5O_{12}$ Spinel," *J. Am. Chem. Soc.*, **131** [49] 17786-17792 (2009).

[6] L. Aldon, P. Kubiak, M. Womes, J. Jumas, J. Olivier-Fourcade, J. Tirado, J. Corredor, and C.P. Vicente, "Chemical and Electrochemical Li-insertion into the $Li_4Ti_5O_{12}$ Spinel," *Chem. Mater.*, **16** [26] 5721-5725 (2004).

[7] T. Ohzuku, A. Ueda, and N. Yamamoto, "Zero-Strain Insertion Material of $Li[Li_{1/3}Ti_{5/3}]O_4$ for Rechargeable Lithium Cells," *J. Electrochem. Soc.*, **142** [5] 1431-1435 (1995).

[8] K. Ariyoshi, R. Yamato, and T. Ohzuku, "Zero-Strain Insertion Mechanism of $Li[Li_{1/3}Ti_{5/3}]O_4$ for Advanced Lithium-ion (Shuttlecock) Batteries," *Electrochim. Acta*, **51** [6] 1125-1129 (2005).

[9] Z. Zhong, C. Ouyang, S. Shi, and M. Lei, "Ab initio Studies on $Li_{4+x}Ti_5O_{12}$ Compounds as Anode Materials for Lithium-Ion Batteries," *Chem. Phys. Chem.*, **9** [14] 2104-2108 (2008).

[10] T.-F. Yi, Y. Xie, Y.-R. Zhu, R.-S. Zhu, and H. Shen, "Structural and Thermodynamic Stability of $Li_4Ti_5O_{12}$ Anode Material for Lithium-ion Battery," *J. Power Sources*, **222** 448-454 (2013).

[11] C. Ouyang, Z. Zhong, and M. Lei, "Ab initio Studies of Structural and Electronic Properties of $Li_4Ti_5O_{12}$ Spinel," *Electrochem. Commun.*, **9** [5] 1107-112 (2007).

[12] M. Armand, and J. M. Tarascon, "Building Better Batteries," *Nature*, **451** [7179] 652-657 (2008).

[13] I. Belharouak, Y.K. Sun, W. Lu, and K. Amine, "On the Safety of the $Li_4Ti_5O_{12}/LiMn_2O_4$ Lithium-Ion Battery System," *J. Electrochem. Soc.*, **154** [12] A1083-A1087 (2007).

[14] G.N. Zhu, H.J. Liu, J.H. Zhuang, C.X. Wang, Y.G. Wang, and Y.Y. Xia, "Carbon-coated Nano-sized $Li_4Ti_5O_{12}$ Nanoporous Micro-sphere as Anode Material for High-Rate Lithium-Ion Batteries," *Energy Environ. Sci.*, **4** 4016-4022 (2011).

[15] G. Du, N. Sharma, V.K. Peterson, J.A. Kimpton, D. Jia, and Z. Guo, "Br-Doped $Li_4Ti_5O_{12}$ and Composite TiO_2 Anodes for Li-Ion Batteries: Synchrotron X-Ray and In situ Neutron Diffraction Studies," *Adv. Funct. Mater.*, **21** [20] 3990-3997 (2011).

[16] M. Wagemaker, D.R. Simon, E.M. Kelder, J. Schoonman, C. Ringpfeil, U. Haake, D. Lützenkirchen-Hecht, R. Frahm, and F.M. Mulder, "A Kinetic Two-Phase and Equilibrium Solid Solution in Spinel $Li_{4+x}Ti_5O_{12}$," *Adv. Mater.*, **18** [23] 3169-3173 (2006).

[17] Y.-J. Bai, C. Gong, Y.-X. Qi, N. Lun and J. Feng, "Excellent long-term Cycling Stability of La-Doped $Li_4Ti_5O_{12}$ Anode Material at High Current Rates," *Journal of Materials Chemistry*, **22** [36] 19054-19060 (2012).

[18] K.-S. Park, A. Benayad, D.-J. Kang, and S.-G. Doo, "Nitridation-Driven

Conductive $Li_4Ti_5O_{12}$ for Lithium Ion Batteries," *J. Am. Chem. Soc.*, **130** [45] 14930-14931 (2008).

[19] L. Shen, C. Yuan, H. Luo, X. Zhang, S. Yang, and X. Lu, "In situ Synthesis of High-Loading $Li_4Ti_5O_{12}$-Graphene Hybrid Nanostructures for High Rate Lithium Ion Batteries," *Nanoscale*, **3** [2] 572-574 (2011).

[20] M. Chen, W. Li, X. Chen, and G.W. Diao, "A review of Research on Hematite as Anode Material for Lithium-Ion Batteries," *ACS Appl. Mater. Interfaces*, **6** [12] 4514-4523 (2014).

[21] J. Wang, H. Zhao, Q. Yang, C. Wang, P. Lv, and Q. Xia, "$Li_4Ti_5O_{12}$–TiO_2 Composite Anode Material for Lithium-Ion Batteries," *J. Power Sources*, **222** 196-201 (2013).

[22] Y.-Q. Wang, L. Gu, Y.-G. Guo, H. Li, X.-Q. He, S. Tsukimoto, Y. Ikuhara, and L.-J. Wan, "Rutile-TiO_2 Nanocoating for a High-Rate $Li_4Ti_5O_{12}$ Anode of a Lithium-Ion Battery," *J. Am. Chem. Soc.*, **134** [18] 7874-7879 (2012).

[23] M.M. Rahman, J.-Z. Wang, M.F. Hassan, D. Wexler, H.K. Liu, "Amorphous Carbon Coated High Grain Boundary Density Dual Phase $Li_4Ti_5O_{12}$-TiO_2: A Nanocomposite Anode Material for Li‐Ion Batteries," *Adv. Energy Mater.*, **1** [2] 212-220 (2011).

[24] J.-Y. Shin, J.H. Joo, and D. Samuelis, "Oxygen-Deficient TiO_2-δ Nanoparticles via Hydrogen Reduction for High Rate Capability Lithium Batteries," J. Maier, *Chem. Mater.*, **24** [3] 543-551 (2012).

[25] J.C. Parker, and R.W. Siegel, "Raman Microprobe Study of Nanophase TiO_2 and Oxidation-Induced Spectral Changes," *J. Mater. Res.*, **4** [06] 1246-1252 (1990).

[26] H. Zhang, and J.F. Banfield, "Understanding Polymorphic Phase Transformation Behavior During Growth of Nanocrystalline Aggregates: Insights from TiO_2," *J. Phys. Chem. B*, **104** [15] 3481-3487 (2000).

[27] M. Kitano, K. Funatsu, M. Matsuoka, M. Ueshima, and M. Anpo, "Preparation of Nitrogen-Substituted TiO_2 Thin Film Photocatalysts by the Radio Frequency Magnetron Sputtering Deposition Method and Their Photocatalytic Reactivity under Visible Light Irradiation," *J. Phys. Chem. B*, **110** [50] 25266-25272 (2006).

[28] J. Wang, D.N. Tafen, J.P. Lewis, Z.L. Hong, A. Manivannan, M. Zhi, M. Li, and N.Q. Wu, "Origin of Photocatalytic Activity of Nitrogen-Doped TiO_2 Nanobelts," *J. Am. Chem. Soc.*, **131** [34] 12290-12297 (2009).

[29] W. Zhang, and D.W. Liu, "Nitrogen-Treated Hierarchical Macro-/Mesoporous

TiO_2 Used as Anode Materials for Lithium Ion Batteries with High Performance at Elevated Temperatures," *Electrochim. Acta*, **156** 53-59 (2015).

[30] S. Lowell, J. E. Shields, M. A. Thomas, M. Thommes, *Characterization of Porous Solids and Powders: Surface Area, Pore Size and Density*, Kluwer, London, UK **2004**.

[31] W. Zhang, Y.X. Gong, N.P. Mellott, D.W. Liu, and J.G. Li, "Synthesis of Nickel Doped Anatase Titanate as High Performance Anode Materials for Lithium Ion Batteries," *J. Power Sources*, **276** 39-45 (2015).

[32] S. Yamanaka, G.W. Brindley, "High Surface Area Solids Obtained by Reaction of Montmorillonite with Zirconyl Chloride," *Clays Clay Miner*., **27** [2] 119-124 (1979).

[33] H. Ikawa, T. Yamada, K. Kojima, and S. Matsumot, "X-ray Photoelectron Spectroscopy Study of High- and Low-Temperature Forms of Zirconium Titanate," *J. Am. Ceram. Soc*., **74** [6] 1459-1462 (1991).

[34] N. Aas, T.J. Pringle, and M. Bowker, "Adsorption and Decomposition of Methanol on TiO_2, $SrTiO_3$ and SrO," *J. Chem. Soc. Faraday Trans*., **90** [7] 1015-1022 (1994).

[35] R.P. Vasquez, "X-ray Photoelectron Spectroscopy Study of Sr and Ba Compounds," *J. Electron Spectrosc. Relat. Phenom.*, **56** [3] 217-240 (1991).

[36] D. Gonbeau, C. Guimon, G. Pfister-Guillouzo, A. Levasseur, G. Meunier, and R. Dormoy, "XPS Study of Thin Films of Titanium Oxysulfides," *Surf. Sci.*, **254** [1] 81-89 (1991).

[37] W. Gopel, J.A. Anderson, D. Frankel, M. Jaehing, K. Phillips, J.A. Schafer, and G. Rocker, "Surface Defects of TiO_2 (110): A Combined XPS, XAES AND ELS Study," *Surf. Sci*., **139** [2-3] 333-346 (1984).

[38] A.N. Shultz, W.Y. Jang, W.M. Hetherington III, D.R. Baer, L.-Q. Wang, and M.H. Engelhard, "Comparative Second Harmonic Generation and X-Ray Photoelectron Spectroscopy Studies of the UV Creation and O_2 Healing of Ti^{3+} defects on (110) rutile TiO_2 surfaces," *Surf. Sci*., **339** [1] 114-124 (1995).

[39] J. Jamnika, and J. Maier, "Nanocrystallinity Effects in Lithium Battery Materials Aspects of Nano-Ionics. Part IV," *Phys. Chem. Chem. Phys.*, **5** [23] 5215-5220 (2003).

[40] L.Y. Beaulieu, D. Larcher, R.A. Dunlap, and J.R. Dahn, "Reaction of Li with Grain-Boundary Atoms in Nanostructured Compounds," *J. Electrochem. Soc.*, **147** [9] 3206-3212 (2000).

[41] T. Yuan, K. Wang, R. Cai, R. Ran, Z. Shao, "Cellulose-Assisted Combustion Synthesis of $Li_4Ti_5O_{12}$ Adopting Anatase TiO_2 Solid as Raw Material with High Electrochemical Performance," *J. Alloys Compd.*, **477** [1] 665-672 (2009).

[42] Z. Xing, A.M. Asiri, A.Y. Obaid, X. Sun, and X. Ge, "Carbon Nanofiber-Templated Mesoporous TiO_2 Nanotubes as a High-Capacity Anode Material for Lithium-Ion Batteries," *RSC Adv.*, **4** [18] 9061-9063 (2014).

[43] L. Shen, C. Yuan, H. Luo, X. Zhang, K. Xu, and Y. Xia, "Facile Synthesis of Hierarchically Porous $Li_4Ti_5O_{12}$ Microspheres for High Rate Lithium Ion Batteries," *J. Mater. Chem.*, **20** [33] 6998-7004 (2010).

[44] P. Yu, B.N. Popov, J.A. Ritter, and R.E. White, "Determination of the Lithium Ion Diffusion Coefficient in Graphite," *J. Electrochem. Soc.*, **146** [1] 8-14 (1999).

[45] S.T. Myung, K. Izumi, S. Komaba, Y.K. Sun, H. Yashiro, and N. Kumagai, "Role of Alumina Coating on Li-Ni-Co-Mn-O Particles as Positive Electrode Material for Lithium-Ion Batteries," *Chem. Mater.*, **17** [14] 3695-3704 (2005).

[46] G.N. Zhu, Y.G. Wang, and Y.Y. Xia, "Ti-Based Compounds as Anode Materials for Li-Ion Batteries," *Energy Environ. Sci.*, **5** [5] 6652 (2012).

[47] S. Huang, Z. Wen, X. Zhu, and Z. Gu, "Preparation and Electrochemical Performance of Ag Doped $Li_4Ti_5O_{12}$," *Electrochem. Commun.*, **6** [11] 1093-1097 (2004).

[48] D. Mu, Y. Hatano, T. Abe, and K. Watanabe, "Degradation Kinetics of Discharge Capacity for Amorphous Mg-Ni Electrode," *J. Alloy. Compd.*, **334** [1] 232-237 (2002).

[49] H. Li, G. Richter, and J. Maier, "Reversible Formation and Decomposition of LiF Clusters Using Transition Metal Fluorides as Precursors and Their Application in Rechargeable Li Batteries," *Adv. Mater.*, **15** [9] 735-739 (2002).

[50] A.A. Belak, Y. Wang, and A. Van der Ven, "Kinetics of Anatase Electrodes: The Role of Ordering, Anisotropy, and Shape Memory Effects," *Chem. Mater.*, **24** [15] 2894-2898 (2012).

[51] M. Yoshio, H. Noguchi, J.I. Itoh, M. Okada, and T. Mouri, "Preparation and Properties of $LiCo_yMn_xNi_{1-x-y}O_2$ as a Cathode for Lithium Ion Batteries," *J. Power Sources*, **90** [2] 176-181 (2000).

[52] Z. Li, D. Ding, Q. Liu, C. Ning, and X. Wang, "Ni-doped TiO_2 nanotubes for wide-range hydrogen sensing," *Nanoscale Res Lett.*, **9** [1] 118 (2014).

[53] L. Sun, J. Zhai, H. Li, Y. Zhao, H. Yang, and H. Yu, "Study of Homologous

Elements: Fe, Co, and Ni Dopant Effects on the Photoreactivity of TiO_2 Nanosheets," *ChemCatChem,* **6** [1] 339 (2014).

[54] A.N. Mansour, "Characterization of NiO by XPS," *Surf. Sci. Spectra,* **3** [3] 231 (1994).

[55] R. Zhang, and L. Gao, "Synthesis of Nanosized TiO_2 by Hydrolysis of Alkoxide Titanium in Micelles," *Key Eng. Mater.*, **224-226** 573-576 (2002).

[56] M.R. Mahmoudian, W.J. Basirun, and Y. Alias, "Synthesis of Polypyrrole/Ni-doped TiO_2 Nanocomposites (NCs) as a Protective Pigment in Organic Coating," *Prog. Org. Coat.,* **71** 56-64 (2011).

[57] A. Misra, P.K. Tyagi, M.K. Singh, and D.S. Misra, "FTIR Studies of Nitrogen Doped Carbon Nanotubes," *Diamond Relat. Mater.,* **15** 385-388 (2006).

[58] B.C. Viana, O.P. Ferreira, A.G.S. Filho, J.M. Filho, and O.L. Alves, "Structural, Morphological and Vibrational Properties of Titanate Nanotubes and Nanoribbons," *J. Braz. Chem. Soc.*, **20** 167 (2009).

[59] K.G. Kanade, B.B. Kale, R.C. Aiyer, and B.K. Das, "Effect of Solvents On the Synthesis of Nano-size Zinc Oxide and Its Properties," *Mater. Res. Bull.*, **41** 590-600 (2006).

[60] B. Pandey, P.P. Pal, S. Bera, S.K. Pay, and A.K. Kar, "Effect of Nickel Incorporation on Microstructural and Optical Properties of Electrodeposited Diamond Like Carbon (DLC) thin films," *Appl. Surf. Sci.*, **261** 789-799 (2012).

[61] C.C. Li, Q.H. Li, L.B. Chen, and T.H. Wang, "A Facile Titanium Glycolate Precursor Route to Mesoporous Au/$Li_4Ti_5O_{12}$ Spheres for High-Rate Lithium-Ion Batteries," *ACS Appl. Mater. Interfaces,* **4** 1233 (2012).

HIERARCHICAL NANOSTRUCTURES USED AS ANODE MATERIALS FOR LITHIUM-ION BATTERIES

A. Introduction

The previous work has proved that surface-modified TiO_2, $Li_4Ti_5O_{12}$ nanostructured materials are promising candidate anode materials for the next generation of LIBs. However, due to their relatively low intrinsic specific capacities (TiO_2, 335 mAh g^{-1}; $Li_4Ti_5O_{12}$, 175 mAh g^{-1}), some other work still need to be done that could further enhance the materials' capacities without the sacrifice of much cyclic stability and wide using temperature ranges.

During the past few years, molybdenum disulfide (MoS_2) has become the subject of significant attention as a battery anode material,[1,2] because of its high theoretical specific capacity (670 mAh g^{-1}) and layered structure that enables the convenient intercalation/extraction of Li^+ ions.[3] Thus far, various nanostructures of MoS_2 such as nanoflakes,[4] nanoplates,[5] and nanoflowers[6] have been reported for lithium storage. However, a larger volumetric expansion occurs in these MoS_2-based anodes during the conversion reaction of MoS_2 to LiS_2 upon lithiation (103%), which causes severe pulverization, particle aggregation, and unstable solid electrolyte interphase, hence resulting in poor cyclic stability, rate capability, and first cycle irreversible capacity loss.[7] By adopting kinds of carbon coating techniques, many researchers had improved the stability as well as rate capability of MoS_2 as anode materials.[3,8] However, the introduced carbon materials give rise to low volumetric energy density

or have limited effects on the enhancement of cyclic stability of the bare MoS_2.[6,7] Therefore, it is still highly desirable to improve the performance of MoS_2 by rational design of MoS_2 based hybrid nanocomposites.

Inspired by these findings, in this chapter, two different kinds of MoS_2 hierarchical nanostructures are designed. First, we developed a facile and scalable synthesis of MoS_2 decorated LTO nanosheet arrays (MoS_2@LTO) grown directly on Ti foil through a two-step strategy of hydrothermal reactions (part A). Second, we demonstrated a three-step strategy to synthesize a novel TiO_2/MoS_2 core-shell nanospheres *via* a facile microwave-assisted hydrothermal reaction, which is much faster than the traditional hydrothermal method and easy to scale-up for practical manufacturing (part B). These novel hierarchical nanocomposites have not been reported before. The as-prepared samples exhibited higher electrochemical performance than the previous ones obtained in chapter 2-4. Moreover, the binder-free MoS_2@LTO electrodes composed of free-standing nanoarrays grown on bendable substrates can potentially be applied in flexible electronics.

B. Synthesis of Nano-MoS_2 Decorated Self-supported $Li_4Ti_5O_{12}$ Nanosheet Arrays

1. Experimental procedure

Molybdenum disulfide decorated $Li_4Ti_5O_{12}$ (MoS_2@LTO) nanocomposite was synthesized in two steps. First, $Li_4Ti_5O_{12}$ nanosheet arrays were synthesized through a hydrothermal process and further calcination using a similar hydrothermal metal corrosion approach according to the literature.[9-11] In a typical synthesis process, Ti

foil disc (0.127 mm thick, 99%, Alfa Aesar) with a diameter of ~16 mm was immersed in a Teflon-lined stainless steel autoclave (Parr Instrument Co.) containing LiOH solution (12.8 mL, 0.09 M), which was heated to 200 °C and kept static for 24 h. After this treatment, the autoclave was cooled down to room temperature. The obtained Ti foil was washed with deionized water (DI) water three times and dried in air at 50 °C. Then, the prepared sample was calcined at 550 °C for 3 h in air to get the spinel LTO nanosheet arrays for further treatment. Second, the as-prepared foil was again immersed in a glucose solution (99%, anhydrous, Alfa Aesar) (30 mL, 1.5 mM) mixed with sodium molybdate (ACS, 98%, Alfa Aesar) (10 mg) and thiourea (ACS reagent, ≥99.0%, Sigma-Aldrich) (20 mg). The mixture was then transferred to the autoclave, heated to 200 °C and kept static for 24 h. After the autoclave was left to cool down to room temperature, the obtained foil was washed and further calcined at 500 °C for 4 h in an atmosphere of 10% H_2 balanced by N_2 to obtain the final product of MoS_2@LTO composites. For comparison, LTO nanosheet arrays without adding MoS_2 were also prepared during the first step of hydrothermal reaction and calcination. The structural characterization is similar to the formal chapters.

For the electrochemical evaluation, the weight of MoS_2@LTO nanocomposites on Ti foil was calculated by carefully measuring the total weights of the Ti foil before and after growth of MoS_2@LTO nanocomposites. The loading density of MoS_2@LTO was calculated to be 1.005 mg cm^{-2}. The Ti foil with MoS_2@LTO grown on one face was used as the work electrode.

2. Results and discussion

2.1 Morphological and structural analysis

The overall fabrication process of MoS_2 decorated LTO nanosheet arrays (MoS_2@LTO), which is illustrated in Figure 5-1, involves three steps. First, the self-supported LTO 2D nanosheet arrays were fabricated on a Ti foil substrate *via* a hydrothermal process followed by calcination in air. Then, part of the MoS_2 nanosheets grew on the surface of LTO nanosheet arrays with the assistance of glucose through another hydrothermal reaction. Meanwhile, the rest of MoS_2 nanosheet-assembled spheres grew in the spaces between LTO arrays. Finally, the hydrothermal MoS_2@LTO sample was calcined at 500 °C for 4h in an atmosphere of 10% H_2 balanced by N_2 to obtain the annealed MoS_2@LTO nanocomposites.

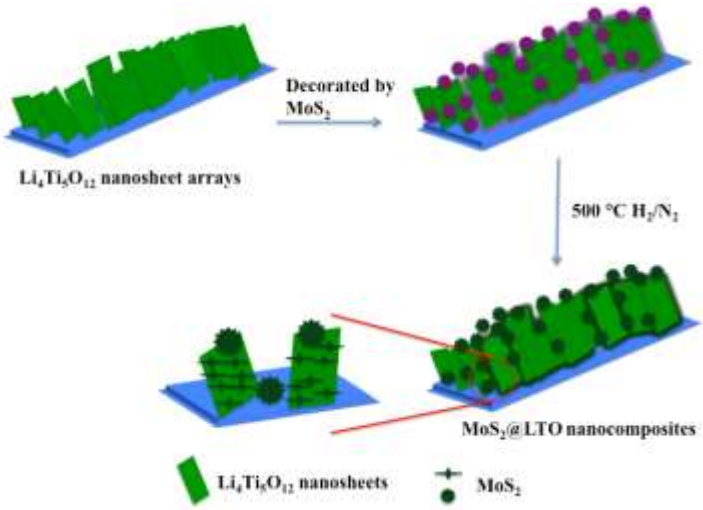

Figure 5-1. Schematic illustration of the fabrication process of the MoS_2@LTO nanocomposites.

Figure 5-2 shows the scanning electron microscope (SEM) images of the precursor of LTO nanosheet arrays (LTO-P) and the MoS_2@LTO nanocomposites. As shown in Figure 5-2a and 5-2b, after the first hydrothermal reaction and calcination, the Ti foil

substrate was uniformly covered vertically oriented aligned rectangular LTO nanosheets with a width of several hundred nanometers and thickness around 16 nm. These well-aligned LTO nanosheet arrays grew in tight contact to the Ti foil and had a yellow-green color (inset of Figure 5-2a). After another hydrothermal growth and calcination at 500 °C in an atmosphere of 10% H_2 balanced by N_2 for 4 h, MoS_2@LTO nanocomposites were formed with spheres of MoS_2 sheets, several hundred nanometers in diameter, on the surface of and in between the LTO nanosheets (Figure 5-2c and 5-2d). The color of the sample turned from yellow-green to black, indicating that MoS_2 nanosheets uniformly covered on the as-obtained LTO nanostructures (inset of Figure 5-2c). The X-ray diffraction (XRD) patterns of the LTO-P and MoS_2@LTO indicated the formation of spinel LTO and MoS_2. As shown in Figure 5-3, before it was decorated with MoS_2, LTO-P exhibited the spinel phase $Li_4Ti_5O_{12}$ (PDF No. 00-049-0207, space group Fd 3m(227), a= 8.36 Å), and diffraction peaks have been indexed in this figure. In addition, a tiny diffraction peak of anatase-TiO_2 also appeared in this pattern. After the further hydrothermal coating reaction and calcination, the diffraction peaks of MoS_2 appeared (PDF No. 01-077-1716, space group P63/mmc, a= 3.16 Å, c= 12.29 Å) together with the decreased intensities of LTO peaks, indicating the successful synthesis of MoS_2@LTO composites. The EDS spectrum further confirmed the presence of MoS_2 in the final hierarchical nanocomposites (Figure 5-4).

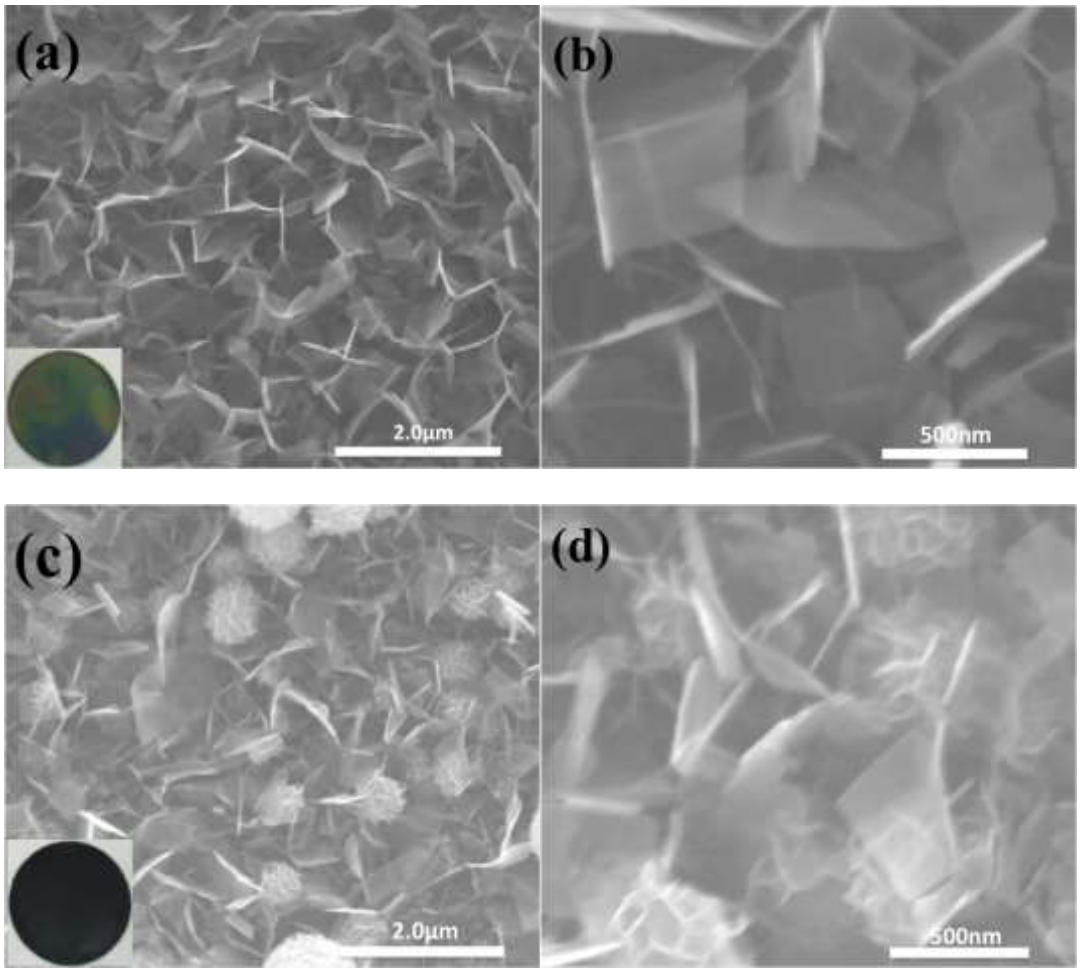

Figure 5-2. SEM images of samples obtained after different processes: low a) and high-magnification b) SEM images of LTO-P fabricated through hydrothermal reaction and further calcination at 550 °C for 3h; low c) and high-magnification d) SEM images of MoS_2@LTO reacted and calcined under the H_2@N_2 atmosphere at 500 °C for 4 h.

X-ray photoelectron spectroscopy (XPS) was employed to further investigate the surface composition of the MoS_2@LTO nanocomposites. As shown in Figure 5-5a, the two peaks at binding energies of 229.7 and, 232.8 eV (the error is ±0.1 eV), correspond well with the Mo $3d_{5/2}$ and Mo $3d_{3/2}$ peaks of Mo^{4+}, respectively.[12,13] In addition, there is another peak at a binding energy of 226.8 eV that can be ascribed to the S 2s peaks of nanostructured MoS_2.[12] Figure 5-5b shows two peaks at 162.6 and

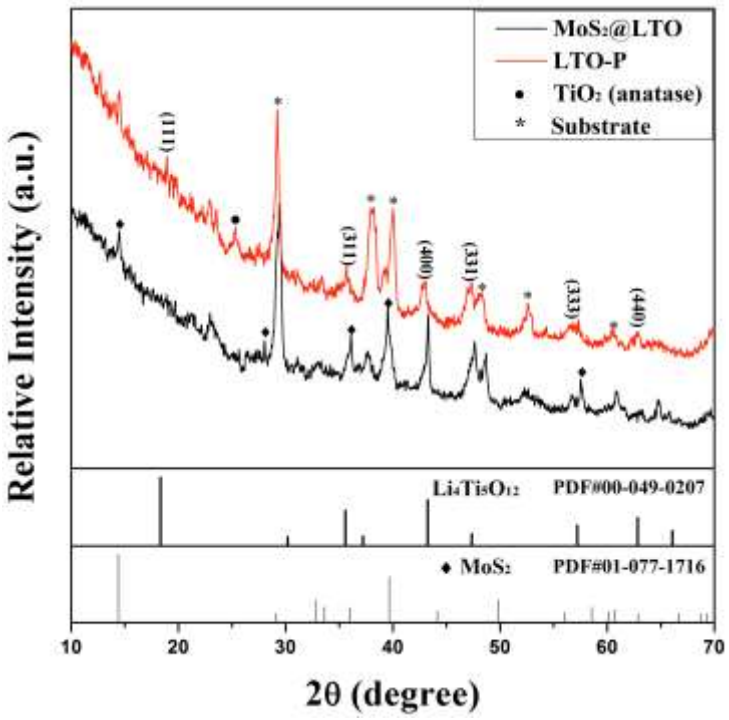

Figure 5-3. XRD patterns of the as-prepared LTO-P, and MoS_2@LTO nanocomposites.

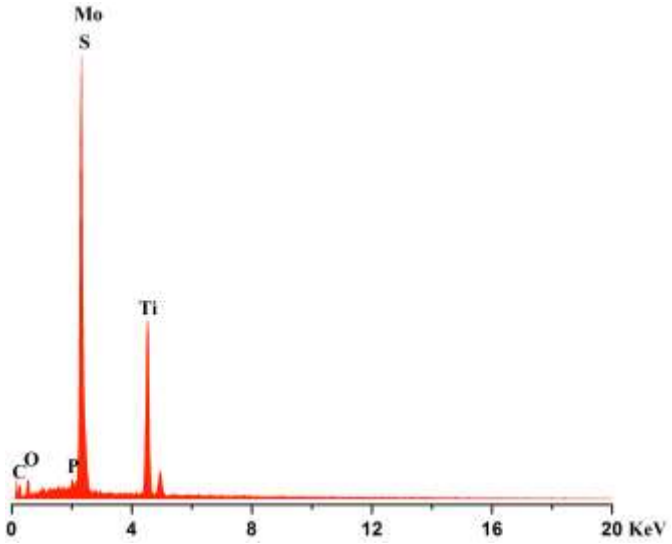

Figure 5-4. EDS spectrum of MoS_2@LTO nanocomposites.

163.8 eV (error is ±0.1 eV), corresponding to S $2p_{3/2}$ and S $2p_{1/2}$, comparable to that reported in the literature for nano-MoS_2.[12] This result suggests that the calcination under H_2@N_2 gas can successfully obtain pure crystalline nano-MoS_2 without oxidized side products (Figure 5-5c) such as molybdenum oxides and sulphides,

which are often observed in MoS_2 nanocomposites,[14,15] and which can interfere with electrochemical performance tests. The exact concentrations of LTO and MoS_2 (wt% of LTO and MoS_2) were further confirmed by inductively coupled plasma mass spectrometry (ICP-MS). The weight ratio of LTO and MoS_2 were approximately 33.5%, 67.5%, respectively.

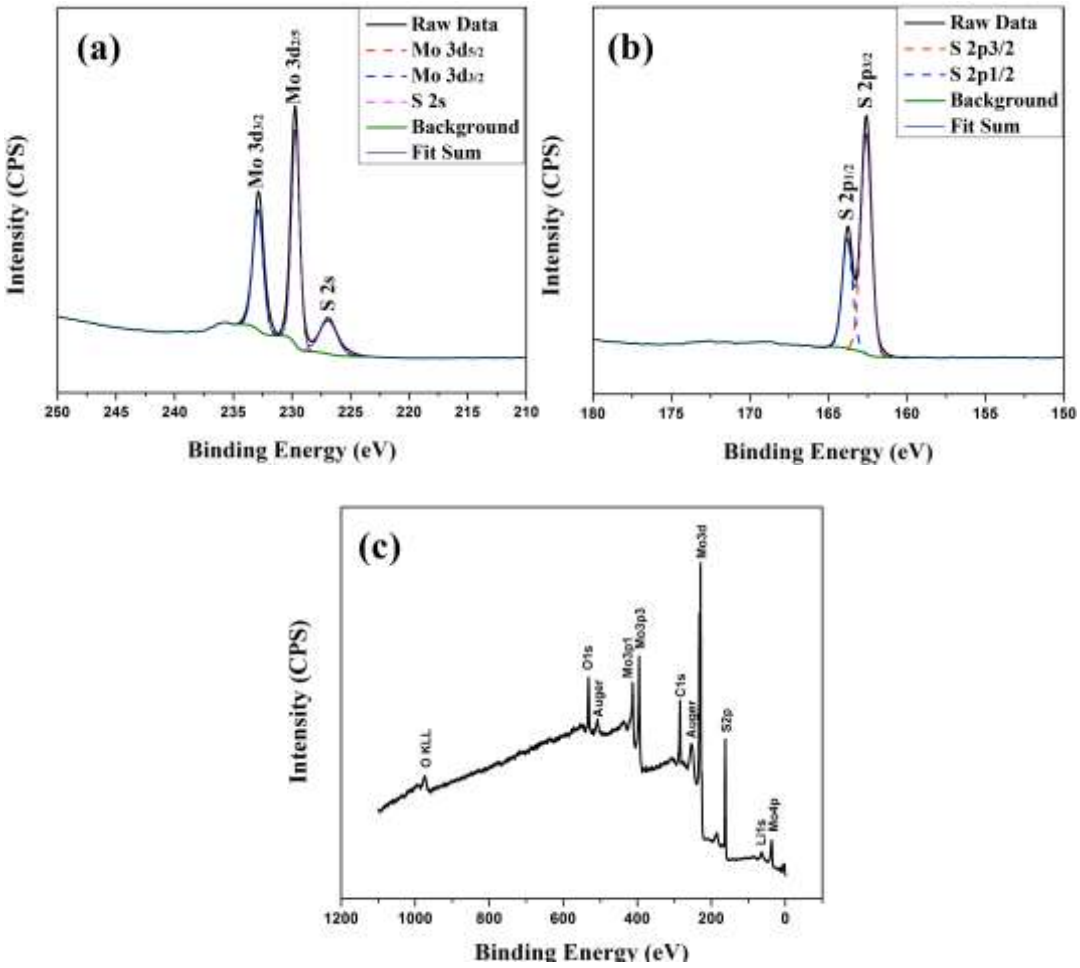

Figure 5-5. XPS spectra of MoS_2@LTO nanocomposites: a) Mo 3d and S 2s peaks and b) S 2p peaks, c) the wide spectrum of MoS_2@LTO nanocomposites, only signals arising from MoS_2 and $Li_4Ti_5O_{12}$; no other impurities were observed.

2.2 Electrochemical performance

The as-synthesized MoS_2@LTO nanocomposites on Ti foil were directly used as a binder-free anode for LIBs to construct a coin cell for electrochemical tests. There

might be some residual carbon existing in the prepared electrode due to the pyrolysis of glucose during the hydrothermal reaction.[16] The lithium-ion insertion/extraction properties of MoS_2@LTO electrodes were investigated by cyclic voltammetry (CV) and galvanostatic discharge/charge measurements. Figure 5-6a shows CV curves of the MoS_2@LTO nanocomposites for the 1st, 2nd, and 5th cycles, collected at a scanning rate of 0.1 mV s^{-1} in a potential window of 1-2.5 V vs. Li^+/Li. In the initial cathodic scan (discharge process), the sharp reduction peak at ~1.10V suggests the presence of a lithium insertion mechanism, which can be attributed to the insertion of lithium ions into MoS_2, thus forming $LiMoS_2$.[6] This peak disappeared and a new reduction peak at ~1.33 V can be observed in the subsequent cycles, indicating that MoS_2 experienced an irreversible phase transition in the initial discharge process.[17] Another sharp reduction peak at ~1.55 V, which was present in all cycles, was associated with insertion of spinel LTO lattice.[18] In the anodic scan (charge process), there were two dominant oxidation peaks at ~2.30 V and ~1.61 V with some intensity decrease in the following cycles, which were assigned to two major reversible conversion reactions of Li_2S to sulfur (S) and $Li_{4+x}Ti_5O_{12}$ to $Li_4Ti_5O_{12}$, respectively. The weak cathodic/anodic peaks at ~1.72 V and ~2.01 V corresponded to the lithiation of the slight amount of TiO_2,[18] which agrees well with the XRD results (Figure 5-3). The charge/discharge voltage profiles of the MoS_2@LTO nanocomposites in the 1st, 2nd, 5th, and 70^{th} cycles at a current density of 100 mA g^{-1}, tested at room temperature is shown in Figure 5-6b. In agreement with the CV results, after initial discharge, the plateau at ~1.10 V was replaced by the new plateau

at ~1.33 V in the discharge curves, and the charge/discharge plateaus at ~2.30 V and ~1.33 V is similar to reported MoS_2.[6] Another clear charge/discharge plateau at ~1.55 V in all cycles was ascribable to the redox reaction of Ti^{4+}/Ti^{3+} for LTO,[18] also consistent with the previous CV results. In the initial cycle, the MoS_2@LTO composites delivered a discharge and charge capacities of 705 mAh g^{-1} and 486 mAh g^{-1}, respectively, corresponding to a Coulombic efficiency of 69%, which may be due to the irreversible electrochemical decomposition of the electrolyte and the formation of a complicated interface.[1,19,20] After this capacity degradation, some capacity loss can be observed, the discharge and charge capacities were 488 mAh g^{-1} and 466 mAh g^{-1}, respectively, showing a Coulombic efficiency of 95%. This value was even larger in the subsequent cycles. After 70 cycles at the current density of 100 mA g^{-1}, MoS_2@LTO still delivered a reversible capacity of 433 mAh g^{-1} (0.435 mAh cm^{-2}), corresponding to a Coulombic efficiency of 99%. Furthermore, it also should be noted that the MoS_2@LTO composites still showed a relatively large charge/discharge voltage hysteresis similar to the reported MoS_2 composites,[3,19] which makes it not ideal as a good anode material. Thus, further work need to be done to investigate the factors associated with this voltage hysteresis and to improve it.

Figure 5-6c displays the rate performance of the MoS_2@LTO composites at different current densities from 100mA g^{-1} to 5000 mA g^{-1}. For comparison, the bare LTO nanosheet arrays without MoS_2 was also tested. As shown in this plot, MoS_2@LTO delivered a capacity of 488 mAh g^{-1} at a current density of 100 mA g^{-1} after an initial capacity degradation, and retained a capacity of 433 mAh g^{-1} after 70

cycles at different current densities, indicating the good cyclic stability. The theoretical capacity of the MoS_2@LTO nanocomposites can be calculated as follows [19,21]:

$$C_{MoS_2@LTO} = C_{MoS_2} \times wt\%_{MoS_2} + C_{LTO} \times wt\%_{LTO} = 670 \times 0.675 + 175 \times 0.335 \approx 511\left(mAh \cdot g^{-1}\right)$$

The above result indicates that the MoS_2@LTO nanocomposites can deliver a stable capacity over 85% of their theoretical value even after 70 cycles at different current densities. Meanwhile, this nanocomposite electrode also exhibited excellent rate capability with a reversible capacity of 173 mAh g^{-1} even at a high current density of 5000 mA g^{-1}. As a comparison, the bare LTO nanosheet arrays only delivered capacities of 173 mAh g^{-1} and 52 mAh g^{-1} at current densities of 100 mA g^{-1} and 5000 mA g^{-1}, respectively.

More significantly, a crucial parameter for lithium-ion batteries addressed to the storage of renewable energy sources, is the capability to sustain efficient operation over a wide temperature range. Figure 5-6d shows the MoS_2@LTO electrode tested over a temperature excursion spanning from -15 to 55 °C at a relatively large current density of 500 mA g^{-1} for 100 cycles. As shown in this plot, MoS_2@LTO delivered a capacity of 315 mAh g^{-1} after 100 cycles with a capacity retention ratio of 93% at room temperature (25 °C). Compared to the measurement at room temperature, when tested at -15 °C, it exhibited a little lower capacity of 270 mAh g^{-1} but better cyclic stability (98% of capacity retention after cycling). After increasing the test temperature to 55 °C, it still delivered a capacity of 299 mAh g^{-1} with decent cyclic stability (86% of capacity retention after 100 cycles). These results indicate that the

prepared nanocomposites fulfilled the requirement of working over a wide temperature range. Furthermore, even at these extreme temperatures for ordinary use, the sample still cycled with a stable capacity delivery.

Finally, the cyclic stability of MoS_2@LTO electrode was tested for 1000 cycles at room temperature. As shown in Figure 5-6e, even at a large current of 5000 mA g^{-1}, MoS_2@LTO nanocomposite still retained a capacity of 174 mAh g^{-1} after 1000 cycles with a capacity loss of only 2.1%. Meanwhile, the Coulombic efficiency is approximately closes to 100% during the whole measurement. The better cyclic stability at large current density can be ascribed to the high-surface-area of prepared MoS_2@LTO nanocomposite, in which the interfacial storage mechanism may take place that contribute much more at larger current densities, thereby reducing the depth of bulk intercalation and alleviating bulk degradation.[9,22-24] After 1000 cycles at the current density of 5000 mA g^{-1}, the MoS_2@LTO nanocomposites still retained their initial morphology with no obvious change (Figure 5-7). Such a good performance at these current densities, especially, the performance at a such high current density (5000 mA g^{-1}) is much better than that of nanostructured LTO,[9] TiN-coated LTO,[25] and LTO-graphene,[26] LTO-C nanotube arrays,[27] and LTO-TiO_2 composites.[28]

To further clarify the effects of MoS_2 coating on the electrochemical properties of LTO, electrochemical impedance spectroscopy (EIS) was carried out for both bare LTO-P and MoS_2@LTO after cycling at different current densities for 70 cycles. To obtain a fair comparison, the resistance values were normalized to the mass of the active material.

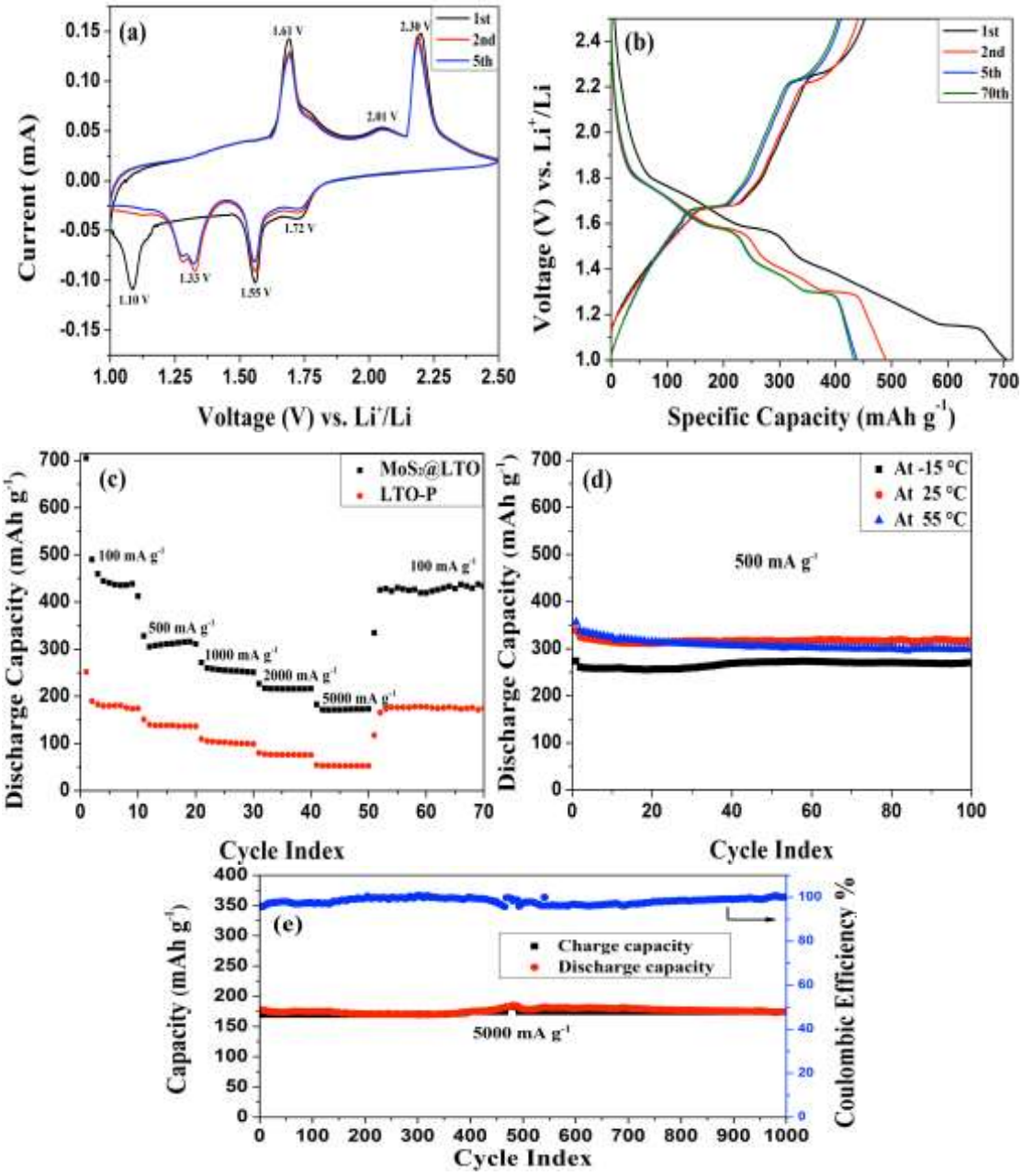

Figure 5-6. Electrochemical performance of MoS_2 decorated $Li_4Ti_5O_{12}$ nanocomposites (MoS_2@LTO) and bare $Li_4Ti_5O_{12}$ nanosheet arrays (LTO-P): a) cyclic voltammetry curves for the 1st, 2nd and 5th cycle of the MoS_2@LTO at a scan rate of 0.1 mV s^{-1}, b) galvanostatic charge/discharge voltage profiles of the MoS_2@LTO nanocomposite at a current density of 100 mA g^{-1}, c) rate performance of MoS_2@LTO and LTO-P at different current densities, d) cycling performance of MoS_2@LTO nanocomposite at various temperatures, e) specific capacity and Coulomic efficiency for 1000 cycles at a current density of 5000 mA g^{-1} for MoS_2@LTO at room temperature.

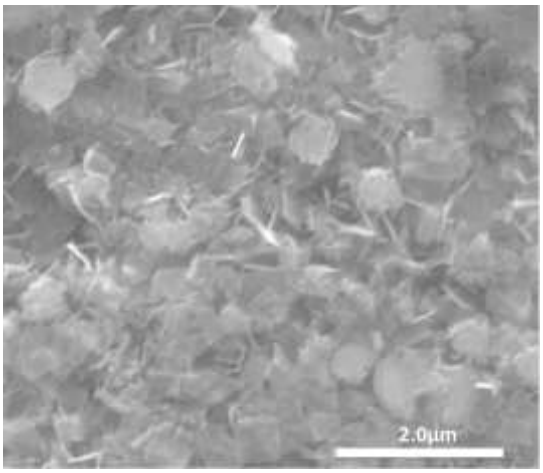

Figure 5-7. SEM image of MoS_2@LTO after 1000 cycles at the current density of 5000 mA g^{-1}.

The Nyquist plots are shown in Figure 5-8, which were composed of depressed semicircle in the high frequency (HF) region, and a sloped line in the low frequency (LF) region. For the depressed semicircles, the generally accepted interpretation is that the HF semicircle is characteristic of internal resistance, including the resistance of the electrode–electrolyte interface, separator, and electrical contacts, which corresponds to the ohmic resistance (R_s) in the equivalent circuit (Figure 5 inset), and the middle frequency (MF) semicircle is due to the impedance of the charge transfer reaction at the interface of electrolyte and active material (R_{ct}). In this plot, MoS_2@LTO showed an extra MF semicircle compared with the bulk LTO. Considering that the MoS_2@LTO electrodes cycling condition above 1 V (vs. Li^+/Li) will not have a solid electrolyte interface (SEI) film, this extra MF semicircle could be interpreted as the resistance of the interphase electronic contacts (R_I= 40Ω) between these two composites,[29,30] and the third semicircle can be attributed to the charge transfer resistance (R_{ct}). As shown in this plot, there was little difference between the LTO and MoS_2@LTO of the resistance R_s (5.6 Ω, 6.8 Ω). However, the MoS_2@LTO

exhibited a much smaller charge transfer resistance (R_{ct}= 9 Ω) than that of the bare LTO (R_{ct}= 76 Ω), and an obvious lower total resistance of the LTO composites can also be observed in this figure (55 Ω vs. 83 Ω). Given the fact that the incorporation of MoS_2 can greatly enhance the electronic conductivity of the MoS_2@LTO nanocomposite electrode, improved conductivity is considered to be a key factor in improving the rate performance, and cycling stability of the LTO nanohybrid composites in this study.

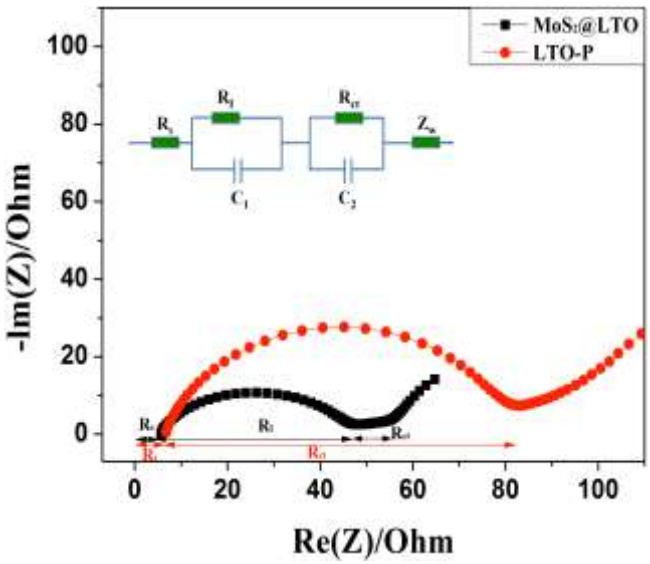

Figure 5-8. Nyquist plots of LTO-P and MoS_2@LTO after cycling, the inset shows the equivalent circuit used for fitting the experimental EIS data. The R terms are explained in the main text.

Based on the above results, the much improved electrochemical performance of the MoS_2 decorated LTO nanocomposites could be attributed to the following aspects: 1) the LTO nanosheet arrays directly grown on Ti substrate, which is favorable for fast electron transport as well as retaining the morphology of nanostructures during cycling; 2) the interconnected robust nanosheet arrays of the LTO backbone could effectively accommodate the strain of the volume change of MoS_2 and maintain the

hierarchically conductive network, which brings about high capacity and excellent cycling stability over a wide temperature range; 3) introduced MoS_2 nanosheets provide high electrode/electrolyte interfacial contact areas and numerous open channels for the access of electrolyte and shorten the diffusion paths of Li^+ ions, thus improving the dynamic performance of Li^+ storage. All these reasons explain why the MoS_2@LTO nanocomposites exhibited a superior electrochemical performance in this experiment.

3. Conclusion

In summary, a novel nanohybrid MoS_2@LTO composite is successfully fabricated through a simple hydrothermal process. Owing to the unique hierarchical structure, sufficient conductivity, high contact surface area, and good structure stability of the MoS_2 decorated LTO nanosheets arrays, the prepared MoS_2@LTO nanocomposites exhibited high revisable capacity, wide operating temperature range, remarkable rate capability and excellent cycling stability. This proposed synthesis strategy will provide a novel and feasible method for the synthesis of other composites, and such binder and additive free hybrid MoS_2 electrodes are expected to open up new avenues to power flexible electronic devices.

C. Microwave-Hydrothermal Synthesis of MoS_2/TiO_2 Core-shell Nanostructures

1. Experimental procedure

The synthesis procedure involves three steps. First, MoS_2 nanosheet-assembled spheres were synthesized through a microwave-assisted hydrothermal process. In a typical synthesis process, 0.6 g of sodium molybdate (ACS, 98%, Alfa Aesar) was added to 30 mL of glucose solution (99%, anhydrous, Alfa Aesar) (0.05 M) mixed with thiourea (ACS reagent, ≥99.0%, Sigma-Aldrich) (0.6 g) under stirring. The mixture solution was then transferred to a Teflon-lined autoclave with a 50 mL capacity that was transparent to microwave irradiation. The autoclave was sealed and placed in the microwave oven being heated at 200 °C for 1.3 h under stirring. The autoclave was allowed to cool to room temperature naturally after the reaction. The black suspension was washed with deionized (DI) water three times and dried in air at 50 °C. Second, the as-prepared MoS_2 nanoparticles were coated with TiO_2 through an extension of classical Stöber method.[31,32] 0.1 g of core MoS_2 were dispersed in anhydrous ethanol (100 mL, >99.5%, Anhydrous, Sigma-Aldrich), and mixed with concentrated ammonia solution (0.5 mL, ACS, 30%, Alfa Aesar) under ultrasound for 20 min. Afterward, 0.85 mL of tetrabutyl titanate (TBOT) (>97%, Sigma-Aldrich) was added dropwise for 5 min, and the reaction was allowed to proceed for 24 h at 45 °C under continuous stirring. The resultant products were separated and collected, followed by washing with DI water and ethanol for 3 times, respectively. Then, the obtained powders were dried at 50 °C overnight. Third, the obtained samples were treated with another microwave-assisted hydrothermal reaction in LiOH solution

(1.0M) at 140°C for 1.3 h, leading to the formation of MoS_2/TiO_2 core-shell nanospheres. The final products were calcined at 400 °C for 3 h in an atmosphere of 10% H_2 balanced by N_2. For comparison, MoS_2 nanoparticles without coating TiO_2 were also prepared during the first step of microwave-assisted hydrothermal reaction and calcination. The structural characterization and electrochemical evaluation are similar to the formal chapters.

2. Results and discussion

2.1 Morphological and structural analysis

The overall fabrication process of core-shell MoS_2/TiO_2 is illustrated in Figure 5-9, involves three steps.

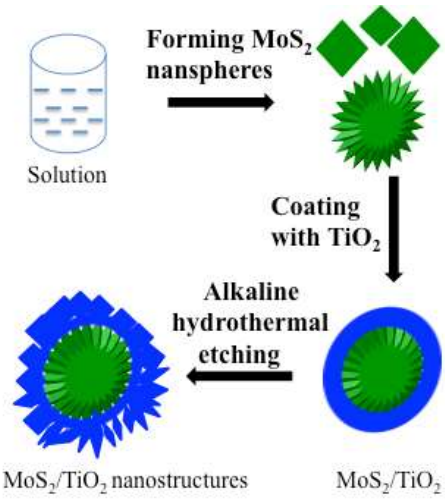

Figure 5-9. Schematic illustration of the fabrication process of the MoS_2/TiO_2 nanostructures.

First, the MoS_2 nanosheets assembled spheres were synthesized through a microwave-assisted hydrothermal process. Second, the as-prepared MoS_2 nanoparticles were coated with titania *via* a simple Stöber approach using tetrabutyl titanate (TBOT) as a precursor. Third, the obtained MoS_2/TiO_2 nanoparticles were

microwave-hydrothermally treated in LiOH solution (1.0 M) at 140 °C, leading to the formation of nanosheet-based shell MoS_2/TiO_2 nanospheres. Finally, the prepared MoS_2/TiO_2 samples were treated at 400 °C for 3 h in an atmosphere of 10% H_2 balanced by N_2 to obtain the annealed MoS_2/TiO_2 hybrid nanostructures.

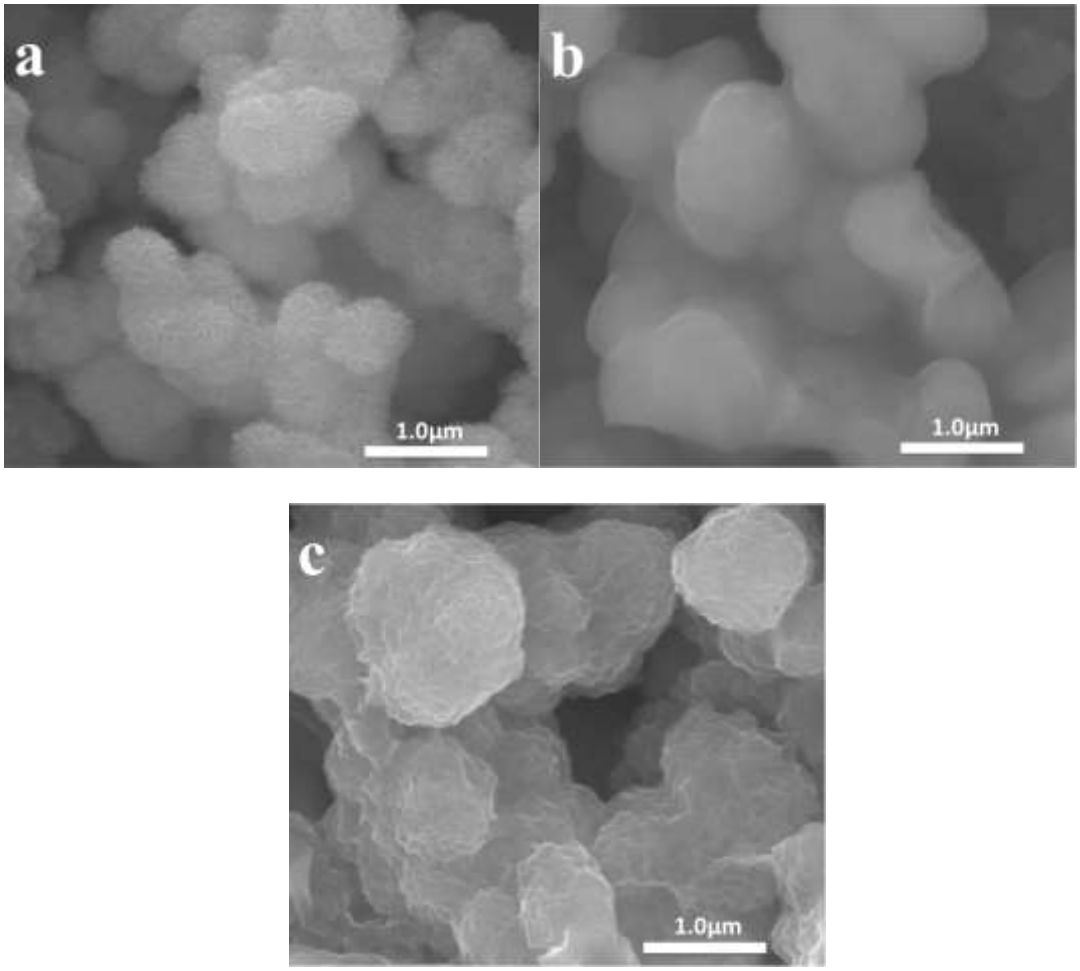

Figure 5-10. SEM images of samples obtained after different reaction process: a) MoS_2 nanosheet-assembled spheres fabricated through microwave-hydrothermal reaction; b) MoS_2/TiO_2 nanoparticles prepared after sol-gel process; c) core-shell MoS_2/TiO_2 nanostructures with nanosheet-based shell reacted and calcined under $H_2@N_2$ atmosphere at 400 °C for 3 h.

Figure 5-10 shows the scanning electron microscope (SEM) images of samples obtained after different processes. As shown in Figure 5-10a, after the first

microwave-hydrothermal reaction, ultra-thin MoS_2 nanosheets assembled spheres can be obtained, which has a mean diameter of 600 nm. After the following sol-gel process at 45 °C for 24 h, MoS_2/TiO_2 nanoparticles were formed that showed a mean diameter of ~700 nm (Figure 5-10b). The MoS_2/TiO_2 nanoparticles possessed smooth surface compared with MoS_2 nanospheres (Figure 5-10a). After another microwave-hydrothermal treatment in LiOH solution (1.0 M) at 140 C for 1.3 h, unique nanosheet-based spheres with a mean size of ~1μm were obtained (Figure 5-10c), and the growth followed a "partial dissolution-anisotropic growth" process that has been reported in our previous work.[33] The X-ray diffraction (XRD) pattern of MoS_2/TiO_2 after calcination indicated the formation of MoS_2 and anatase TiO_2.

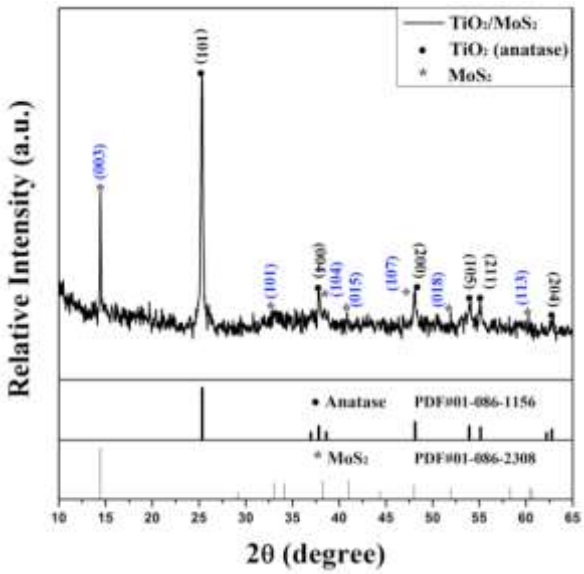

Figure 5-11. XRD pattern of as-prepared MoS_2/TiO_2 nanostructures after calcination.

As shown in Figure 5-11, the diffraction peaks can be indexed to MoS_2 phase (PDF No. 01-086-2308, space group P63/mmc, a= 3.16 Å, c= 12.29 Å) and antase-TiO_2 phase (PDF No. 01-086-1156, space group 141/amd, a= 3.78 Å, c= 9.51 Å), respectively. The detected peaks can be mainly assigned to the (003), (101), (015),

and (113) planes of the rhombohedral MoS_2 phase and the (101), (004), (200) and (204) planes of the anatase TiO_2 phase. The energy-dispersive spectrometry (EDS) spectra further confirmed the presence of Mo, Ti, S, and O in the final hierarchical nanostructures (Figure 5-12).

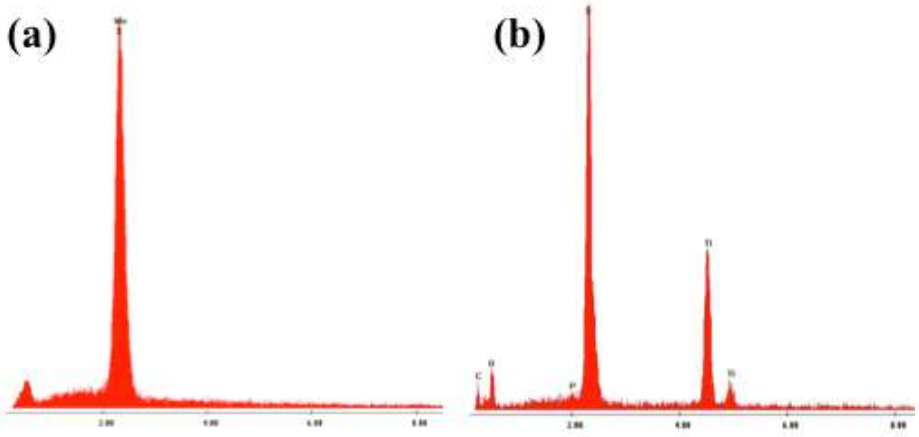

Figure 5-12. EDS spectra of MoS_2 a) and MoS_2/TiO_2 nanostructures b).

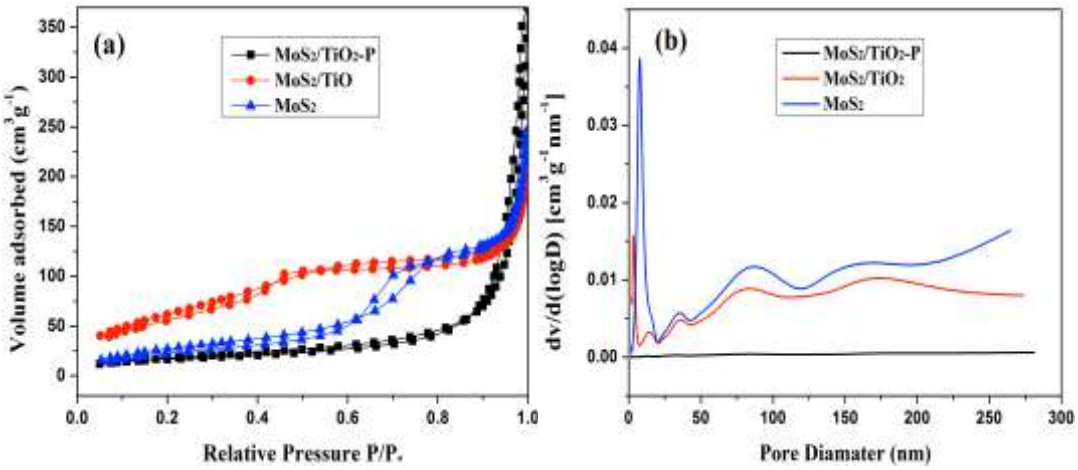

Figure 5-13. a) Nitrogen adsorption/desorption isotherms and b) pore-size distribution curves of samples obtained after different processes. The MoS_2/TiO_2-P is represented the sample after the sol-gel reaction.

To further investigate the effects of microwave-hydrothermal etching on the surface area of prepared MoS_2/TiO_2 nanoparticles, nitrogen sorption measurements of bare MoS_2 and MoS_2/TiO_2 nanoparticles before and after microwave-hydrothermal etching were shown in Figure 5-13. The specific surface areas of these three samples

were calculated using the Barrett-Joyner-Halenda (BJH) method to be 271.8 m^2 g^{-1}, 5.4 m^2 g^{-1}, and 104.5 m^2 g^{-1}, respectively (MoS_2, MoS_2/TiO_2-P and MoS_2/TiO_2). As shown in Figure 5-13a, the isotherm curves of MoS_2 and MoS_2/TiO_2 exhibited typical adsorption hysteresis that belongs to type IV isotherm curves, indicating that these two samples have nanoporous structure, derived from the packing of the nanosheets. For comparison, the MoS_2/TiO_2 nanoparticles synthesized after the sol-gel process, which has type II isotherm curve with little porosity. These results agree well with the SEM images as shown in Figure 5-10. Figure 5-13b shows the corresponding pore-size distribution curves of these three samples. As shown in this figure, MoS_2 showed large porosity with pores sizes under 100 nm, while these pores have almost vanished after the sol-gel process (MoS_2/TiO_2-P). However, after the further microwave-hydrothermal etching, sample MoS_2/TiO_2 exhibited comparable pores in the pore sizes of less than 300 nm, which indicates that this microwave-hydrothermal etching is a useful way to increase the surface area of as-prepared MoS_2/TiO_2 nanoparticles, thus leading to a favorable structure for the lithium ion transportation.

2.2 Electrochemical performance

The calcined MoS_2/TiO_2 hybrid nanostructures were then assembled into two-electrode coin type cells to investigate the electrochemical performance with the Li metal as the counter-electrode. For comparison, the bare MoS_2 nanosheet-based spheres without coated TiO_2 were also tested. Figure 5-14a shows the cyclic voltagrams (CVs) of MoS_2 and MoS_2/TiO_2 electrodes at a scan rate of 0.1 mV s^{-1} in a potential window of 0.2~2.5 V versus Li^+/Li for the first cycle. As shown in this

figure, for the sample MoS_2/TiO_2, there were three reduction peaks located at ~0.56, 1.10, and 1.61 V in the initial cathodic sweep (discharge process) (Figure 5-14a). The peak at ~1.12 V corresponds to the Li ion insertion into MoS_2.[6,34] The pronounced peak located at ~0.56 V corresponds to the decomposition of MoS_2 into Mo nanoparticles embedded in a Li_2S matrix, which is based on the conversion reaction:[35]

$$MoS_2 + 4Li^+ + 4e^- \rightarrow Mo + 2Li_2S \quad (1)$$

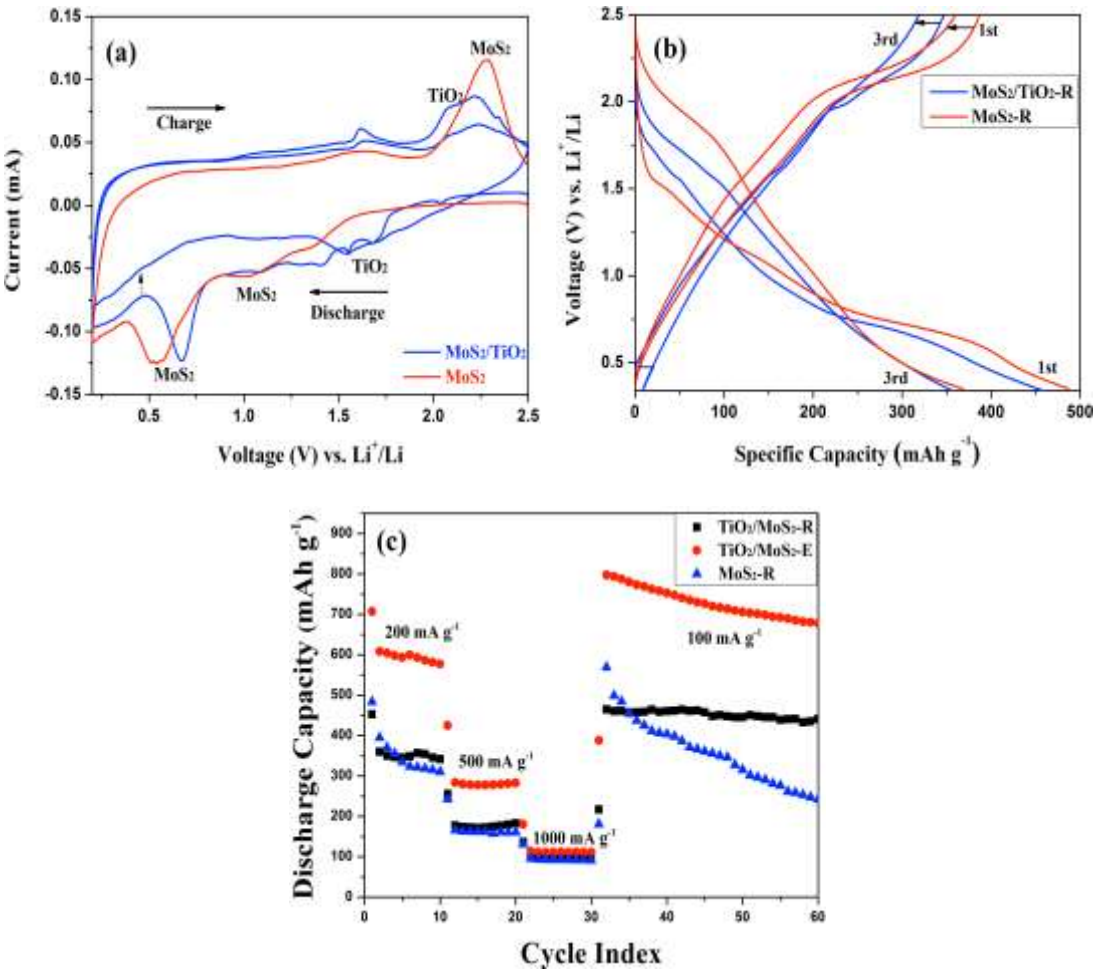

Figure 5-14. Electrochemical performance of MoS_2/TiO_2 core-shell nanostructure and bare MoS_2 nanospheres: a) cyclic voltammetry curves at a scan rate of 0.1 mV s^{-1}, b) galvanostatic charge/discharge voltage profiles of first and third cycles at a current density of 200 mA g^{-1}, c) rate performance of samples at different current densities at room temperature and 55 °C.

The disappearance of both of the reduction peaks in the following cycle suggested the irreversibility in the conversion of MoS_2 into Li_2S and Mo.[6] Another reduction peak at ~1.61 V, which was present in these two cycles, was associated with Li ion insertion of anatase TiO_2 following reaction:[36]

$$TiO_2 + xLi^+ + xe^- \rightarrow Li_xTiO_2 (0 < x < 1) \quad (2)$$

Meanwhile, there are two dominant oxidation peaks located at ~2.01 and 2.30 V in the anodic sweep (charge process) in these two cycles, which are attributed to the two major reversible conversion reactions of Li_xTiO_2 to TiO_2 and Li_2S to sulfur (S), respectively. As the comparison, the CV curve of bare MoS_2 only showed similar oxidation/reduction peaks for MoS_2 during the cathodic/anodic sweep. These results illustrate that the hybrid nanostructures of MoS_2/TiO_2 play a major role in the electrochemical performance, and the TiO_2 shell also makes a contribution to the charge/discharge capacity. Figure 5-14b displays the charge/discharge voltage profiles of these two samples in the first and third cycles at the current density of 200 mA g^{-1}, tested at room temperature. In the initial cycle, MoS_2/TiO_2 showed three plateaus located at ~0.56, 1.10, and 1.60 V on the charge curve, suggesting the three-step lithiation process; and the other two plateaus at ~2.01 and 2.30 V during discharge process corresponded to the reversible Li^+ extraction. For the bare MoS_2, there were three plateaus located at ~0.51, 1.10, and 2.30 V during the charge/discharge process correspond to the Li ion extraction/insertion only for MoS_2 phase. In the third cycle, the plateaus at ~0.46 and 1.10 V disappeared in the discharge process for the both two samples, and the charge/discharge plateaus at ~2.30, 1.61, and 2.0 V are similar to

report MoS_2 and TiO_2,[6,35] which are also in accordance with the previous CV profiles (Figure 5-13a). In the initial cycle, MoS_2/TiO_2 nanostructures delivered relatively lower discharge and charge capacities of 454 mAh g^{-1} and 353 mAh g^{-1} compared to the bare MoS_2 (487, 380 mAh g^{-1}), indicating the contribution of TiO_2 to the charge/discharge capacity. In the following cycles, there was an obvious capacity degradation for these two samples due to the formation of the solid electrolyte interface (SEI) film and the irreversible reaction between Li and MoS_2/TiO_2 as indicated in reactions (1) and (2). The discharge and charge capacities were 354, 315 and 368, 351 mAh g^{-1} for MoS_2/TiO_2 and MoS_2 at the 3rd cycle, respectively. In addition, it also should be noted that the MoS_2/TiO_2 composites still showed a relatively large charge/discharge voltage hysteresis similar to the reported MoS_2 composites,[3] which makes it not ideal as a good anode material. Thus, further work needs to be done to investigate the factors associated with this voltage hysteresis and to improve it.

Figure 5-14c shows the cycling performance of MoS_2/TiO_2 and MoS_2 in the 60-cycle test at room temperature under different current densities from 100 mA g^{-1} to 1000 mA g^{-1}. As shown in this plot, the bare MoS_2-R exhibited a higher discharge capacity of 487 mAh g^{-1} in the initial cycle than the MoS_2/TiO_2-R (454 mAh g^{-1}) at the current density of 200 mA g^{-1}. However, this capacity dropped continuously, with a capacity of 298 mAh g^{-1} left after 10 cycles and the capacity retention rate was only 61%. Furthermore, when the current density was increased to 500 mA g^{-1} at the 11th cycle, the capacity dropped to 155 mAh g^{-1}, and this capacity will further decrease to

90 mAh g^{-1} while the current density was increased to 1000 mA g^{-1} at the 21st cycle. After the current density was decreased to 100 mA g^{-1} at the 31st cycle, the discharge capacity increased to 580 mAh g^{-1}. After 30 cycles, it only exhibited a discharge capacity of 207 mAh g^{-1} with the continuous decrease, and its capacity retention rate is 36%. In contrast, MoS_2/TiO_2-R started with a relatively lower initial discharge capacity of 457 mAh g^{-1} but experienced much less capacity degradation in the first 10 cycles. In addition, when the current density is decreased to 100 mA g^{-1} at the 31st cycle, MoS_2/TiO_2-R delivered a discharge capacity of 462 mAh g^{-1} which showed little capacity fading in the following 30 cycles and was still as high as 410 at the 60th cycle with the capacity retention of 89%.

In addition, it is well-known that when the testing temperature of lithium ion batteries is increased to more than 50 °C, the capacity of batteries increases at the cost of cyclic stability.[33] So in our study, we also tested the cycling performance of MoS_2/TiO_2 hybrid nanostructures at an elevated temperature of 55 ºC (denoted as MoS_2/TiO_2-E). The result is also shown in Figure 5-14c. MoS_2/TiO_2-E delivered a higher discharge capacity of 703 mAh g^{-1} than that of the MoS_2/TiO_2-R, and had a similar capacity degradation in the initial cycle when tested at the current density of 200 mA g^{-1}. After this capacity degradation, some capacity loss can be observed; the discharge capacity was 560 mAh g^{-1} at the 10th cycle with a decent capacity retention ratio of 80%. When the current density is decreased to 100 mA g^{-1} at the 31st cycle, the discharge capacity recovered to 801 mAh g^{-1} and showed reasonable capacity fading in the following cycles. Finally, MoS_2/TiO_2-E delivered a capacity of 659 mAh

g^{-1} at the 60^{th} cycle, and the capacity retention ratio is 82% that is also much higher that that of MoS_2-R tested at room temperature. Above electrochemical results show that the TiO_2 nanosheet-based shell decorated MoS_2 samples have noticeably better Li ion storage capability than the bare MoS_2, and is also stable when used at a high temperature of 55 °C. Furthermore, the average discharge capacity of this MoS_2/TiO_2 hybrid nanostructure is preferable compared to previously reported mesoporous MoS_2/TiO_2 nanofibers,[37] TiO_2 supported SnO_2,[38] TiO_2/α-Fe_2O_3 core/shell arrays[39] and core-shell TiO_2/MoO_xS_y nanocomposites.[40]

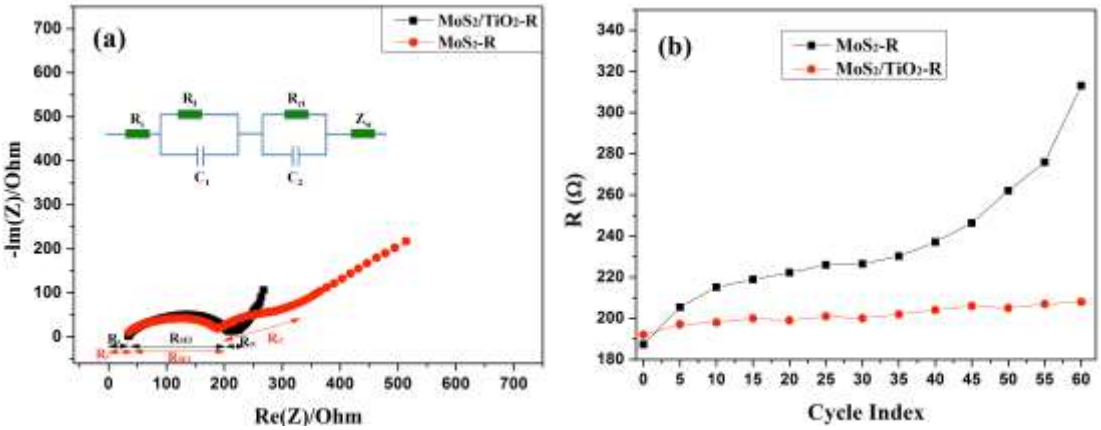

Figure 5-15. Nyquist plots of MoS_2/TiO_2 and MoS_2 after different cycles tested at room temperature : a) Nyquist plots after 60 cyles, the inset shows the equivalent circuit used for fitting the experimental EIS data, b) Total resistance as funtion of cycle number.

To further clarify the effects of TiO_2 coating on the electrochemical properties of MoS_2, electrochemical impedance spectroscopy (EIS) was carried out for both bare MoS_2 and MoS_2/TiO_2 after different cycles at various current densities for 60 cycles when tested at room temperature. To obtain a fair comparison, the resistance values were normalized to the mass of the active material, and all measurements were taken after full relaxation. The Nyquist plots are shown in Figure 5-15a. As shown in this

figure, the Nyquist plots of MoS_2 and MoS_2/TiO_2 after 60 cycles were composed of one depressed semicircle in the high frequency (HF) region, two semicircles in the middle frequency (MF) region, and a sloped line in the low frequency (LF) region. For the depressed semicircle in HF region, which is characteristic of internal resistance (R_s), including the resistance of the electrode–electrolyte interface, separator, and electrical contacts. This resistance is similar for MoS_2 and MoS_2/TiO_2 during cycling because of the fact that both materials are coated directly on the substrates that used as the current collector (5.7 Ω, 6.3 Ω), which ensures good electrical conductivity in the electrodes. In the MF region, the first semicircle can be interpreted as the resistance of solid electrolyte interface (SEI) film (R_{SEI}), and the second semicircle is due to the impedance of the charge transfer reaction at the interface of electrolyte and active material (R_{ct}). Based on the behavior of our EIS spectra and the others' studies,[30] we proposed an equivalent circuit for the Nyquist plots of these two samples (Figure 5-15a inset). In addition, there was little difference between the MoS_2 and MoS_2/TiO_2 of the resistance R_{SEI} (183 Ω, 188 Ω). However, the MoS_2/TiO_2 exhibited a much smaller charge transfer resistance (R_{ct}= 23 Ω) than that of the bare MoS_2 (R_{ct}= 125 Ω), and thus an obvious lower total resistance can also be observed in this figure (207 Ω vs. 313 Ω).

To get more insight into the resistance change during cycling, figure 5-15b plotted the total resistance of R for these two samples after each five cycles. As shown in this figure, before the electrochemical measurement, the bare MoS_2 exhibited a smaller resistance (187 Ω) than the MoS_2/TiO_2 (193 Ω) due to the higher intrinsic electrical

conductivity of MoS_2 compared to TiO_2. However, there was a continuously resistance increase for MoS_2 during cycling, and it showed a total resistance of 313 Ω after 60 cycles, suggesting that the volumetric change occurred in the cycling did cause unstable interface of the electrolyte and active material. In contrast, the TiO_2 coated sample MoS_2/TiO_2 exhibited smaller increase on the resistance with a value of 207 Ω after 60 cycles. Meanwhile, for the bare MoS_2, more quickly resistance increase can be observed when cycled at the relatively lower current density (100, and 200 mA g^{-1}), which is corroborated well with the conclusion that the capacity degradation can be more readily observed when tested using a small current density.[41] These results proved that the coated TiO_2 could greatly improve the charge transfer process at the electrode/electrolyte interface and maintain good electronic conductivity during long-term cycling. Thus, these improved interface properties are considered to be a key factor in improving the cycling stability of the MoS_2/TiO_2 hybrid nanostructures in this study.

Based on the above results, the enhanced lithium storage properties of the MoS_2/TiO_2 hybrid nanostructures could be explained in detail as follow: 1) the TiO_2 coating could provide better accommodation of the strain of Li ion intercalation/extraction, thus the large volume change of MoS_2 during charge/discharge can be buffered, which brings about stable cycling performance even at a low current density and at elevated temperature; 2) the nanosheet-based TiO_2 shell has large electrode/electrolyte interfacial contact areas and more active sites for Li ion transportation; 3) The nanosheet-based TiO_2 and MoS_2 nanostructures

can store more lithium ion, have better structural flexibility, and decrease lithium ions' and electrolyte diffusion path simultaneously.

3. Conclusions

In summary, we have demonstrated a microwave-assisted hydrothermal strategy to synthesize MoS_2/TiO_2 core-shell hybrid nanostructures with a nanosheet-based shell. This approach is facile, efficient and easy to scale-up. Compared to MoS_2, the as-prepared MoS_2/TiO_2 materials exhibited high revisable capacity, wide operating temperature range and remarkably improved cycling stability when used as lithium ion battery electrodes, and the existence of TiO_2 nanosheet-based shell is considered to play an irreplaceable role in enhancing its electrochemical performance. This proposed synthesis strategy could be easily extended to design other hybrid nanostructured materials used in high-performance LIBs and relevant fields.

References

[1] J. Xiao, X. Wang, X.Q. Yang, S. Xun, G. Liu, P.K. Koech, J. Liu, and J.P. Lemmon, "Electrochemically Induced High Capacity Displacement Reaction of PEO/MoS_2/Graphene Nanocomposites with Lithium," *Adv. Funct. Mater.*, **21** [15] 2840-2846 (2011).

[2] U. K. Sen, and S. Mitra, "High-Rate and High-Energy-Density Lithium-Ion Battery Anode Containing 2D MoS_2 Nanowall and Cellulose Binder," *ACS Appl. Mater. Interfaces*, **5** [4] 1240-1247 (2013).

[3] K. Chang, W. Chen, L. Ma, H. Li, H. Li, F. Huang, Z. Xu, Q. Zhang, and J.-Y. Lee, "Graphene-Like MoS_2/Amorphous Carbon Composites with High Capacity and Excellent Stability as Anode Materials for Lithium Ion Batteries," *J. Mater. Chem.*, **21** [17] 6251-6257 (2011).

[4] H. Hwang, H. Kim, and J. Cho, "MoS_2 Nanoplates Consisting of Disordered Graphene-Like Layers for High Rate Lithium Battery Anode Materials," *Nano letters,* **11** [11] 4826-4830 (2011).

[5] Li, H.; Li, W.; Ma, L.; Chen, W.; Wang, J. "Electrochemical Lithiation/Delithiation Performances of 3D Flowerlike MoS_2 Powders Prepared by Ionic Liquid Assisted Hydrothermal Route," *J. Alloys Compd.*, **471** [1] 442-447 (2009).

[6] T. Stephenson, Z. Li, B. Olsen, and D. Mitlin, "Lithium Ion Battery Applications of Molybdenum Disulfide (MoS_2) Nanocomposites," *Energy Environ. Sci*., **7** [1] 209-231 (2014).

[7] X. Li, W. Li, M. Li, P. Cui, D. Chen, T. Gengenbach, L. Chu, H. Liu, and G. Song, "One-Pot Synthesis of $CoFe_2O_4$/Graphene Oxide Hybrids and Their Conversion into FeCo/Graphene Hybrids for Lightweight and Highly Efficient Microwave Absorber," *J. Mater. Chem. A*, **3** 5535-5546 (2015).

[8] K. Chang, and W. Chen, "L-Cysteine-Assisted Synthesis of Layered MoS_2/Graphene Composites with Excellent Electrochemical Performances for Lithium Ion Batteries," *ACS nano,* **5** [6] 4720-4728 (2011).

[9] S. Chen, Y. Xin, Y. Zhou, Y. Ma, H. Zhou, and L. Qi, "Self-Supported $Li_4Ti_5O_{12}$ Nanosheet Arrays for Lithium Ion Batteries with Excellent Rate Capability and Ultralong Cycle Life," *Energy Environ. Sci.*, **7** 1924-1930 (2014).

[10] C. Wang, X. Zhang, Y. Zhang, Y. Jia, J. Yang, P. Sun, and Y. Liu, "Hydrothermal Growth of Layered Titanate Nanosheet Arrays on Titanium Foil and Their Topotactic Transformation to Heterostructured TiO_2 Photocatalysts," *J. Phys. Chem. C,* **115** [45] 22276-22285 (2011).

[11] H. D. Yu, Z. Zhang, and M.Y. Han, "Metal Corrosion for Nanofabrication," *Small*, **8** [17] 2621-2635 (2012).

[12] N.M. D. Brown, N. Cui, and A. McKinley, "An XPS Study of the Surface Modification of Natural MoS_2 Following Treatment in an RF-oxygen Plasma," *Appl. Surf. Sci.*, **134** [1] 11-21 (1998).

[13] T. Wang, L. Liu, Z. Zhu, P. Papakonstantinou, J. Hu, H. Liu, and M. Li, "Enhanced Electrocatalytic Activity for Hydrogen Evolution Reaction from Self-assembled Monodispersed Molybdenum Sulfide Nanoparticles on an Au Electrode," *Energy Environ. Sci.*, **6** [2] 625-633 (2013).

[14] Y. Gong, S. Yang, Z. Liu, L. Ma, R. Vajtai, P. M. Ajayan, "Graphene-Network-Backboned Architectures for High-Performance Lithium Storage," *Adv. Mater.*, **25** [29] 3979-3984 (2013).

[15] M. Mao, L. Mei, D. Guo, L. Wu, D. Zhang, Q. Li, and T. Wang, "High Electrochemical Performance Based on the TiO_2 Nanobelt@few-layered MoS_2 Structure for Lithium-Ion Batteries," *Nanoscale*, **6** [21] 12350-12353 (2014).

[16] X. Sun, and Y. Li, "Colloidal Carbon Spheres and Their Core/Shell Structures with Noble-Metal Nanoparticles," *Angew. Chem. Int. Ed.*, **43** [5] 597-601 (2004).

[17] X.H. Cao, Y.M. Shi, W.H. Shi, X.H. Rui, Q.Y. Yan, J. Kong, and H. Zhang, "Preparation of MoS_2-Coated Three-Dimensional Graphene Networks for High-Performance Anode Material in Lithium-Ion Batteries," *Small*, **9** [20] 3433-3438 (2013).

[18] G.N. Zhu, Y.G. Wang, and Y.Y. Xia, "Ti-Based Compounds as Anode Materials for Li-ion Batteries," *Energy Environ. Sci.*, **5** [5] 6652-6667 (2012).

[19] X. Xu, Z. Fan, S. Ding, D. Yu, and Y Du, "Fabrication of MoS_2 Nanosheet@ TiO_2 Nanotube Hybrid Nanostructures for Lithium Storage," *Nanoscale*, **6** [10] 5245-5250 (2014).

[20] X. Zhu, C. Yang, F. Xiao, J. Wang, and X. Su, "Synthesis of Nano-TiO_2-Decorated MoS_2 Nanosheets for Lithium Ion Batteries," *New J. Chem.*, **39** [1] 683-688 (2015).

[21] J. Luo, X. Xia, Y. Luo, C. Guan, J. Liu, X. Qi, C. F. Ng. T. Yu, H. Zhang, and H. J. Fan, "Rationally Designed Hierarchical TiO_2@Fe_2O_3 Hollow Nanostructures for Improved Lithium Ion Storage," *Adv. Energy Mater.*, **3** [6] 737-743 (2013).

[22] J. Y. Shin, D. Samuelis, and J. Maier, "Sustained Lithium-Storage Performance of Hierarchical, Nanoporous Anatase TiO_2 at High Rates: Emphasis on Interfacial Storage Phenomen," *Adv. Funct. Mater.*, **21** [18] 3464-3472 (2011).

[23] M. V. Reddy, G. V. Subba Rao, and B.V.R. Chowdari, "Metal Oxides and Oxysalts as Anode Materials for Li Ion Batteries," *Chem. Rev.*, **113** [7] 5364-5457 (2013).

[24] S. Liu, H. Jia, L. Han, J. Wang, P. Gao, D. Xu, J. Yang, S. Che, "Hierarchical Zinc Oxide Materials with Multiple Porosity Prepared by Ultrafast Temperature Gradient Chemical Gas-Phase Synthesis," *Adv. Mater.*, **24** [4] 543-548 (2012).

[25] K. S. Park, A. Benayad, D. J. Kang, and S.G. Doo, "Nitridation-Driven Conductive $Li_4Ti_5O_{12}$ for Lithium Ion Batteries," *J. Am. Chem. Soc.*, **130** [45] 14930-14931 (2008)**.**

[26] L. Shen, C. Yuan, H. Luo, X. Zhang, S. Yang, and X. Lu, "In Situ Synthesis of High-Loading $Li_4Ti_5O_{12}$-Graphene Hybrid Nanostructures for High Rate Lithium Ion Batteries," *Nanoscale*, **3** [2] 572-574 (2011).

[27] J. Liu, K. Song, P. A. van Aken, J. Maier, and Y. Yu, "Self-Supported $Li_4Ti_5O_{12}$-C Nanotube Arrays as High-rate and Long-Life Anode Materials for Flexible Li-Ion Batteries," *Nano Lett.*, **14** [5] 2597-2603 (2014).

[28] Y. Q. Wang, L. Gu, Y. G. Guo, H. Li, X. Q. He, S. Tsukimoto, Y. Ikuhara, and L. J. Wan, "Rutile-TiO_2 Nanocoating for a High-rate $Li_4Ti_5O_{12}$ Anode of a Lithium-Ion Battery," *J. Am. Chem. Soc.*, **134** [18] 7874-7879 (2012).

[29] M. Gaberscek, J. Moskon, B. Erjavec, R. Dominko, and J. Jamnik, "The Importance of Interphase Contacts in Li Ion Electrodes: the Meaning of the High-Frequency Impedance arc," *Solid-State Lett.*, **11** [10] A170-A174 (2008).

[30] J. Guo, A. Sun, X. Chen, C. Wang. And A. Manivannan, "Cyclability Study of Silicon-Carbon Composite Anodes for Lithium-Ion Batteries Using Electrochemical Impedance Spectroscopy," *Electrochim. Acta*, **56** [11] 3981-3987 (2011).

[31] W. Stöber, A. Fink, and E. Bohn, "Controlled Growth of Monodisperse Silica Spheres in the Micron Size Range," *J. Colloid Interf. Sci.*, **26** [1] 62-69 (1968).

[32] W. Li, J. Yang, Z. Wu, J. Wang, B. Li, S. Feng, Y. Deng, F. Zhang, and D. Zhao, "A Versatile Kinetics-Controlled Coating Method to Construct Uniform Porous TiO_2 Shells for Multifunctional Core-Shell Structures," *J. Am. Chem. Soc.*, **134** [29] 11864-11867 (2012).

[33] W. Zhang, W. Zhou, J.H. Wright, Y.N. Kim, D. Liu, X. Xiao, "Mn-Doped TiO_2 Nanosheet-Based Spheres as Anode Materials for Lithium-Ion Batteries with High Performance at Elevated Temperatures," *ACS Appl. Mater. Interfaces*, **6** [10] 7292-7300 (2014).

[34] Y. Miki, D. Nakazato, H. Ikuta, T. Uchida, and M. Wakihara, "Amorphous MoS_2 as the Cathode of Lithium Secondary Batteries," *J. Power Sources*, **54** [2] 508-510 (1995).

[35] X. Fang, X. Yu, S. Liao, Y. Shi, Y.-S. Hu, Z. Wang, G.D. Stucky, and L. Chen, "Lithium Storage Performance in Ordered Mesoporous MoS_2 Electrode Material," *Microporous and Mesoporous Mater*., **151** 418-423 (2012)**.**

[36] T. Fröschl, U. Hörmann, P. Kubiak, G. Kučerová, M. Pfanzelt, C.K. Weiss, R. Behm, N. Hüsing, U. Kaiser, and K. Landfester, "High Surface Area Crystalline Titanium Dioxide: Potential and Limits in Electrochemical Energy Storage and Catalysis, " *Chem. Soc. Review,* **41** [15] 5313-5360 (2012).

[37] W. Zhuang, L. Li, J. Zhu, R. An, L. Lu, X. Lu, X. Wu, and H. Ying, "Facile Synthesis of Mesoporous MoS_2-TiO_2 Nanofibers for Ultrastable Lithium Ion Battery Anodes," *ChemElectroChem*, **2** [3] 374-381 (2015).

[38] Y.-M. Lin, R.K. Nagarale, K.C. Klavetter, A. Heller, and C.B. Mullins, "SnO_2 and TiO_2-Supported-SnO_2 Lithium Battery Anodes with Improved Electrochemical Performance," *J. Mater. Chem.*, **22 [**22**]** 11134-11139 (2012).

[39] Y. Luo, J. Luo, J. Jiang, W. Zhou, H. Yang, X. Qi, H. Zhang, H.J. Fan, Y. Denis, and C.M. Li, "Seed-Assisted Synthesis of Highly Ordered TiO_2@α-Fe_2O_3 Core/Shell Arrays on Carbon Textiles for Lithium-Ion Battery Applications," *Energy Environ. Sci.*, **5** [4] 6559-6566 (2012).

[40] Y. Qiao, X. Hu, Y. Liu, G. Liang, M.C. Croft, and Y. Huang, "Surface Modification of MoO_xS_y on Porous TiO_2 Nanospheres as an Anode Material with Highly Reversible and Ultra-Fast Lithium Storage Properties," *J. Mater. Chem. A*, **1** [47] 15128-15134 (2013).

[41] S. Huang, Z. Wen, X. Zhu, and Z. Gu, "Preparation and Electrochemical Performance of Ag Doped $Li_4Ti_5O_{12}$," *Electrochem Commun.*, **6** [11] 1093-1097 (2004).

CONCLUSIONS AND PERSPECTIVES

A. Concluding Summary

This dissertation was focused on the development of surface-modified nanomaterials as high-performance anode materials for lithium-ion batteries. A series of studies has been completed to improve lithium-ion battery performance, including: 1) synthesis and physical characterization of surface-modified nanomaterials, including manganese/nickel-doped TiO_2 nanomaterials, nitrogen-treated macro/mesoporous TiO_2, $Li_4Ti_5O_{12}$-TiO_2 nanocomposites, and MoS_2 hierarchical nanomaterials; 2) fabrication of traditional (mixed with active materials, carbon black, and binder) and free-standing electrodes (binder and carbon black free) through different techniques 3) electrochemical performance evaluation and extraction of the underlying mechanisms governing capacitance. The main conclusions can be summarized as follows:

1. Ion-doped TiO_2 was produced from a room temperature ion-exchange process.

The protonated ditatanate ($H_2Ti_2O_5 \cdot H_2O$) is a crucial precursor to the success of this experiment. Unlike the previous papers which reported good electrochemical performance of protonated ditatanate with various morphologies,[1-4] in this work, we demonstrated the effects of a further ion-exchange of $H_2Ti_2O_5 \cdot H_2O$ with Mn and Ni ions. Electrochemical measurement results showed that this novel ion-doped TiO_2 exhibited superior reversible capacity, improved cycling stability and rate capability when used as a lithium ion battery electrode. We have found that the improved

electrochemical performance could be ascribed to the roles of dopant ions in inhibiting crystal structure conversion under calcination and thus improving the electrode/electrolyte interface stability during cycling, which has been seldom reported in open literature.

2. Nitrogen-treated macro/mesoporous TiO_2 was prepared by a one-step dropwise process using titanium isopropoxide as a precursor. Besides Mn and Ni ion-doping to create surface defects, nitrogen atmosphere calcination did also introduce surface defects along with the benefit of avoiding side reactions. In addition, these native surface defects (Ti^{3+}) enhanced the initial electrical conductivity of TiO_2 and acted as protective barrier layers between the liquid electrolyte and the electrode surface to inhibit electrolyte oxidization during cycling and HF etching generated by trace amounts of moisture reacting with $LiPF_6$ based electrolyte.[5,6] Therefore, compared to the air-treated samples, nitrogen-treated TiO_2 exhibited 57% of improvement in the electrochemical performance at elevated temperatures (55 °C).

3. Nanoporous $Li_4Ti_5O_{12}$-TiO_2 composites with plenty of interphase boundaries were synthesized by a modified method by extending the fabrication of macro/mesoporous TiO_2 in our previous work. Various phase assemblage of the composites can be tuned by employing different calcination temperatures. In addition, extrinsic defects were created by ion-exchange process and calcination under the nitrogen atmosphere, respectively. Electrochemical evaluations indicated that as-prepared $Li_4Ti_5O_{12}$-TiO_2 nanocomposites possessed high charge-discharge capacities and good cycling performance when used as an anode material for lithium

ion batteries. Especially, it exhibited excellent cyclic stability when tested at an elevated temperature of 55 °C, a reversible capacity of ~190 mAh g^{-1} at 30 mA g^{-1} after 50 cycles could be observed.

4. Hierarchical MoS_2 nanosheet-based structures ($Li_4Ti_5O_{12}$-MoS_2, TiO_2-MoS_2) were fabricated *via* a hydrothermal approach. The morphology and crystallinity of these hybrid nanostructures could be controlled by different reaction time and temperature. For example, increasing reaction temperature led to more crystalline feature and undesired morphology (larger grain size, irregular shape, and particle agglomeration) for both of $Li_4Ti_5O_{12}$-MoS_2 (LM) and TiO_2-MoS_2 (TM). Due to the unique hierarchical structure, sufficient conductivity, high electrode/electrolyte contact surface area, and good structure stability, these hybrid nanostructures exhibited high reversible capacity, wide operating temperature range, and remarkable rate capability (the capacities were over two times larger than TiO_2 and $Li_4Ti_5O_{12}$ samples at a high current density of 500 mA g^{-1}, Table II). These results are much better than ion-doped TiO_2 (IT), nitrogen-treated TiO_2 (NT), and surface-modified $Li_4Ti_5O_{12}$-TiO_2 nanocomposites (LT) in our previous work (detailed data is shown in Table II).

Table II. Discharge Capacities of Selected Samples in this Thesis at 25 and 55 °C [mAh g^{-1}].

	IT-R	**IT-E**	**NT-R**	**NT-E**	**LT-R**	**LT-E**	**LM-R**	**LT-E**	**TM-R**	**TM-E**
150 mA g^{-1}	78	169	108	248	147	170	433*	N/A	410*	659*
500 mA g^{-1}	50	147	67	181	117	141	315	299	152	297

*Discharge capacities at the current density of 100 mA g^{-1}

In addition, the common electrodes need to be mixed with a binder and carbon black and then pressed onto substrates before being assembled into a battery. This process introduces extra undesirable interfaces and reduces the overall specific energy storage capacity because of the additives.[7] Herein, the as-prepared $Li_4Ti_5O_{12}$-MoS_2 hierarchical nanostructures directly grown on the bendable substrate of Ti foil, avoids these drawbacks and could potentially be applied in flexible wearable electronics.

B. Perspectives for Future Work

Although a series of studies on the physical, structural and electrochemical properties of different anode materials have been carried out in this dissertation, it should be noted that the characterization of the electrode performance has focused on the specific capacity, cycle life, rate capability, and temperature-dependent performance. Other important performance parameters of the electrode such as thermodynamic properties, in-situ reaction mechanisms, and electrode/electrolyte interface stability during cycling have not been considered. Meanwhile, the exact roles of dopants in the discharge/charge process and their effects on crystallization are still unknown. It is therefore suggested that efforts should be made to the parameters mentioned above in order to fundamental understand and improve the performance of the electrode materials for lithium-ion batteries.

References

[1] N. Sutradhar, S.K. Pahari, M. Jayachandran, A.M. Stephan, J.R. Nair, B. Subramanian, H.C. Bajaj, H.M. Mody, and A.B. Panda, “Organic Free Low

Temperature Direct Synthesis of Hierarchical Protonated Layered Titanates/Anatase TiO_2 Hollow Spheres and their Task-Specific Applications," *J. Mater. Chem. A,* **1** 9122-9131 (2013).

[2] Y.G. Tao, Y.Q. Xu, J. Pan, H. Gu, C.Y. Qin, and P. Zhou, "Glycine Assisted Synthesis of Flower-Like TiO_2 Hierarchical Spheres and Its Application in Photocatalysis," *Mater. Sci. Eng. B*, **177** 1664-1671 (2012).

[3] B. Liu, J.E. Boercker, and E.S. Aydil, "Oriented Single Crystalline Titanium Dioxide Nanowires," *Nanotechnology,* **19** 505604 (2008).

[4] S.W. Pradhan, Y. Mao, S.S. Wong, P. Chupas, and V. Petkov, "Atomic-Scale Structure of Nanosize Titania and Titanate: Particles, Wires and Tubes," *Chem. Mater.*, **19** 6180-6186 (2007).

[5] L. Yu, X. Qiu, J. Xi, W. Zhu, and L. Chen, "Enhanced High Potential and Elevated Temperature Cycling Stability of $LiMn_2O_4$ Cathode by TiO_2 Modification for Li-Ion Battery," *Electrochim. Acta*, **51** 6406 (2006).

[6] S.T. Myung, K. Izumi, S. Komaba, Y.K. Sun, H. Yashiro, and N. Kumagai, "Role of Alumina Coating on Li-Ni-Co-Mn-O Particles as Positive Electrode Material for Lithium-Ion Batteries," *Chem. Mater.*, **17** 3695 (2005).

[7] J. Jiang, Y. Li, J. Liu, and X. Huang, "Building One-Dimensional Oxide Nanostructure Arrays on Conductive Metal Substrates for Lithium-Ion Battery Anodes," *Nanoscale*, **3** 45 (2011).